Experimental investigation and numerical simulation of the particle motion in flighted rotating drums

Dissertation
zur Erlangung des akademischen Grades

Doktoringenieurin
(Dr.-Ing.)

von M.Sc. Lanyue Zhang
geb. am 06.08.1987 in ChongQing, China

genehmigt durch die Fakultät für Verfahrens- und Systemtechnik
der Otto-von-Guericke-Universität Magdeburg

Promotionskommission	Prof. Dr.-Ing. Eckehard Specht (Vorsitz)
	Prof. Dr.-Ing. habil. Evangelos Tsotsas (Gutachter)
	Dr.-Ing. Jochen Mellmann (Gutachter)
	Prof. Dr.-Ing. Fabian Herz (Gutachter)
eingereicht am:	20.08.2020
Promotionskolloquium am:	02.12.2020

Zhang, Lanyue:
Experimental investigation and numerical simulation of the particle motion in flighted rotating drums
Otto von Guericke University Magdeburg, 2020.

Abstract

The particle motion in flighted rotating drum (FRD) is still a challenge due to the uncertain parameters and complicated particle movement. The number of particles in the dilute phase and the distribution of particles in the cross-section of the drum continuously change as the drum rotates. This information is essential to improve the performance of the drum and the product quality, but are not clearly understood by experimental or numerical approaches so far.

In this thesis, the experimental techniques of magnetic particle tracking (MPT) and particle tracking velocimetry (PTV) are applied to track the movement of particles in FRD. Besides, the discrete element method (DEM) is used to simulate the dynamic characteristics of the granular system in the drum.

In an FRD, the MPT technology is utilized to measure the particle motion. The movement of plastic balls and soybeans in a laboratory flighted rotating drum is investigated with 5 % filling degree at various rotating speeds. On the basis of tracer trajectories, translational and rotational velocity distributions of particles are evaluated. Further, the falling time of particles in the dilute phase is investigated in dependence on the discharge angle. In addition, the movement dynamics of curtains are evaluated in the equatorial region of the drum. As the measurements revealed, the particle motion in FRD is strongly influenced by the drum rotating speed and slightly affected by particle size and shape within the scope of this work.

The PTV method, combining the segmentation and tracking processes, is applied to simultaneously track many particles in an FRD with a satisfactory recovery ratio. The particle motion in the cross-section of the drum is systematically analyzed based on changes in correlated particle trajectories. DEM simulations are performed in correspondence to the experimental measurements. The simulations are in agreement with PTV measurements in terms of the holdup ratio and cascading rate of a single flight, the falling time of dilute phase, the distribution of particles among the three phases, the average velocities and granular temperatures of the particle system in FRD.

The effect of flights on the transverse particle motion in FRD is investigated by installing different numbers of flights on the drum. The loading and unloading profiles of the single flight and active flights, and the particle ratio of dilute phase are investigated on the basis of PTV measurements and DEM simulations. Besides, previous literature models are used to calculate the particle ratios in the flight phase and the dilute phase, respectively. A detailed comparison is represented and shows DEM simulations to agree well with PTV measurements, whereas literature models show significant deviations.

Kurzzusammenfassung

Die Partikelbewegung in einer Drehtrommel mit Schaufeleinbauten (FRD) ist aufgrund der unsicheren Parameter und ihrer komplizierten Natur immer noch eine Herausforderung. Die Anzahl der Partikel in der Partikel-Gas-Phase und die Verteilung der Partikel über den Querschnitt der Trommel ändern sich kontinuierlich während der Trommeldrehung. Informationenen darüber sind entscheidend, um die Leistung der Trommel und die Produktqualität zu verbessern. Jedoch werden diese durch experimentelle oder numerische Ansätze bisher nicht ausreichend beschrieben.

In dieser Arbeit werden die experimentellen Methoden der magnetischen Partikelverfolgung (MPT) und der Particle Tracking Velocimetry (PTV) angewendet, um die Bewegung von Partikeln in einer Drehtrommel mit Rechteck-Hubschaufeln zu verfolgen. Außerdem wird die Diskrete Elemente Methode (DEM) verwendet, um das dynamische Verhalten eines Schüttgutes in der Trommel zu simulieren.

Die MPT-Technologie wird verwendet, um die Bewegung von Plastikkugeln und Sojabohnen in einer Labor-Drehtrommel mit Schaufeleinbauten zu analysieren. Die Partikelbewegung wird mit 5 % Füllgrad bei verschiedenen Drehzahlen untersucht. Auf der Basis von Tracer-Trajektorien werden Translations- und Rotationsgeschwindigkeitsverteilungen von Partikeln ausgewertet. Ferner wird die Fallzeit von Partikeln in der Partikel-Gas-Phase in Abhängigkeit vom Abwurfwinkel untersucht. Zusätzlich wird die Bewegungsdynamik von Partikelschleiern in der Äquatorialebene der Trommel ausgewertet. Wie die Messungen im Rahmen dieser Arbeit zeigten, wird die Partikelbewegung in FRD stark von der Rotationsgeschwindigkeit der Trommel und nur geringfügig von der Partikelgröße und -form beeinflusst.

Die PTV-Methode, welche die Segmentierungs- und Verfolgungsprozesse kombiniert, wird angewendet, um gleichzeitig viele Partikel in einer FRD mit einer zufriedenstellenden Reproduktionsrate verfolgen zu können. Die Partikelbewegung im Querschnitt der Trommel wird systematisch anhand von Änderungen der korrelierten Partikelbahnen analysiert. DEM-Simulationen werden entsprechend den experimentellen Messungen durchgeführt. Die Ergebnisse der Simulationen stimmen überein mit den Ergebnissen der PTV-Messungen

hinsichtlich des Füllungsgrades und der Kaskadenrate einer Einzelschaufel, der Fallzeit in der Partikel-Gas-Phase, der Verteilung der Partikel auf die drei Bewegungsphasen, der Durchschnittsgeschwindigkeiten und der granularen Temperatur des Partikelsystems in FRD.

Um den Einfluss der Hubschaufelanzahl auf die transversale Partikelbewegung zu untersuchen, werden Drehtrommeln mit unterschiedlichen Anzahlen von Schaufeln präpariert. Die Lade- und Entladeprofile von Einzelschaufeln und aktiven Schaufeln sowie der Partikelanteil in der Partikel-Gas-Phase werden anhand von PTV-Messungen und DEM-Simulationen untersucht. Außerdem werden frühere Literaturmodelle verwendet, um die Partikelanteile in den Schaufeln bzw. der Partikel-Gas-Phase zu berechnen. Ein detaillierter Vergleich wird angestellt und zeigt, dass die DEM-Simulationen mit den PTV-Messungen gut übereinstimmen, während Literaturmodelle signifikante Abweichungen zeigen.

Contents

Nomenclature

$\boldsymbol{a}$	particle acceleration	[m/s^2]
A	reference area	[m^2]
$\boldsymbol{B}$	magnetic flux density	[A/m]
C_D	drag force coefficient	[-]
d_p	particle diameter	[m]
$\boldsymbol{d}$	displacement vector	[pixel]
D	diameter of the flighted rotary drum	[m]
$\boldsymbol{D}$	magnetic shift density	[C/m^2]
e	restitution coefficient	[-]
E	Young's modulus	[Pa]
$E^{'}$	alignment value of particle orientation	[°]
$\boldsymbol{E}$	electric field intensity	[V/m)]
f_{ca}	flight cascading rate	[% or kg/s]
f_{di}	particle ratio of dilute phase	[%]
f_F	flight holdup ratio	[%]
$\boldsymbol{f}_c$	interaction force between two particles	[N]
$\boldsymbol{f}_{con}$	particle conservation force	[N]
$\boldsymbol{f}_{dis}$	particle dissipative force	[N]
$\boldsymbol{f}_{pf}$	particle-fluid interaction force	[N]
F_D	drag force	[N]
Fr	Froude number	[-]
$\boldsymbol{g}$	gravitational acceleration	[m/s^2]
G	shear modulus	[Pa]
h	reference height	[m]
$\boldsymbol{H}$	magnetic field intensity	[A/m]
I	intensity of the matrix of raw image	[-]
$\boldsymbol{I}$	moment of inertia	[kg $\cdot$ m^2]

$\boldsymbol{J}$	current density	[A/m^2]
l	surface length of materials in flight	[m]
l_1, l_2	flight segments length	[m]
L	drum length	[m]
m	matrix size	[pixel]
m_p	particle mass	[kg]
n_F	flights number	[-]
$n_{F,a}$	number of active flights	[-]
N	reference number	[-]
P_n	number of neighbor particles	[-]
$\boldsymbol{P}$	match probability	[-]
$\widetilde{\boldsymbol{P}}$	non-normalized match probability	[-]
Q	quality function	[-]
$\boldsymbol{Q}$	match probability of neighboring particles	[-]
$\boldsymbol{r}$	position vector of dipole	[-]
r_{dHS}	length in Fig. 2.1	[m]
$r_{_H}$	distance from center to l_1	[m]
$r_{_{HS}}$	distance from center to the tip or the flight	[m]
R	drum radius	[m]
Re	Reynolds number	[-]
R_m	maximum displacement radius	[pixel]
R_n	neighboring radius	[pixel]
R_q	quasi-rigidity radius	[pixel]
R_r	recovery ratio	[-]
s	intensity in the matrix of particle image	[-]
S_f	scale factor	[pixel/mm]
S_{rot}	rotation path	[m]
$t, \Delta t$	time, time step	[s]
t_F	particle falling time	[s]
$\boldsymbol{T}$	torque	[N $\cdot$ m]
$u, \boldsymbol{u}$	particle velocity	[m/s]
U_{max}	particle maximum velocity	[m/s]
V	magnitude of particle velocity	[m/s]
x, y, z	Cartesian coordinates	[m]
X, Y, Z	normalized Cartesian coordinates	[-]

Greek symbols

α	flight angle, see Fig. 2.2	[°]
α_D	inclination of the drum	[°]

$\alpha(e)$	damping ratio	[-]
β_1, β_2	flight angle, see Fig. 2.2	[°]
γ	kinetic angle of repose	[°]
γ_{coef}	normalized cross-correlation coefficient	[-]
δ	flight discharge angle	[°]
δ_c	angle in Fig. 2.1	[°]
δ_{ij}	overlap between two particles	[m]
δ_L	last discharge angle	[°]
ϵ	angle in Fig. 2.1	[°]
η_n, η_t	normal and tangential damping coefficient	[-]
θ	granular temperature	[m^2/s^2]
θ_0	spherical coordinates of dipole	[°]
Θ_D	dynamic angle of repose	[°]
κ_n, κ_t	normal and tangential stiffness coefficient	[-]
κ_r	rolling coefficient	[N/m]
μ	friction coefficient	[-]
$\boldsymbol{\mu}_m$	magnetic moment of dipole	$[A \cdot m^2]$
μ_g	dynamic viscosity of gas	[Pa · s]
ρ	density	[kg/m^3]
σ	Poisson ratio	[-]
τ_H	collision time	[s]
ϕ	angle of rotation	[°]
φ_0	spherical coordinates of dipole	[°]
$\omega, \boldsymbol{\omega}$	particle angular velocity	[rad/s]
ω_D	drum rotational speed	[rpm]

Subscripts and superscripts

0	original point
$1, 2$	indices
$2D, 3D$	two or three dimensional
B, D, F	bed, dilute, flight phase
f	flight
Hz	Hertzian model
i, j, k	indices
n	normal direction
p	particle
r	rolling or relatively value
t	tangential direction, or tracer
w	wall

x, y, z	Cartesian coordinate components
λ	particle type
*	equivalent value

Abbreviations

AMR	anisotropic magneto resistive
ANOVA	analysis of variance
CFD	computational fluid dynamics
CV	coefficient of variation
DEM	discrete element method
FRD	flighted rotating drum
FUF	first unloading flight
MPT	magnetic particle tracking
PDF	probability distribution function
PEPT	positron emission particle tracking
PTV	particle tracking velocimetry

Chapter 1

Introduction

1.1 Flighted rotary drum

Rotary drums with internal flights are very commonly used in the mineral, food, sugar, fertilizer, and metallurgical industries for drying granular or particulate solids. Compared with other dryers, the flighted rotating drum (FRD) shows several advantages: simplicity, low cost, wide applicability and high processing capacity. In general, FRDs are operated as direct heat dryers, in which the wet materials are in direct contact with the hot air that flows in co-current or counter-current configuration. As the drum rotates, the flights lift the materials up to a certain height then throw them into the cross-section of the drum. These particles generate a series of curtains which are highly exposed to the hot gas providing sufficient heat and mass transfer. When the fall of the solids ends, they may bounce or slip due to particle-particle, particle-flight, or particle-wall collisions. At the same time, solids are transported to the axial direction due to the inclination of the drum and the action of the flights.

The loading of a rotary drum is the total amount of material in the drum. It is affected by the drum operating conditions, material flow properties, gas flow rate and the dryer geometry. Three loading states of FRD are categorized: under-loaded, design-loaded, and over-loaded [1, 2]. These states are distinguished by defining a first unloading flight (FUF) in the FRD, which is the flight that first discharges solids during rotation. In a design-loaded dryer, the FUF is exactly located at the 9 o'clock position for a clockwise rotating drum and its tip is located on the horizontal line passing through the center of the cross-section of the drum. A drum is classified as under-loaded when the flights are not full to their capacity and discharging occurs after the 9 o'clock position. An over-loaded drum is defined when there are more solids than required to fill the flights. In this situation, there is discharge before the 9 o'clock position and the excess material rolls to the bed

phase at the bottom of the drum. It should be noted that when a drum is operated at design load, the maximum ratio of solids is lifted up to the upper half of the drum and then showers into the gas phase. Therefore, maximum heat and mass transfer can be expected between the material and the gas. This illustrates that the drum loading state strongly affects the drum performance.

In 1987, Matchett and Baker [1] reported a model that treated the flow of material in FRD as consisting of two phases. One phase, called airborne phase, consists of the falling particles which are affected by gravity and drag forces due to the air flow through the dryer. The other phase, called dense phase, consists of the particles which rest in the flights or in the overload bed at the bottom of drum. Later, the dense phase was further divided into two parts: the bed dense phase at the bottom of the drum and the flight dense phase in the active flights (the flights filled with material and located in the upper half of the drum) [3]. As the drum rotates, particles interchange freely among the three phases. Clearly, more dilute phase is expected in the FRD than in an empty drum with many potential benefits, such as energy saving and efficiency improvement.

The material in FRD is elevated and cascaded into the gas with the help of flights. Thus, the amount of dilute phase is mainly controlled by the number, dimension and shape of the flights. Good flight design is essential to promote the gas-solid contact which is required for rapid and homogeneous drying. The most commonly used flight profiles are shown in Fig. 1.1.

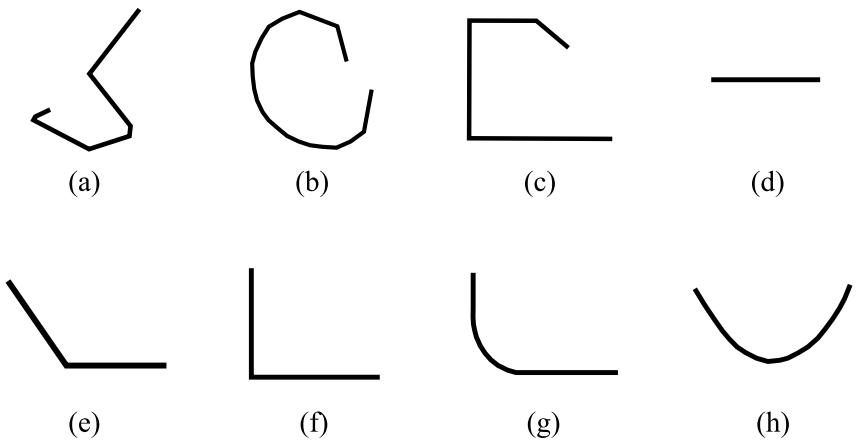

Figure 1.1: Common flight profiles.

As it could unload particles centrally, the flight shown in Fig. 1.1 (a) was chosen in some experiments to make more particles cascade at or around the vertical diameter of the drum [4]. For this flight profile, the heat transfer is expected to be most pronounced as a larger proportion of particles have the longest falling distance. Alternatively, it is possible to arrange for a cascade pattern that maximizes the amount or the proportion of particles in the drum, which are cascading at a certain point in time. However, this flight

profile creates a non-uniform particle concentration in the cascading curtains, which in turn causes uneven patterns in the gas flow. The heat transfer is rather reduced as the gas flow will take the easiest route through the drum, where the particle concentration is lowest.

Based on these studies, Kelly [5] proposed that the equal horizontal distribution (EHD) flight profile may be close to the optimum design, as shown in Fig. 1.1 (b) and (c). This flight profile could give a uniform concentration of dilute phase, thereby providing the most effective heat and mass transfer between solids and gas. Unfortunately, the shape of EHD flight is somewhat impractical when dealing with sticky solids which are commonly processed in flighted rotary dryers. Besides, this work points out that different flight profiles are suitable for different drum rotating speeds, but not for different values of the solids kinetic coefficient of friction.

The other flights (d)-(h) of Figure 1.1 are more frequently used in FRD [6]. In general, the radial fights (d) and (e) are suitable for sticky materials, while circular flight (h) has been applied by Purcell [7] to develop a uniform distribution of curtains and is supposed to be easier to form in comparison with types (f) and (g). The rectangular flights (f) are mostly used for free flowing bulk materials.

In addition, the number of flights is a key parameter of drum design, since it defines the number of curtains responsible for the heat and mass transfer. Obviously, a small number of curtains reduces the contact area between material and gas phase, resulting in poor dryer performance. However, too many curtains also have a negative effect, since the size of the gaps between the curtains decreases and does not allow the gas to pass through [8]. Thus, the selection of the number of flights should be carefully considered.

1.2 Motivation and objectives

When the drum rotates, particles switch continuously among the bed phase, the flight phase and the dilute phase. In the region of the dilute phase, heat and mass are vividly transferred between the particles and gas during drying or cooling processes. Thus, the particle distribution in the cross-section of the drum is closely related to drum performance [9]. However, the movement of particles in FRD is rather complicated since it is influenced by many parameters: drum geometry (dimensions, flight configuration and number), drum operating parameters (rotating speed, filling degree, gas and material flow rates), and the material properties (particle diameter, shape, density and dynamic angle of repose) [8, 10].

Different research methods have been applied to study the particle motion in FRD, including experimental measurements, mathematical calculations, and numerical simulations. Collectively, these studies mainly focus on the loading profiles of the flights or the mixing behavior of bi-dispersed and poly-disperse particle systems. The particle motion in the

dilute phase and the bed phase in FRD is still unclear. Specifically, experimental analysis is usually limited to manually measuring the area of particles on photographs, which is very time consuming. Numerous mathematical formulas have been derived to describe the profile of granular matter in moving flights. In addition, numerical simulations are conducted to provide more details of the particle motion in FRD. However, the development and verification of mathematical equations and numerical models require the support by experimental data. More robust and intelligent experimental techniques should therefore be implemented to further study particle motion in FRD.

In regard of particle dynamics in a granular bed, four measurement techniques are commonly utilized to reconstruct individual particle trajectories in different configurations: radioactive particle tracking, positron emission particle tracking (PEPT), magnetic particle tracking (MPT), and image analysis method. The radioactive particle tracking method, which is based on the attenuation of γ-rays in material, has been used in rotary drums to characterize particle mixing, segregation, and velocity profiles [11–13]. The method of PEPT, based on positron annihilation, was developed by Hawkesworth et al. [14]. Parker et al. [15] firstly used it in a rotary drum to study the thickness of active layer, rolling motion of spheres and particle axial dispersion. Then, this method was applied to analyze particle velocities in the passive and active regions of a granular bed [16, 17]. However, the handling of radioactive substances is problematic in practice.

The MPT technique includes a magnetic tracer, a magnetic monitoring system and the algorithm to reconstruct the particle position and orientation based on the analysis of quasi-static magnetic field around the tracer particle [18]. It can measure particle translational and rotational speeds simultaneously, which is impossible for other tracking technologies. So far, the MPT technique has not been applied to the research of rotary drums.

Image analysis methods have often been used in experimental studies of particle behavior in FRD. Some parameters, such as the kinetic angle of repose, particle falling height, and material area in a flight have been extracted manually or semi-automatically from the experimental images [19–21]. Particle tracking velocimetry (PTV), an image-based measurement technique, can be utilized to simultaneously track a large number of particles in 2D or 3D setups [22, 23]. Compared with traditional particle image velocimetry, which is based on spatial cross-correlation, PTV can quantify flow velocities on single particle level [24]. As yet, there is no application of image particle tracking method in FRD.

The aim of the present work is to investigate the particle motion and particle ratio distribution in FRD with rectangular flights, in terms of the holdup and discharge ratio of single flight and active flights, particle ratio in each of the three mentioned phases, the falling time in the dilute phase, and the velocity characteristics of particles. The MPT and PTV methods will both be applied to track particles in FRD. The measurement results will be compared with DEM simulation data. Understanding the particle motion in FRD

is of major importance to improve the performance of the drum and the quality of final product.

1.3 Outline of the thesis

This dissertation is divided into 10 chapters. In Chapter 2, the literature about the transversal motion of particles in FRD is reviewed via three parts: previous geometrical models, experimental measurements, and numerical simulations. In Chapter 3, the theoretical principle of the magnetic tracking technology is introduced. Then, the moving behavior of a high-density tracer is investigated to verify the applicability of the MPT method in the FRD. In Chapter 4, the algorithms used in the particle segmentation procedure and the particle tracking procedure are described. Then, the calibration of the parameters used in the PTV is conducted based on drum images. In Chapter 5, the experimental setup of the laboratory-scale FRD and the operating parameters of the experiments are introduced in detail. In Chapter 6, the governing equations as well as the contact and rolling models applied in the DEM simulations are described. Besides, the DEM parameters are presented with calibration process.

In Chapter 7, the MPT method is applied for continuous 3D tracking of particles in the horizontally arranged laboratory-scale FRD. The time-averaged translational and rotational velocity distributions are evaluated in dependence on the type of bed material and drum rotating speed. Furthermore, the falling time of particles in the dilute phase is determined as a function of discharge angle. In addition, translational velocities are measured in the dilute phase in the equatorial region of the drum.

In Chapter 8, PTV measurements and DEM simulations are conducted to investigate particle dynamics. A comparison between the PTV experimental results and DEM simulations is presented in terms of the holdup and cascading rate of a single flight, the falling time distribution in the dilute phase, particle ratios in each of the three considered phases, and the average velocity and granular temperature of the particle system. The effects of drum rotating speed and drum filling degree on the particle motion are studied in detail.

In Chapter 9, the effect of the number of flights on particle moving behavior in the transverse section of drums is estimated by the PTV method and DEM simulations. The holdup ratio and discharge rate of a single flight and active flights, as well as the particle ratio of the dilute phase are analyzed in detail. Besides, the results of the PTV measurements are compared with the predictions of previous literature models.

In Chapter 10, the main results of the thesis are summarized and an outlook to future studies is given.

Chapter 2

Literature view on particle motion in the FRD

FRDs are used in a broad range of industrial applications. The movement of particles is mostly dependent on flights and drum geometry as well as on the operating conditions. Due to the close correlation between solids transport behavior and the drum performance, several research investigations have been carried out in the past decades. All these studies can be divided into three groups: geometrical models, experimental measurements, and numerical simulations.

2.1 Geometrical models for particle motion

The motion of particles in FRD is quite complex, as the particles are lifted and cascaded by the flights, then re-entering the bed at the bottom, with the possibility of bouncing and rolling. In many contributions, geometrical models have been reported to describe the solids transport in the cross-section of the FRD. It is worth noting that there is no unified model capable of predicting the movement of particles with different shape, size and flow characteristics in a flight. Also, no geometrical model has been developed to describe the particle motion in flights with arbitrary geometry. But, geometrical models can quickly solve practical problems and provide useful information for scaling up, so they are widely used in industry.

2.1.1 Kinetic angle of repose

The kinetic angle of repose is composed by the material surface in a flight to the horizontal plane. This angle changes with the rotation of the drum until all particles have left the flight. When the angle of material surface is larger than the maximum stability angle at a certain angle position, an avalanche occurs on the material surface to achieve a new stable surface in the flight.

In 1962, Schofield and Glikin [25] calculated the kinetic angle of repose by balancing the gravitational, centrifugal, and frictional forces at the tip of the flight. It assumed that only one layer of particles are flowing over the flight surface. The kinetic angle of repose is determined in terms of the flight geometry, angle position of the flight, drum speed, and material properties. The relevant parameters are illustrated in Fig. 2.1 (a) and the model is expressed as

$$\tan\gamma = \frac{\mu + Fr\left(\frac{r_{HS}}{R}\right)(\cos\delta - \mu\sin\delta)}{1 - Fr\left(\frac{r_{HS}}{R}\right)(\sin\delta + \mu\cos\delta)}. \tag{2.1}$$

Where, μ is the coefficient of dynamic friction which is calculated from the dynamic angle Θ_D ($\mu = \tan\Theta_D$); r_{HS} is the radius formed by the tip of the flight and δ is the discharge angle, as shown in Fig. 2.1. Fr is the Froude number which is calculated from the drum rotating speed and drum radius ($Fr = \omega_D^2 R/g$). There is no variable related to the flight profile in Eq. 2.1, which means this model assumes that the surface angle of the material in a flight is independent of flight geometry.

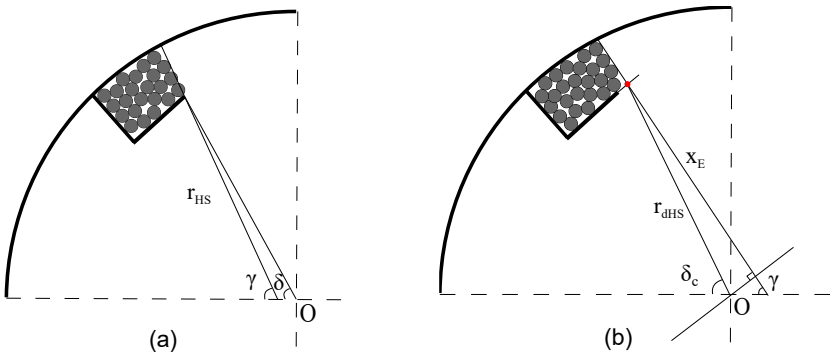

Figure 2.1: Schematic diagram of the relevant parameters used in the kinetic angle of repose models: (a) the model of Schofield and Glikin (1962); (b) the model of Sunkara et al.(2015).

Based on the above work, Sunkara et al. [26] proposed an extended model by assuming an active layer at the flight surface and including the inertial force in the force balance analysis. The velocity profile of this particle layer was predicted by treating the granular material as a continuum. New parameters are defined, as depicted in Fig. 2.1 (b). The kinetic angle of repose can be calculated by

$$\tan\gamma = \frac{\mu + Fr\left(\frac{r_{dHS}}{R}\right)(\cos\delta_c - \mu\sin\delta_c) + Fr\dfrac{\overline{u}_x^*}{\cos\gamma}\dfrac{d\overline{u}_x^*}{dx^*}}{1 - Fr\left(\frac{r_{dHS}}{R}\right)(\sin\delta_c + \mu\cos\delta_c)}. \tag{2.2}$$

Where, $\overline{u}_x^* = \overline{u}_x/R\omega_D$ and $\overline{u}_x$ is the average velocity of the particles in the active layer. It is $\delta_c = \gamma - \arcsin(x_E/r_{dHS}) \pm 90°$, where the negative sign is for $\delta_c < \gamma$ and the positive

sign for $\delta_c > \gamma$. Good performance of the extended model was observed in comparison between model predictions and experimental measurements. It should be noted that the velocity gradient of the particles in the active layer needs to be validated before using this model. However, it is quite difficult to determine the velocity profile and layer thickness either by empirical formula calculation or by experimental measurement.

2.1.2 Holdup of a flight

The holdup of a flight is important to know, as it determines how many particles will subsequently enter the dilute phase region. In the cross-section of the FRD, the relative holdup of a flight is expressed as the area occupied by material in the flight to the total area occupied by material in the transverse of the drum. Through geometric analysis, the particle area in a flight can be expressed as a function of drum size, flight profile, flight discharge angle, dynamic and kinetic angles of repose. In this way, many geometric models have been proposed in the last decades to predict the holdup of specific shaped flights under various operating conditions. Typical length and angle parameters used in these empirical models are illustrated in the cross-section of the drum, as shown in Fig. 2.2.

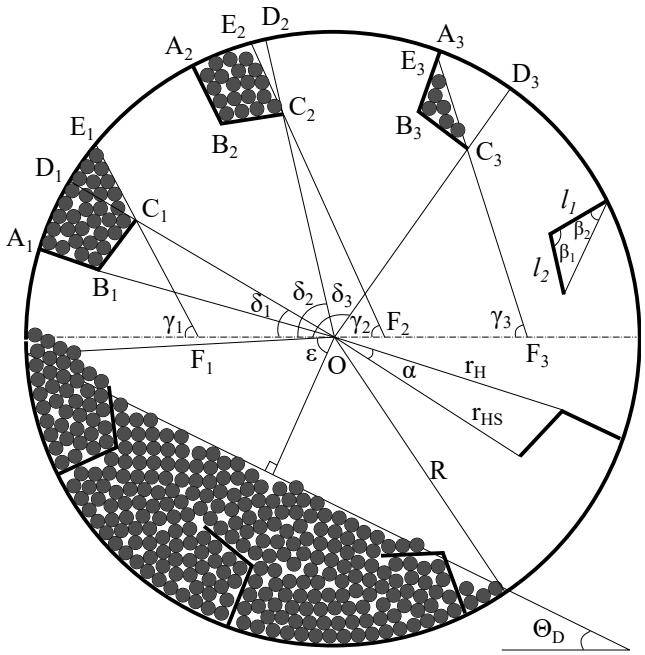

Figure 2.2: Schematic diagram of a flighted rotary drum with design parameters.

In 1978, Glikin [27] developed a model to determine the solids area (A) in an rectangular flight at the discharge angle δ. The kinetic angle of repose of solids γ in this model is determined by Eq. 2.1. In the whole discharging process, the calculation of the flight's holdup is divided into four stages, as expressed in Table 2.1, Eqs. 2.3. It should be noted that in these equations, the solids area supported by the flight and the rotating wall is

simplified to a polygon. It means that a small arch area is ignored. Besides, this model holds only for a drum with rectangular flights.

In 1988, Baker [28] proposed two geometric models to calculate the solids area in general angled flights and in extended circular flights, respectively. In an angled flight, lines C_1D_1, C_2D_2 and C_3D_3 in Fig. 2.2 are equal to $(R - r_{HS})$. Thus, the solids area in the flight can be easily obtained by subtracting the area of the excess triangles and wedges from the fan area. A general formula is derived to accurately calculate the area of the 'wedge' ($A_{\triangle CDE}$ or $A_{\triangle C_2D_2E_2}$). The expressions of the particle area in a flight are given by Eqs. 2.4 in Table 2.1. The solids area in the extended circular flight can be derived and calculated by a similar formula, but this is not shown here.

In 1993, Sherritt et al. [3] calculated the area of solids in a flight by integrating the flight discharge rate from the initial discharge angle δ_{init} to the final discharge angle δ_L. Assuming that a wedge of particles discharges from the flight tip as the drum rotates, the infinitesimal discharge area of a flight and the area of solids in a flight at δ can be calculated by Eqs. 2.5 in Table. 2.1. Variable l is the length of the exposed surface of the solids in a flight (line C_1E_1, C_2E_2 or C_3E_3 in Fig. 2.2). However, in this equation, the area of the wedge is calculated from the auxiliary circle centered on the flight tip rather than the circle representing the drum wall. This excessive simplification of the geometric analysis results in the particle area being smaller than the actual value. To solve this problem, Wang et al. [29] accurately calculated the cross-section area filled with material in a flight. The model was developed by assuming that the material surface can be determined from the dynamic angle of repose of the material, neglecting the presence of any material flowing over the flight tip. The entire unloading process of the flight was divided in these stages and the area of solids at various stages was calculated with the software Calculus Calculator.

Considering that most of the existing models were based on an angular flight with two segments, Revol et al. [30] developed a new set of equations to predict the solids holdup in flights with three segments. Unlike the previous models which have only one coordinate system with the drum axis as the origin, this study defined an additional moving coordinate system with the flight tip as the origin. The coordinates of the intersection between the material surface and drum wall, as well as the intersections of the segments, were utilized to the calculation of the material area in a flight. However, the kinetic angle of repose of solids was determined by the model of Schofield and Glikin [25], which means the value of this angle is appropriate for flights with any number of segments. It is foreseeable that this situation will bring errors to the prediction of the model. Similar geometrical model derivation was also reported by Lisboa et al. [31] to predict the solids area in two-segment flights. Besides, van Puyfelde [32] presented a model called GFRLift to illustrate the holdup profile of different flights in a rotary dryer. The performance of simple and complex flights was investigated by evaluating the loading profiles.

In 2013, Sunkara et al. [8] estimated the influence of flight length ratio on the holdup and discharge characteristics of the rectangular flight. Mathematical models for the filling degree of a rectangular flight were derived without any geometrical simplifications. The solids areas of flight at discharge angle δ are given by Eqs. 2.7 in Table 2.1. The kinetic angle of repose γ in this model was calculated from the classical Schofield and Glikin model (Eq. 2.1) [25] instead of their new model (Eq. 2.2). The rectangular flight with a flight length ratio of $l_2/l_1 = 1$ showed the most suitable discharge characteristics, which produced the most uniform particle distribution over the cross-section of the drum.

All the above models for predicting flight holdup assume that the material surface is free flowing and is defined by the kinetic angle of repose of material. However, research has confirmed that the surface angle of a granular solid can be increased beyond the angle of repose of material whilst remaining stable [33, 34]. An angle of maximal stability seems to exist for granular materials, several degrees larger than the angle of repose, beyond the degree which the material surface becomes unstable and avalanches appear. This phenomenon suggests that the previous models very likely under-predict the holdup of the flight and are not accurate enough to estimate flight holdup.

Considering this phenomenon, Lee and Sheehan [35] derived geometric models to predict the flight loading behavior for a two-segment angled flight by using a mean surface angle. The expressions for the material-filled area of the flight in two discharge regions are given by Eqs. 2.6 in Table 2.1, respectively. The mean surface angle used in the equations should be measured from a series of experiments; it lies between the kinetic angel of repose of the material and the maximum angle of stability. In addition, this work indicates that the accuracy of a model is highly dependent on the accuracy of mean surface angle. A similar study was reported by Debacq et al. [36]. The value of the maximum angle of stability was experimentally measured for various flight positions at ambient and high temperatures. This angle was then utilized in the corresponding model to calculate the volume fraction of fine cohesive powders contained in a flight.

Table 2.1: Different geometric formulas for calculating the particle area in a flight.

Glikin (1978) [27]	For $0 < \delta \leq \gamma$ $A(\delta) = l_2 l_1 \cdot \frac{R - l_1/2}{R - l_1} + \frac{1}{2} l_1^2 \cdot \tan(\gamma - \delta)$; for $\gamma < \delta \leq \gamma + \alpha$ $A(\delta) = l_2 l_1 \cdot \frac{R - l_1/2}{R - l_1} - \frac{1}{2} l_1^2 \cdot \tan(\delta - \gamma)$; for $\gamma + \alpha < \delta \leq \gamma + \alpha + \arctan(l_2/l_1)$ $A(\delta) = l_2 l_1 \cdot \frac{R - l_1/2}{R - l_1} - \frac{1}{2} l_1^2 \cdot [\tan(\alpha) + \tan(\delta - \gamma - \alpha)]$; for $\gamma + \alpha + \arctan(l_2/l_1) < \delta \leq \gamma + \alpha$ $A(\delta) = l_2^2/(2 \cdot \tan(\delta - \gamma - \alpha))$.	(2.3)
Baker (1988) [28]	For $0 < \delta \leq \gamma$ $A(\delta) = \frac{\alpha R^2}{2} - l_2^2 \cdot \sin(\beta_1 - \alpha) \cdot \sin\beta_1 \cdot \sin\alpha/2 + A_{\triangle DCE}$; for $\gamma < \delta \leq (\gamma + \alpha + \beta_2)$ $A(\delta) = \frac{\alpha R^2}{2} - l_2^2 \cdot \sin(\beta_1 - \alpha) \cdot \sin\beta_1 \cdot \sin\alpha/2 - A_{\triangle DCE}$; for $(\gamma + \alpha + \beta_2) < \delta \leq \delta_L$ $A(\delta) = l_2^2 \cdot \sin\beta_1 \cdot \sin(\delta - \gamma + \beta_1 - \alpha)/2 \cdot \sin(\delta - \gamma - \alpha)$. Here, $A_{\triangle DCE} = \frac{1}{2} R^2 [(\gamma - \delta) - \arcsin(\frac{r_{HS}}{R} sin(\gamma - \delta))]$ $-\frac{1}{2} R \cdot r_{HS} \cdot \sin\left[(\gamma - \delta) - arcsin\left(\frac{r_{HS}}{R}\sin(\gamma - \delta)\right)\right]$.	(2.4)
Sherritt et al. (1993) [3]	$dA = \pi l^2 d\delta$; $A(\delta) = \pi \int_{\delta_{init}}^{\delta_L} l^2 d\delta$.	(2.5)
Lee and Sheehan (2010) [35]	For $0 < \delta \leq \delta_t$ $A(\delta) = R^2 \left(\gamma - \delta + \alpha - \arcsin\left[(\frac{r_{HS}}{R})\sin(\delta + 180° - \gamma)\right]\right) \cdot \frac{\pi}{180°}$ $-R \cdot r_{HS} \cdot \sin\left(\gamma - \delta - \arcsin\left[(\frac{r_{HS}}{R})\sin(\delta + 180° - \gamma)\right]\right)$ $-r_H(l_2 \cdot \sin\beta_1)$; for $\delta_t < \delta \leq 180° + \gamma - \beta_1$ $A(\delta) = l_2^2 \cdot \sin\beta_1 \cdot \sin(180° - \beta - \delta_1 + \alpha + \gamma)/\sin(\delta - \alpha - \gamma)$. Here, $\delta_t = 90° + \gamma + \arcsin\left(l_2 \cdot \sin\beta_1 / \sqrt{l_1^2 + l_2^2 - 2 l_1 l_2 \cos\beta_1}\right)$.	(2.6)
Sunkara et al. (2013) [8]	For $0 < \delta \leq \gamma$ $A(\delta) = \frac{\pi R^2(\gamma + \epsilon^* - \varphi)}{180°} - r_H \cdot R \frac{\cos(\kappa - \gamma)}{\cos(\alpha)} \frac{\sin(\gamma + \epsilon^* - \varphi)}{\cos(\varphi - \gamma)} - l_2^2 \cdot \tan(\varphi - \gamma)$; for $\gamma < \delta \leq \gamma + \alpha + \beta_2$ $A(\delta) = \frac{\pi R^2(\gamma + \epsilon^* - \varphi)}{180°} - R^2 \sin(\epsilon^*)\cos(\epsilon^*) - \frac{(R \cdot \cos(\epsilon^*))^2}{\tan(\delta - \gamma)} - r_H \cdot l_2$; for $\gamma + \alpha + \beta_2 < \delta \leq \delta_L$ $A(\delta) = l_2^2 \cdot \frac{1}{\tan(\delta - \gamma - \alpha)}$. Here, $\epsilon^* = \arccos\left[(\frac{r_H}{R})\frac{\cos(\kappa - \gamma)}{\cos(\alpha)}\right]$, $\varphi = \kappa - \alpha$, and $\kappa = 90° - \delta$.	(2.7)

2.1.3 Falling height of the dilute phase

In order to estimate the exposure time of the dilute phase in hot air, it is necessary to estimate the falling height of particles in FRD. Generally, the falling height is simplified as the vertical distance from the flight tip to the bottom rotating wall. According to Glikin [27], the falling height h_F can be calculated by

$$h_F = \frac{r_{HS} \cdot \sin\delta + \sqrt{R^2 - (r_{HS} \cdot \cos\delta)^2}}{\cos\alpha_D}. \tag{2.8}$$

Here, the α_D is the inclination angle of the drum.

In 2013, Debacq et al. [37] analyzed the falling height of particles in a drum which was placed horizontally and filled partially. By assuming the falling particles to hit the surface of granular bed instead of the rotating wall, the falling length was determined as

$$\begin{aligned} h_F = {} & r_H \cdot \sin(\delta - \alpha) + l_2 \cdot \cos(\delta - \alpha) + R \cdot \cos(\epsilon + \Theta_D) \\ & - \tan\Theta_D \cdot [(r_H - l_2 \cdot \tan(\delta - \alpha)) \cdot \cos(\delta - \alpha) - R \cdot \sin(\epsilon + \Theta_D)] \, . \end{aligned} \tag{2.9}$$

Following this work, Sunkara et al. [38] further divided the particle falling procedure into two situations. The first case is when the falling particles hit the bed surface at the bottom of the drum. After the flight tip rotates to the position vertically above the lower end of the bed δ_{BE}, the falling particles would hit either the rotating wall or the flight sheets. The expressions for particle falling height were given by:

For $0 \leq \delta < \delta_{BE}$,

$$h_F = R\frac{\cos\epsilon}{\cos\Theta_D} + r_H \cdot \frac{\sin\delta - \tan\Theta_D \cdot \cos\delta}{\cos\alpha}. \tag{2.10}$$

For $\delta_{BE} \leq \delta < \delta_L$:

a) The falling particles hit the rotating wall,

$$h_F = r_H \cdot \frac{\sin\delta}{\cos\alpha} + \sqrt{R^2 - r_H^2 \cdot \left(\frac{\cos\delta}{\cos\alpha}\right)^2}. \tag{2.11}$$

Here, $\delta_{BE} = 180° - \arccos(R \cdot (\cos\alpha \cdot \sin(\epsilon - \Theta_D))/r_H)$.

b) The falling particles hit the flight sheet,

$$h_F = 2 \cdot r_H \cdot \frac{\sin\delta}{\cos\alpha}. \tag{2.12}$$

Here, the $\delta_{BE} = 90° + \arccos\left(R \cdot (\cos\alpha \cdot \sin\epsilon)/r_H\right) - \Theta_D$.

2.1.4 Particle ratio of dilute phase

In 1993, Sherritt et al. [3] predicted the total airborne holdup by using the average discharge rate of one flight and the total number of flights (n_F). The particle ratio of the dilute phase was expressed as

$$f_{di} = n_F \cdot \frac{\omega_D}{2A_s} \int_{\delta_{init}}^{2\pi} l^2 \cdot t_F \, d\delta. \tag{2.13}$$

Here, t_F is the falling time of a particle which can be calculated by $\sqrt{2h_F/g}$. Particle falling height h_F is determined by Eq. 2.8. A_s is the material area in the cross-section of the drum.

Wang et al. [29] stated that the averaging method in the above model brings high deviations. According to the same geometric principle, the dilute phase discharged from every single flight was calculated separately. The instantaneous total particle ratio of the dilute phase could be determined by

$$f_{di} = \sum_{i=1}^{n_F} \left(-\omega_D \cdot \frac{df_{F,i}(\delta)}{d\delta} \right) \cdot t_{F,i}. \tag{2.14}$$

Where, $t_{F,i}$ is the falling time of solids discharged from the i^{th} flight; $f_{F,i}$ is the holdup ratio of the i^{th} flight, respectively.

Based on these studies, Sunkara et al. [38] proposed that the particle ratio of dilute phase should be only related to the number of active flights $n_{F,a}$ rather than the total flights number n_F. Thus, the expression for the average ratio of the dilute phase was given by

$$f_{di} = n_{F,a} \cdot \overline{f_{di,i}}. \tag{2.15}$$

Where, $n_{F,a} = \delta_L/360° \cdot n_F$. Moreover, $\overline{f_{di,i}}$ is the average ratio of a single i^{th} curtain, which was defined by

$$\overline{f_{di,i}} = \frac{1}{\delta_L} \cdot \int_0^{\delta_L} \left(\sqrt{2 \cdot Fr \cdot \frac{h_F}{R}} \cdot \left(-\frac{df_F(\delta)}{d\delta} \right) \right) d\delta. \tag{2.16}$$

2.2 Experimental methods

To investigate the particle motion in FRD, two measurement techniques are generally used to study the particle motion, which are the dyed tracer tracking method and the image analysis method.

2.2.1 Dyed tracer tracking method

Danckwerts [39] first reported the application of dye tracer tracking technology in a kiln, which was used to determine the residence time distribution of solids. Undyed powder was fed into the kiln at a constant feed rate. At the steady state, the kiln was turned off for approximately one minute to inject tracer particles (black color) into the kiln. At the kiln outlet, mixtures of the undyed material and tracer were then manually collected in 30 s intervals. Samples were collected until black tracer powder was no longer visible. Based on this method, Njeng et al. [40–42] studied the residence time distribution and axial dispersion for the continuous flow of sand and broken rice in an FRD. In 2017, Paredes et al. [43] investigated the axial movement of dry cohesive powders in an FRD. The mean residence time was measured and the dyed tracer concentration that corresponds to the axial dispersion coefficient was determined using a spectrophotometer, following a methodology developed by Emady et al. [44].

2.2.2 Image analysis method

In recent years, image analysis methods have been widely used in drum research. By continuously taking pictures, the particle movement process in the cross-section of the FRD can be recorded. Many parameters are displayed directly in the experimental image, e.g. dynamic angle of repose, kinetic angle of repose, first and final discharge angle of flight. Through further analysis and processing, the loading and unloading characteristics of a flight, and particle distribution in three phases (flights, dense bed, dilute bed) can be also obtained from images.

Based on the development of technology, the use of image analysis methods in FRD research can be divided in three stages. Initially, the parameters in images were measured manually. With the help of length and angle scales, the kinetic angle of repose in a flight at a specific angular position was measured under various drum operating conditions [45, 46]. Besides, the holdup of flights was estimated by integrating solid-filled areas from the pictures [5, 28–30, 47].

Then, the image processing software ImageJ became popular in the analysis of drum processes. It can measure distances and angles, calculate the area of user-defined sections, and conduct pixel value statistics of intensity-thresholded objects [48]. Using these features of ImageJ, it is much easier and more accurate to measure the kinetic angle of repose and the particle area in the regions of flight phase or bed phase. The optimum filling degree of the FRD was determined by confirming the precise angle location of the FUF [2, 49]. The performance of simple and complex flights was evaluated by measuring the loading and unloading profiles of the flights [8, 32]. Besides, these data obtained through image analysis played an important role in the process of model development and validation. Lee and Sheehan [35] observed that the unloading of flights was discontinuous from images. Thus,

the average of the measured surface angle was substituted into the proposed geometric model to calculate the total surface area of solids in the flight. In addition, Sunkara et al. [38] derived the characteristics of the dilute phase through photo analysis. In drum images, the cross-sectional area of the dilute phase was estimated by subtracting the areas of the dense phase and the flight phase from the total filling area of the drum. However, it is still necessary to manually mark and select the target areas when using ImageJ. This process is very time consuming and eye straining when analyzing a large number of images, and it is easy to introduce errors artificially.

To facilitate image analysis, semi-automated processing methods were developed by combining the aforementioned ImageJ software with the Matlab image processing toolbox [50, 51]. Specifically, ImageJ was used for the image preprocessing, including contrast enhancement, filtering and thresholding. Matlab codes were then adapted to calculate the actual area of interesting solids containing regions in the cross-section of the drum. In actual operations, the airborne phase area and the drum edges were first removed from the images, and then a pixel intensity threshold was used to cut off the flight components, thereby retaining only solids of the flight phase [52]. Based on this technology, four criteria for determining the drum design loading were introduced and compared. The results indicated that the areas of FUF provided a more suitable way to estimate the design load. Following this work, Karali et al. [51] identified the influence of drum operating conditions on the optimum loading of the drum by a semi-automated image analysis method, as the side view of materials in flights had to be manually selected. Though, some problems were noted when applying the automated image analysis method. The light locations need to be adjusted to avoid any reflections on the drum frontal cover wall, and the camera location needs to be optimized to decrease the appearance of the material's side view [53]. Moreover, it is still challenging to accurately identify the separating edges between the solids frontal cross-section area and its side view during image analysis. Further, this method cannot directly measure the particle ratio of the dilute phase, as it is difficult to determine the void ratio of the falling curtains. These problems limit the effective application of the semi-automated method.

2.3 Numerical simulations

With the development in computational power and mathematical algorithms, numerical simulations are popularly used to investigate particle and fluid flows. During the past decade, several numerical studies conducted by using the computational fluid dynamics (CFD) and discrete element method (DEM) were published related to the particle motion in FRD.

2.3.1 Computational fluid dynamics method

In 2012, Ajayi and Sheehan [52] studied the mass of airborne solids in the FRD at design loading. The voidage and shape of free falling particle curtains of the discharging flight at the angle position of 150 ° were modeled by using CFD Eulerian-Eulerian approach. Based on the simulation results, the volume fraction of falling particles was estimated. Besides, the height of the curtains was investigated from the CFD data.

Using the same method, Nascimento et al. [54] studied the effect of solid properties and drum operating conditions on the holdup of a flight. Through numerical calculation, the solid volume fraction calculated by grid interpolation method was displayed in 20 colors in the software of FLUENT. Each color represented a range of solid volume fractions. Using ImageJ to measure the area of each color, the holdup of a flight was calculated by summing the masses corresponding to each color in the flight.

Another study was reported by Machado et al. [55], who investigated the holdup of a single flight and the height of material bed based on CFD simulations. A rotary drum with one flight was utilized in this work. To ensure the accuracy of the simulation results, the effect of numerical parameters on particle motion was studied by using different values of specularity coefficient and particle-particle restitution coefficient in the CFD simulations. The specularity coefficient is an empirical parameter qualifying the nature of particle-wall collisions and ranges from 0 for perfect specular collisions to 1 for perfectly diffuse collisions depending on the roughness of the wall [56].

2.3.2 Discrete element method

In 2008, Vargas et al. [20] developed a 2D-DEM model to study the segregation of bi-disperse (size or density) particle systems in the FRD. The effect of the location of flights, at the central axis of the drum or at the inner side of the rotating wall, was estimated with 50 % filling degree at 6 rpm. The results showed that the flights installed at the central axis dramatically decreased the segregation of bi-disperse particles compared to the flights fixed on the inner wall of the drum. Following this work, Jiang et al. [19] considered flights of different shapes at the central axis of a drum to check their mixing performance for a bi-disperse particle system. The results from a series of DEM simulations indicated that the mixing efficiency of flights with shape of '+' (cross-flights with four blades) and '∗' (flights with six blades) was higher than that of shape '-'.

In addition to the particle size, the shape of particles is also a research hotspot in DEM simulations. Geng et al. [57] developed a 3D-DEM model to investigate the mixing behavior of spherical particles and slender particles. The results showed that the mixing rate could be improved with higher rotating speed of the drum and larger radius of cylindrical flights. Compared to spherical particles, the slender particles were faster to attain a state of mixedness. Similar simulations were performed on the movement of filamentous particles

in a 2D-FRD. These works confirmed that increasing the flight length or drum rotating speed can accelerate the particle mixing process in the FRD. Subsequently, a 3D simulation was developed to study the residence time distribution of flexible ribbon particles [58]. Each particle was divided into three rigid segments, connected by two hinge constraints. The air drag force was considered for each particle, but the influence of particles on air flow was not considered. At higher drum rotating speeds, the normal distribution of residence time became wider. Besides, the mean particle residence time was reduced significantly with the increasing of drum rotating speed, and decreased moderately with the increasing of drum slope or the initial velocity of air flow.

In 2016, Zhou et al. [59] simulated the transverse mixing of particles with various cohesion values in FRD. Four radial flights with different length were utilized and the particle mixing behavior was characterized by the mixing time and mixing entropy. The insertion of flights improved the transverse mixing performance of cohesive particles. In fact, the enhancement in mixing from flights with optimal length was more obvious for highly cohesive particles than for particles with low cohesion.

The influence of flight design (shape, placement, dimension and number) on the binary mixture (size, density and shape) segregation was also investigated by DEM simulations [60–62]. Besides, Xie et al. [63] modeled the conductive heat transfer in the drum with different types of flights at various drum rotating speeds. In addition, Scherer et al. [64] studied the convective drying of wood chips in the FRDs by using coupled DEM and CFD simulation.

2.4 Summary

Among literature studies either geometrical models, experimental measurements, or numerical simulations are presented independently and without comparison with each other. Moreover, studies have mainly focused on determining the particle residence time, holdup or discharging behavior of flights. Details of particle motion in FRD, especially for the dense bed phase and the dilute phase, are still unclear to researchers and equipment producers. Furthermore, the experimental methods for investigating particle motion are quite limited, although experimental data would be very important for model development and numerical simulation validation. Therefore, the present study focuses on particle motion in FRD, by using new experimental methods.

Chapter 3

Magnetic particle tracking methodology

This chapter is based on Zhang et al. [65].

The principle of the MPT method is based on tracking of a single magnetic marker. Specifically, a small permanent magnet is inserted into a particle of the respective bed material. This particle is then embedded into the granular bed acting as a tracer particle. Evaluation of the quasi-static magnetic field results in a three-dimensional position and orientation of the tracer at each time step.

Due to the ability to record particle trajectories, the MPT technique has successfully been used to study particle motion, mixing and segregation for several cases of dense granular flow, especially in prismatic spouted beds and fluidized beds [18,66–69]. Compared to the radioactive tracking and PEPT methods, MPT has lower costs and is safer. It is also worth to note that MPT has the advantage of measuring particle position and orientation simultaneously, thus obtaining the particle rotational velocity, which is not possible by other tracking techniques. As yet, the MPT technique has not been used to investigate the particle motion in rotary drums, either non-flighted or flighted.

3.1 Magnetic tracking technique

Modern magnetic materials such as neodymium magnets (also known as NdFeB) and samarium–cobalt magnets provide a high magnetic moment. As a magnetic marker, they could provide strong magnetic field signals even in a magnetically unshielded environment. Magnetic tracking is an inverse problem with five degrees of freedom, three for position and two for orientation. When the magnetic moment of the magnetic marker is unknown, this can act as a sixth degree of freedom. The magnetic field is measured by several sensors that are positioned in a known configuration.

To identify the position of a permanent magnet with a certain magnetic moment, the quasi-static stray magnetic field around it is analyzed. With the help of Maxwell's equations [70], the macroscopic properties of electromagnetic fields are described, including the electric field intensity $\mathbf{E}$, magnetic field intensity $\mathbf{H}$, magnetic flux density $\mathbf{B}$ in vacuum, electric charge density ρ_v, magnetic shift density $\mathbf{D}$ and electric current density $\mathbf{J}$ as

$$\nabla \cdot \mathbf{D} = \rho_v, \tag{3.1}$$

$$\nabla \cdot \mathbf{B} = 0, \tag{3.2}$$

$$\nabla \times \mathbf{H} = \frac{\delta \mathbf{D}}{\delta t} + \mathbf{J}, \tag{3.3}$$

$$\nabla \times \mathbf{E} = -\frac{\delta \mathbf{B}}{\delta t}. \tag{3.4}$$

Based on these equations, the theoretical magnetic field intensity $\mathbf{H}$ around a dipole at $\mathbf{r}_i$ (described by the Cartesian coordinates x_0, y_0, z_0 and the spherical coordinates (θ_0, φ_0) measured at sensor i (see Fig. 3.1) can be expressed according to Richert et al. [71] as

$$\mathbf{H}(\mathbf{r}_i, \boldsymbol{\mu}_m) = \frac{1}{4\pi}\left(- \frac{\boldsymbol{\mu}_m}{r^3} + \frac{3(\boldsymbol{\mu}_m \cdot \mathbf{r}_i)\mathbf{r}_i}{r^5}\right). \tag{3.5}$$

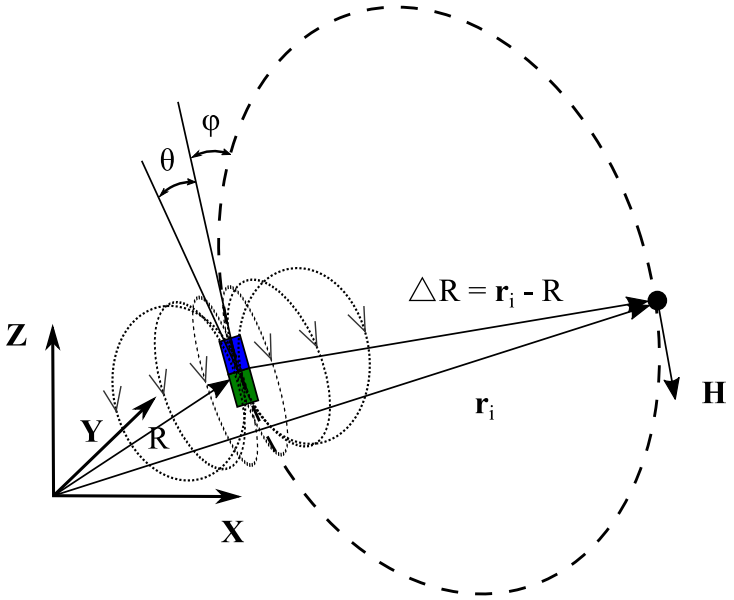

Figure 3.1: Field distribution around a magnet, and coordinate system.

In this equation, the magnetic moment of the dipole $\boldsymbol{\mu}_m$ in spherical coordinates is

calculated by

$$\boldsymbol{\mu}_m = \boldsymbol{\mu}_{m_0} \left(sin\theta_0 cos\varphi_0, sin\theta_0 sin\varphi_0, cos\theta_0 \right). \tag{3.6}$$

The magnetic moment of magnitude $\boldsymbol{\mu}_{m_0}$ is equal to the saturation magnetization of the (NdFeB-based) magnet times the volume of the magnet. The position vector of dipole $\mathbf{r}_i$ is defined as

$$\mathbf{r}_i = \left(x_i - x_0, y_i - y_0, z_i - z_0 \right). \tag{3.7}$$

To determine the actual position and orientation of the magnetic marker, all utilized sensor signals must be calculated. The optimization algorithm minimizes the differences between measured and simulated magnetic field strengths by varying the position and orientation of the simulated magnetic marker using a quality function. This quality function indicates the accuracy of the solution, which is expressed by

$$Q = \sum_{i=1}^{N_s} \frac{[\mathbf{H}(\mathbf{r}_i, \boldsymbol{\mu}_m)_i^{Measurement} - \mathbf{H}(\mathbf{r}_i, \boldsymbol{\mu}_m)_i^{Prediction}]^2}{\triangle \mathbf{H_i}^2}. \tag{3.8}$$

Here, N_s denotes the number of sensors. The Q value, which is calculated as the sum of the squared differences between measured and simulated magnetic field intensity, should be as small as possible to get a high probability of the true position (x_0, y_0, z_0) and the orientation (θ_0, φ_0) of the dipole. Many sensors with appropriate arrangement are expected to achieve a higher data accuracy and a better coverage of the measuring volume.

3.2 MPT method verification

The magnetic material NdFeB, which can provide a high magnetic moment, is commonly used to make tracers. In actual operation, a certain volume of magnet is embedded in a bed of particles. In this way, the size of the tracer particle should be the same as that of the original particles. However, the density of the tracer particle is likely to be higher than that of other particles, as the density of NdFeB magnet is quite high (7300 - 7700 kg/m^3). This change in density may affect the motion dynamics of the tracer particle.

As reported in several studies on unbaffled rotary drums, density differences in binary particle systems caused radial segregation in the granular bed, but did not induce axial particle segregation even at density ratios up to 4.9 [72–74]. Moreover, Yamamoto et al. [75] investigated the effect of particle density on the mixing behavior of particles in a rotating drum with four flights with 30 % filling degree by experiments and DEM numerical simulations. The results indicated that flights can control the moving behavior of both, higher and lower density particles, decreasing the segregation greatly. In addition, it was confirmed that the segregation of particles with different densities decreased in the rotary drum as the filling degree was reduced [76–78]. Therefore, with a small filling degree of

the FRD, the effect of density difference on particle motion at the bottom of the drum and on the flights can be expected to be negligible.

In the region of dilute phase, the velocity differences between the original particles and the tracer particle are also analyzed. The motion of particles in the dilute region is mainly influenced by gravity and the drag force. The buoyancy, pressure gradient force and Basset force are not accounted for, since they are of minor importance for the high density ratio flows $(\rho_p/\rho_g) >> 1$ considered in this study. The particle motion is described by

$$\mathbf{a} = \frac{du_p}{dt} = \frac{m_p g - F_D}{m_p}, \tag{3.9}$$

where $\mathbf{a}$ is the particle acceleration and m_p is the mass of an individual particle. The drag force is expressed by

$$F_D = \frac{1}{2}\rho_g C_D A \cdot u_r^2, \tag{3.10}$$

where ρ_g is the mass density of gas, A is the cross-sectional area of the particle and u_r is the velocity of particle relative to gas. C_D is the drag coefficient which is dependent on the Reynolds number

$$Re = \frac{\rho_g d_p u_r}{\mu_g}; \tag{3.11}$$

(μ_g: dynamic viscosity of gas, d_p: particle diameter).

Conditions of the present work correspond to Reynolds numbers in the transition region $(1 < Re < 1000)$ [79], so that the drag coefficient can be calculated as [80]

$$C_D = \frac{24\,(1 + 0.15Re^{0.687})}{Re}. \tag{3.12}$$

Combining Eqs. 3.10, 3.11 and 3.12, the drag force is expressed as

$$F_D = 3\pi\mu_g d_p u_r + 0.9\pi\mu_g^{0.313}\rho_g^{0.687}d_p^{1.687}u_r^{1.687}. \tag{3.13}$$

Considering unidirectional free fall, the particle velocity is obtained from Equations 3.13 and 3.9 as a function of the falling height to

$$u_p^2 = 2h\left(g - \frac{18\mu_g u_p}{\rho_p d_p^2} - \frac{5.4\mu_g^{0.313}\rho_g^{0.687}u_p^{1.687}}{\rho_p d_p^{1.313}}\right). \tag{3.14}$$

With the above equation, particle instantaneous velocity corresponding to a certain height of fall can be calculated by the Newton iteration method. To compare the velocity difference between original particle and tracer, five different falling heights are selected and the corresponding particle velocities are calculated for the case of plastic balls, as listed in Table 3.1. The results show that the higher the falling height, the bigger is the velocity difference between the original particle and the tracer.

Moreover, the results show that there is only 1.7 % velocity difference between plastic balls and the corresponding tracer when the falling height is assumed to be 0.194 m (diameter of the drum). The velocity comparison in the case of soybeans (see Chapter 5) has also been conducted by introducing a shape correction factor in the calculation of drag force and still a negligible velocity difference has been obtained. Based on these studies, representative results both in the dense phase region and in the dilute phase region can be expected.

Table 3.1: Velocity comparison for free fall between plastic balls and the corresponding magnetic tracer.

Falling height h (m)	Plastic balls velocity u_p (m/s)	Tracer velocity u_t (m/s)	Velocity difference $\frac{u_t - u_p}{u_p} \times 100$ (%)
0.034	0.812	0.815	0.369
0.074	1.191	1.200	0.756
0.114	1.471	1.487	1.088
0.154	1.702	1.725	1.351
0.194	1.902	1.934	1.682

Chapter 4

Particle tracking velocimetry method

Parts of this chapter are based on Zhang et al. [81].

Applications of the PTV technique in various granular flows have been widely reported in the last decade. The velocity characteristics of spherical or non-spherical particles in vibrated bed were successfully measured by the PTV method [82, 83]. Small-scale flow patterns of colored particles in a wind tunnel were investigated by using 3D-PTV technique [84]. Kartushinsky et al. [85] also used the PTV method and studied the dispersion of solid particles in a turbulent gas flow. Gopalan et al. [86] measured the pressure drop and particle velocities in a pseudo 2D rectangular fluidized bed. There are also further applications of PTV technology in fluidized beds. Hagemeier et al. [87] accurately investigated the particle dynamics in 2D under various operating conditions. Based on the results, Jiang et al. [88, 89] developed further the PTV technique to systematically estimate particle collision frequency and investigate the velocities of individual particles with different sizes marked by distinguishable colors. Besides, Meyer et al. [90] presented results on particle exchange rates at weirs in horizontal fluidized beds. The fluidization behavior of non-spherical particles was investigated by Vollmari et al. [91].

In a rotary drum without flights, Chou et al. [92] utilized the PTV technique to analyze the dynamic characteristics and velocity distributions of particles under different operating conditions. So far, there is no report on the application of the PTV method to an FRD.

Generally, two processes are contained in particle tracking velocimetry to track the motion of individual particles on the basis of raw grayscale images: particle segregation and particle tracking. Specifically, particle segregation is for identifying particles in each frame and recording their centroid positions. The particle tracking process iteratively matches the identified particles in two subsequent frames. Trajectories and translational velocities of the paired particles are obtained by combining particle displacement and

the duration of the time interval between frames. The algorithms of both procedures are introduced in detail in this chapter.

4.1 Particle segmentation algorithm

In digital images, the intensity pattern of relatively big and spherical particle always has a clear peak in the center, and the intensity concentrically decreases as the distance from the central location increases. According to this feature, Takehara and Etoh [93] proposed a *particle mask correlation method* to identify particles in an image and detect their geometric centers accurately. In this process, all areas that have similar intensity distributions as the particle mask will be segregated as particles, regardless of whether they are a true particle image. Therefore, an intensity recheck procedure is recommended to eliminate interfering particles from the particles identified by the particle mask correlation method [88].

4.1.1 Particle mask correlation method

The flow chart of the particle-mask correlation method is shown in Fig. 4.1. A typical intensity pattern of a spherical particle image is firstly selected as the particle mask [93], with the matrix size of $m \times m$ pixels. Then, this particle mask is scanned over the entire image plane, and the normalized cross-correlation coefficient is calculated at each pixel location depending on the intensity pattern. The normalized cross-correlation coefficient γ_{coef} between the particle mask centered at (x_0, y_0), and the interrogation area with the same size in raw image centered also at (x_0, y_0), is calculated as

$$\gamma_{coef}(x_0, y_0) = \frac{\sum_{i=x_0-m/2}^{x_0+m/2} \sum_{j=y_0-m/2}^{y_0+m/2} [I(i,j) - \bar{I}][s(i,j) - \bar{s}]}{\sqrt{\sum_{i=x_0-m/2}^{x_0+m/2} \sum_{j=y_0-m/2}^{y_0+m/2} [I(i,j) - \bar{I}]^2 \sum_{i=x_0-m/2}^{x_0+m/2} \sum_{j=y_0-m/2}^{y_0+m/2} [s(i,j) - \bar{s}]^2}}. \quad (4.1)$$

Here, $I(i,j)$ is the intensity value in the matrix of the interrogation region in the raw image. $s(i,j)$ is the intensity value in the matrix of the particle mask. $\bar{I}$ and $\bar{s}$ are the corresponding spatial-averaged intensities for the interrogation region in the raw image and the particle mask.

The normalized cross-correlation coefficient between the particle mask and linear elements on the raw image always has a low value. Thus, the linear elements can be automatically eliminated during the segmentation process [94]. According to Eq. 4.1, the normalized cross-correlation coefficient depends on the intensity pattern. Thus, only particles with complete contour like the particle mask are identified.

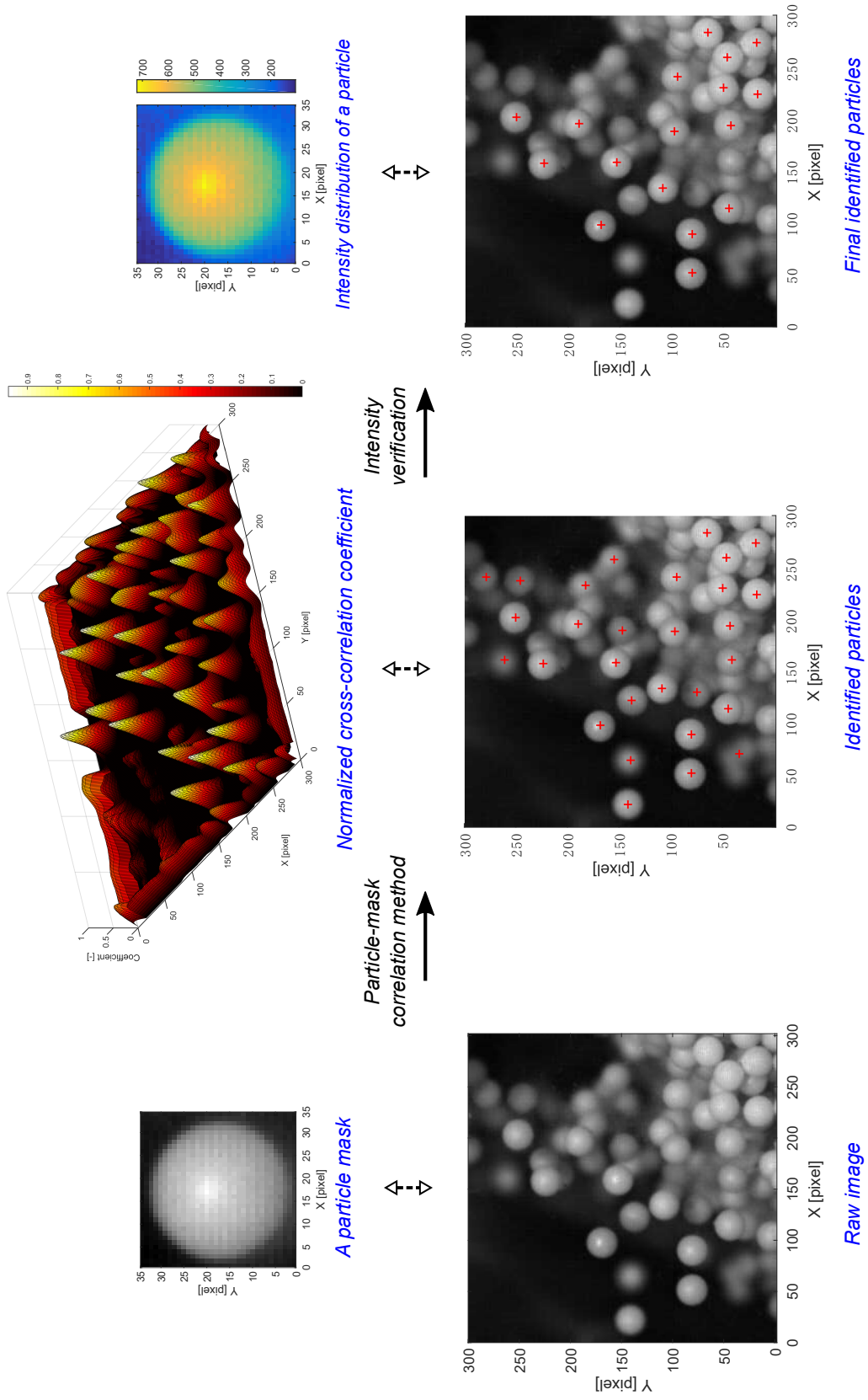

Figure 4.1: Flow diagram of the particle mask correlation method for particle segmentation.

A coefficient value close to 1.0 will be obtained if the intensity pattern distribution of the interrogation region is similar to the assumed particle mask. An obtained matrix of the normalized cross-correlation coefficient is shown in Fig. 4.1, the peaks correspond to the centers of particles in the raw image. Thus, the locations of peaks are identified by median filtering and convolution in image processing.

4.1.2 Intensity verification

Based on the intensity distribution pattern, the particle mask correlation method is quite sensitive. Even it is not a particle image, an interrogation region with a similar intensity pattern as the particle mask is still extracted by this process [93]. Besides, unfocused and very blurry particles in the image plane that may not be of interest for the study are also identified. These particles have similar intensity distributions, but the intensity values are much lower. In order to solve this problem, it is recommended to carry out an intensity recheck process [88]. An intensity constant is averaged based on the brightness values of all pixels of a typical particle image. Mean intensities of the particles detected by the particle mask correlation method are separately calculated and compared with the intensity constant. If the mean intensity of an identified particle is less than the intensity constant, this particle will be removed from the database as depicted in Fig. 4.1. After this process, the centroids of obtained particles (x, y) in each image are stored for particle tracking in the next procedure.

4.2 Particle tracking algorithms

Particle tracking is carried out by pairing the same particle in two or more consecutive images. In the flow of particles in FRD, dense and dilute particle phases coexist and are constantly transformed into each other. Besides, velocity fluctuations are caused by particle-particle collisions and particle-wall collisions. Therefore, a robust and reliable image tracking algorithm should be used to track the movement of many individual particles simultaneously. There are two tracking algorithms that are widely applied in PTV technique to track particles in complex flows.

4.2.1 Voronoi tracking method

With the centroids of identified particles, the flow chart of the Voronoi tracking method is depicted in Fig. 4.2. Voronoi diagram is a geometrical construction which is generated based on a set of given points. With these points, the Voronoi diagram divides the plane into a set of polytopes according to the nearest-neighbor rule. Each point is associated with the region of the plane closest to it [95].

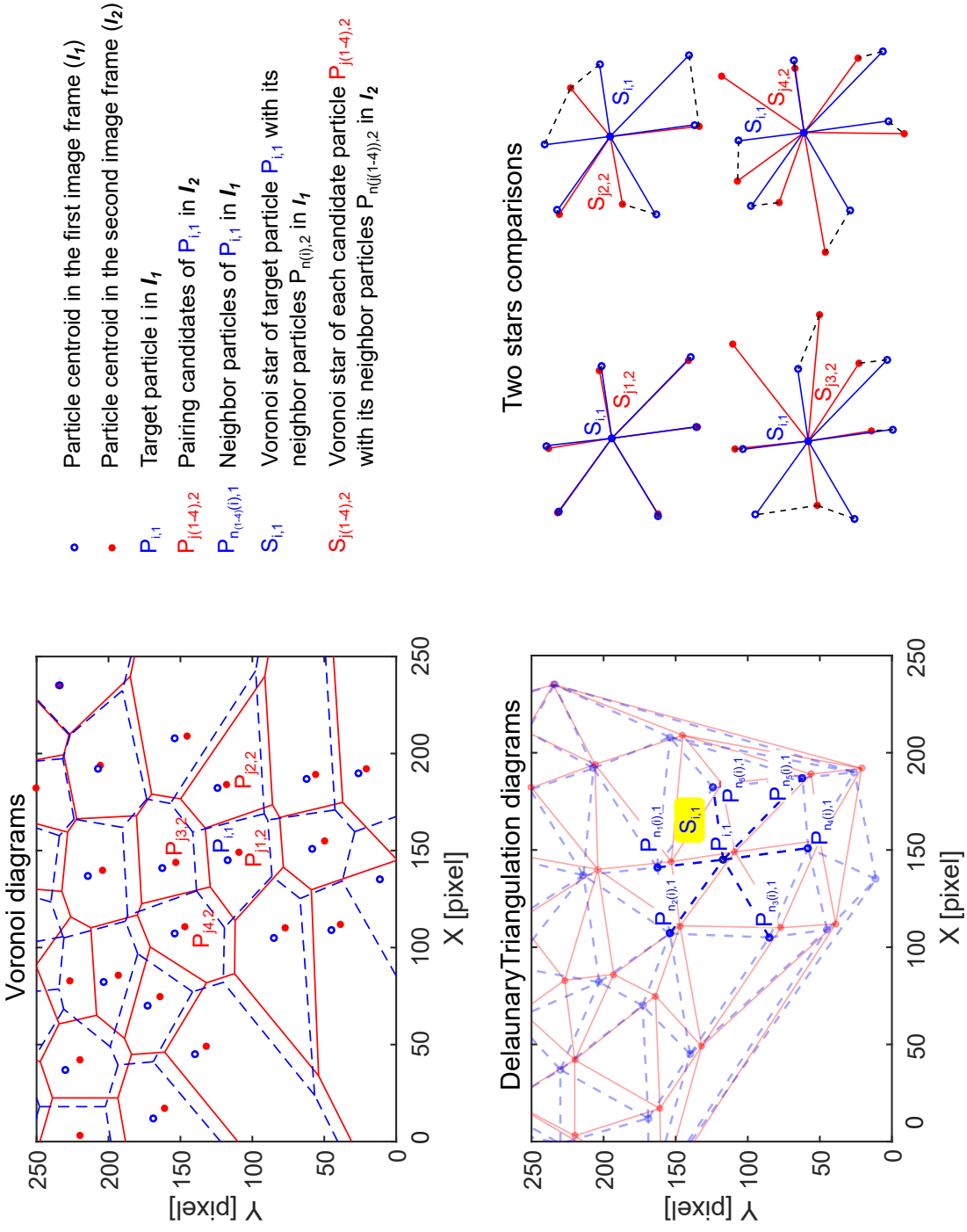

Figure 4.2: Flow diagram of the Voronoi algorithm for particle tracking.

Capart et al. [96] originally applied the Voronoi structure to pair particles in two consecutive frames by assuming that the local Voronoi pattern formed by neighboring particles will remain stable in two or multiple consecutive images. Later, the Voronoi tracking algorithm is widely and successfully applied to analyze the motion of granular flows in 2D and 3D, with spherical and non-spherical particles [87, 92, 97, 98].

The Voronoi plot construction and the matching algorithm are carried out as follows:

1. The Voronoi diagrams for two consecutive images (I_1 and I_2) are constructed based on the particle centroids obtained from particle segregation. Each Voronoi cell (polygonal region) associates with a particle centroid and contains the region of the image plane which is closest to this particle. Particles that share an edge of Voronoi cells are termed 'natural neighbors' of each other.

2. Delaunay triangulation is established by all connections between an arbitrary target particle and its 'natural neighbors'. The Voronoi star $S_{i,1}$ of target particle $P_{i,1}$ is built by the target particle (center of star) and the corresponding neighbors $P_{n(i),1}$ (extremities of the star).

3. The distances between target particle in the first frame $P_{i,1}$ and all particles in the second frame I_2 are calculated according to

$$dis(P_i, P_j) = \sqrt{(x_i - x_j)^2 + (y_i - y_j)^2}. \tag{4.2}$$

   Four particles in the second frame with the nearest distances obtained from

$$match(P_{i,1}) = min_{P_{j,2}}(dis(P_{i,1}, P_{j,2})) \tag{4.3}$$

   are selected as the match candidates $P_{j(1-4),2}$ of $P_{i,1}$. The Voronoi star of each candidate particle $S_{j(1-4),2}$ is established in the same way.

4. To identify the best match particle from candidates in I_2 for the target particle in I_1, the star $S_{i,1}$ is moved to coincide with the corresponding stars of candidate particles $S_{j(1-4),2}$ for calculating the discrepancy of Voronoi stars $dis_s(S_{i,1}, S_{j,2})$, according to

$$dis_S(S_1, S_2) = median_{k_1(1-N_1)}[min_{k_2(1-N_2)}|(\boldsymbol{r}_{k_1,1} - \boldsymbol{r}_{0,1}) - (\boldsymbol{r}_{k_2,2} - \boldsymbol{r}_{0,2})|]. \tag{4.4}$$

   Minimum distance from each extremity of $S_{i,1}$ to the nearest extremities of $S_{j,2}$ is calculated and stored in a vector. This method allows comparisons between any two stars, without the requirement of them having the same number of extremities in the individual stars.

5. Median value of the obtained vectors is estimated by Eq. 4.4 to reflect the matching quality of two stars. The minimal median corresponds to the best match of target

particle.

With a successful matching, the displacement of the target particle in two consecutive images can be easily calculated based on the centroids. The particle velocity is then obtained by combining the displacement with the time interval of two consecutive images.

4.2.2 Probability relaxation method

The probability relaxation method was first developed by Barnard and Thompson [99] to match images in real-world scenes by specifying the geometrical disparity between them. Then, Baek and Lee [100] successfully implemented the probability relaxation method to track particles based on an iterative estimation of the match probability. Hereafter, improvements of the probability relaxation method for particle tracking are introduced and applied to study particles motion in many complex granular flows [94, 101, 102].

This method assumes that a group of particles in a small area have similar movements in a sufficiently short time interval. These particles move under a quasi-rigid condition, even with small velocity variations. By calculating the total probability of neighboring particles meeting the quasi-rigid condition, the target particle in the first frame is iteratively paired with one of its candidate particles in the second frame.

Like the Voronoi tracking method, the probability relaxation method is based on the particle centroids identified in consecutive images I_1 and I_2. The schematic diagram of the probability relaxation algorithm is represented in Fig. 4.3.

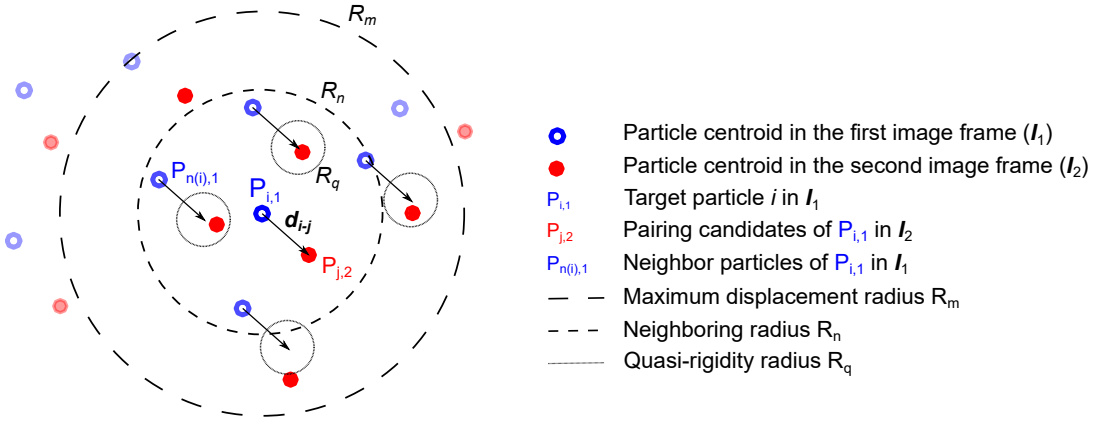

Figure 4.3: Flow diagram of the probability relaxation method.

The detailed process of the probability relaxation method, originally developed by Baek and Lee [100], is as follows:

1. For a target particle $P_{i,1}$ in I_1, maximum displacement radius R_m is defined to find the candidate particles $P_{j,2}$ in I_2. The displacement vector $\boldsymbol{d}_{i-j}$ between target

particle and its pairing candidate particles should meet the following condition:

$$|\boldsymbol{d}_{i-j}| = |dis(P_{i,1}, P_{j,2})| < R_m. \tag{4.5}$$

2. Neighboring radius R_n is applied to find the neighboring particles $P_{n(i),1}$ around the target particle P_i in I_1. Similarly, the pairing candidates of each neighboring particle $P_{n(i),1}$ in I_2 are searched by the maximum displacement radius R_m, which is expressed as $P_{j(n),2}$.

3. According to the quasi-rigidity condition, the target particle and its neighboring particles should have similar motions in two consecutive frames. Thus, the displacement vector $\boldsymbol{d}_{i-j}$ between $P_{i,1}$ and $P_{j,2}$, and the displacement vector $\boldsymbol{d}_{n(i)-j(n)}$ between $P_{n(i),1}$ and $P_{j(n),2}$ are required to satisfy the following condition:

$$|\boldsymbol{d}_{i-j} - \boldsymbol{d}_{n(i)-j(n)}| < R_q. \tag{4.6}$$

   Where, R_q is termed as quasi-rigidity radius and needs to be predefined. Otherwise, this neighboring particle cannot be used to update the matching probability $\mathbf{P}_{ij}$ of each candidate particle to the target particle.

4. To evaluate the matching degree between target particle $P_{i,1}$ and the corresponding candidates $P_{j,2}$, match probability $\mathbf{P}_{ij}$ and no-match probability $\mathbf{P}_i^*$ are defined. $\mathbf{P}_{ij}$ is the matching probability of each candidate particle to $P_{i,1}$, and $\mathbf{P}_i^*$ indicates the probability that $P_{i,1}$ has no matching particle in the 2^{nd} frame. They have the following relationship:

$$\sum_{j=1}^{N_{j(i)}} \mathbf{P}_{ij} + \mathbf{P}_i^* = 1. \tag{4.7}$$

   Where, $N_{j(i)}$ is the total number of candidate particles in the 2^{nd} frame $P_{j,2}$ for the target particle in the 1^{st} frame $P_{i,1}$. The initial value of the probabilities ($\mathbf{P}_{ij}^{(0)}$ and $\mathbf{P}_i^{*(0)}$) are given as

$$\mathbf{P}_{ij}^{(0)} = \mathbf{P}_i^{*(0)} = \frac{1}{N_{j(i)} + 1}. \tag{4.8}$$

5. As mentioned before, the target particle and its neighboring particles undergo a quasi-rigid motion. Therefore, the contribution of all neighboring particles is considered in the tracking algorithm. The sum of matching probability of neighboring particles $\mathbf{Q}_{ij}$ and the corresponding pairing candidates are iteratively calculated by

$$\mathbf{Q}_{ij}^{(n-1)} = \sum_{n(i)=1}^{N_{n(i)}} \sum_{j(n)=1}^{N_{j(n)}} \mathbf{P}_{n(i)j(n)}^{(n-1)}. \tag{4.9}$$

Here, the superscript $(n-1)$ denotes the iteration step. $N_{n(i)}$ is the total number of neighboring particles $P_{n(i),1}$ of target particle $P_{i,1}$. $N_{j(n)}$ represents the total number of the candidate particles $P_{j(n),2}$ of the neighboring particle $P_{n(i),1}$.

6. Combining $\mathbf{P}_{ij}$ and $\mathbf{Q}_{ij}$, the matching probability $\mathbf{P}_{ij}$ is updated by an iteration formula:

$$\widetilde{\mathbf{P}}_{ij}^{(n)} = A \cdot \mathbf{P}_{ij}^{(n-1)} + B \cdot \mathbf{Q}_{ij}^{(n-1)}. \tag{4.10}$$

Where $A(< 1)$ and $B(> 1)$ are constants that affect the convergence speed of the iteration. The values of A and B are 0.3 and 4.0, respectively. $\widetilde{\mathbf{P}}_{ij}^{(n)}$ is the non-normalized probability that is normalized before next iteration step by

$$\mathbf{P}_{i,j}^{(n)} = \frac{\widetilde{\mathbf{P}}_{i,j}^{(n)}}{\sum_{j=1}^{N_{j(i)}} \widetilde{\mathbf{P}}_{i,j}^{(n)} + \mathbf{P}_{i}^{*(n-1)}}, \tag{4.11}$$

$$\mathbf{P}_{i}^{*(n)} = \frac{\mathbf{P}_{i}^{*(n-1)}}{\sum_{j=1}^{N_{j(i)}} \widetilde{\mathbf{P}}_{i,j}^{(n)} + \mathbf{P}_{i}^{*(n-1)}}. \tag{4.12}$$

In theory, the correctly matching particles have a high probability value (close to unity), while the matching probability value of other particles is very low. Therefore, the most probable matching particle of the target particle is the candidate having the maximum matching probability ($max(\mathbf{P}_{ij})$). The velocity vector of the target particle is calculated using the tracked displacement vector $\boldsymbol{d}_{ij}$ and the time interval between two consecutive images.

4.3 PTV method verification

4.3.1 Verification of particle segmentation

An optimized particle segmentation methodology is applied to the raw, grayscale images to identify the particles in FRD. This optimized segmentation method combines the particle-mask correlation method and a regional intensity verification process to detect the centroids of individual particles in each image.

In the particle mask correlation method, a fixed size of particle mask $m \times m$ is applied to calculate the correlation coefficient value, as shown in Eq. 4.1. To improve the performance of particle segmentation, three square matrices are chosen from raw images as candidates for particle mask in this study. As shown in Fig. 4.4, their edge sizes m are 30 pixels ($\approx d_p \cdot S_f$), 22 pixels ($\approx \sqrt{2}/2 \cdot d_p \cdot S_f$) and 16 pixels ($\approx 1/2 \cdot d_p \cdot S_f$), respectively. For each candidate matrix, ten complete and smooth particles are selected manually from raw images. The intensity patterns of these particles are averaged to obtain an intensity pattern distribution of the particle mask, which eliminates the influence of random noisy pixels.

As introduced in Section 4.1.2, an interrogation region which is not a particle image or is a very blurry particle image will still be identified if it has a similar intensity pattern as the particle mask. In the raw images obtained from our experiments, dilute phase particles are visible from different positions in the axial direction of the FRD as shown in Fig. 4.4. With the typical intensity pattern, even dilute phase particles which are far away from the front wall are easily recognized by the particle mask correlation method. However, these particles do not belong to the first layer on the transparent drum front and should not be included in the subsequent analysis of this study. To remove these interfering particles, an intensity verification process is performed by evaluating the mean intensity of each detected particle. It is worth noting that the mean intensity of particles in FRD is affected by many factors, including the shade effects of the rotating wall or flights and the non-uniform intensity distribution of illumination.

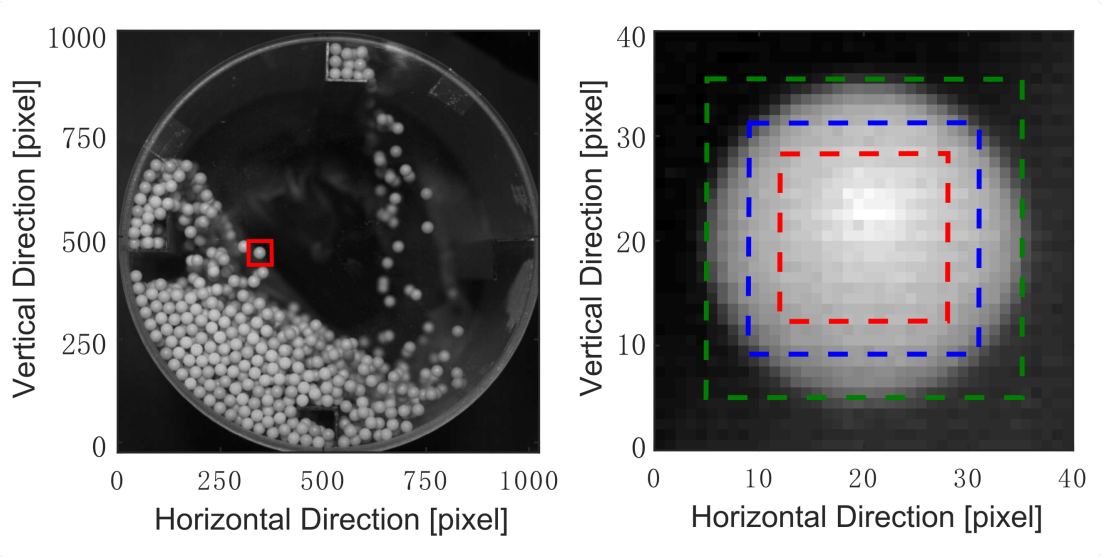

Figure 4.4: Template particle in the raw image with red line box (left) and three square matrices chosen from the template particle with edge sizes of 30 pixels, 22 pixels and 16 pixels (right).

Considering these issues, the mean intensity of particles located in different height are checked separately in this study. The full view of the drum is divided into six zones from bottom to top and the height of each zone is 167 pixels. The mean intensity of a particle is obtained by averaging all pixels in the same area of the candidate matrix (with an edge size of 30 pixels, 22 pixels or 16 pixels). In order to reduce errors, 20 complete particles are selected manually in each height area of the FRD and used to calculate the corresponding threshold mean intensity. The mean intensities of particles in each height zone are plotted in Fig. 4.5. The mean intensity of template particles in each square matrix is illustrated by green rectangles, blue circles, and red triangles, respectively, referring to the respective size of matrix.

In each detection zone, the particle intensity value increases as the matrix size decreases.

This is because the intensity concentrically decreases with the distance from the central location, as can be seen from the Fig. 4.1. The position of the maximum intensity value is near the geometrical center of the particle. Furthermore, the particle intensity in the six zones is quite different for all the three matrix edge sizes. The intensity values in the top zone are significantly lower than that in the other height zones which is due to the shade effect of the rotating wall. In order to eliminate particles in the deeper axial layers and to retain the particles in the front layer, a regional intensity calibration is conducted for the different detection zones. The critical intensity of each detection zone is set to the minimum mean intensity for the corresponding matrix size.

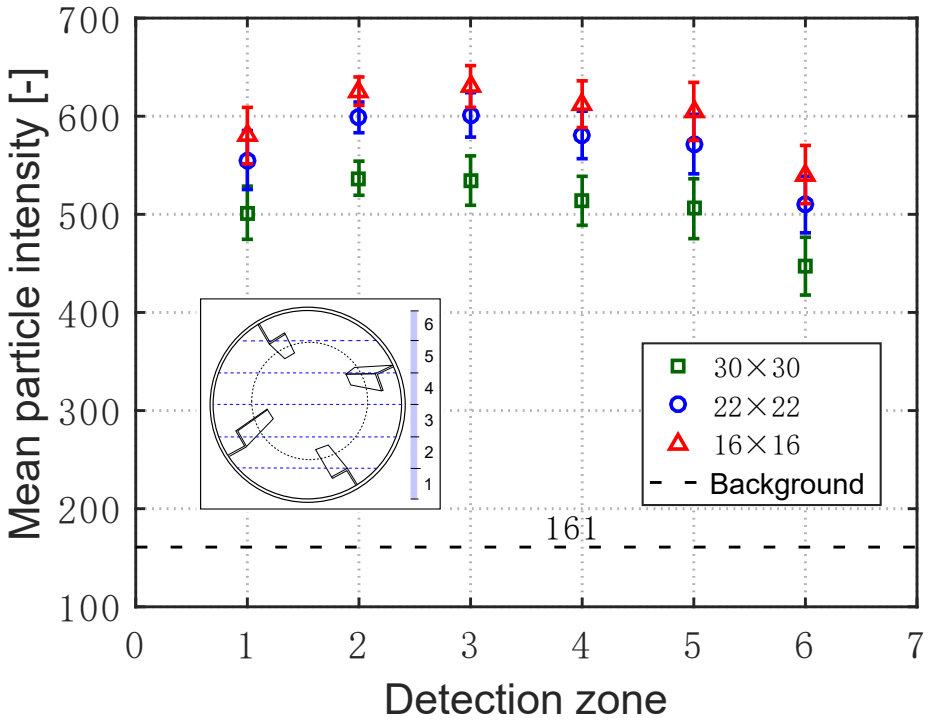

Figure 4.5: Mean intensity of a particle in different detection zones. Inserted figure: specific division of the six zones in the drum.

By applying the corresponding mean intensity value to the segregation process, the performance of the particle segmentation in the FRD is verified. Figure 4.6 shows the number of particles identified by the three candidate square matrices as a function of the threshold value used in the particle-mask correlation method, for a drum filling degree of 20 % and a rotating speed of 30 rpm. As can be seen from the graphs, the number of detected particles is higher at lower threshold values. Moreover, for a certain threshold value, more particles are detected with the small matrix of 16 pixels than with the larger matrices. This is due to the fact that particles whose edge portions overlap with other particles can still be detected by using a small matrix. When a small matrix size of 16 pixels is used, the influence of the edge portion on the calculation of the cross-correlation

coefficient matrix is automatically excluded.

At a filling degree of 20 %, the drum is theoretically filled with in total 4632 particles. Assuming that the particles are evenly distributed in the axial and transverse directions, 185 particles are located in the first axial layer at the front wall with a thickness of one particle diameter. Thus, the optimal threshold values of the cross-correlation coefficients are determined as 0.69, 0.74 and 0.78 for the candidate particle matrices with edge sizes m of 30 pixels, 22 pixels, and 16 pixels, respectively.

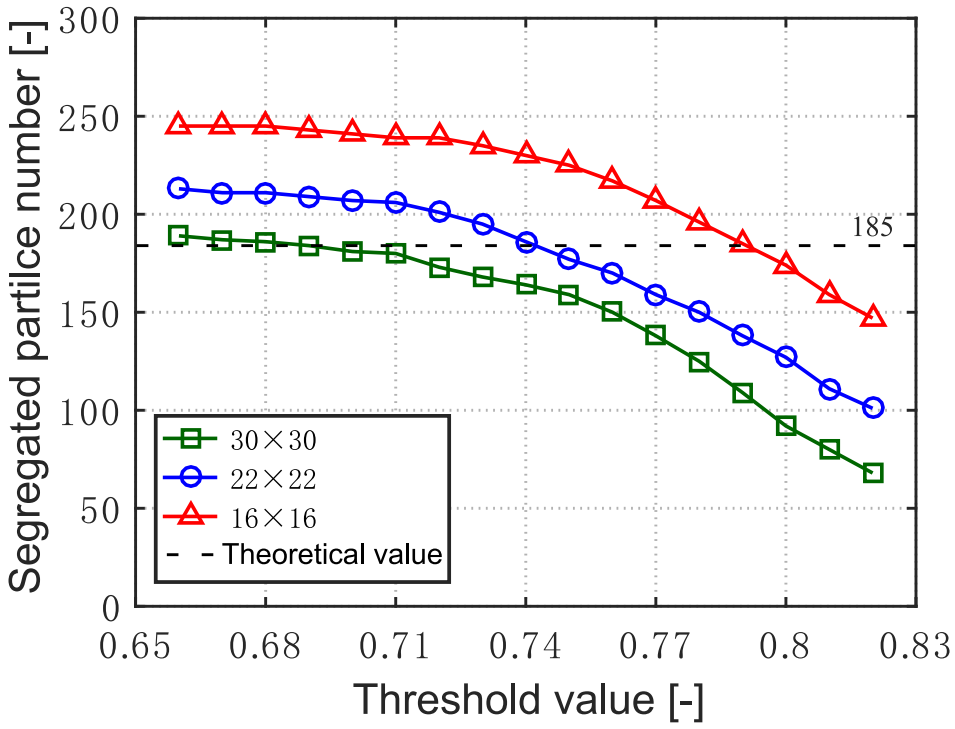

Figure 4.6: Number of particles identified by using different threshold values of the normalized cross-correlation coefficient for three candidate square matrices (30 pixels, 22 pixels and 16 pixels).

Applying these optimal threshold values in the particle segmentation, the centers of identified particles (x, y) are obtained and subsequently plotted for re-examination, as shown in Fig. 4.7.

As a result, two centers occasionally coexist in one particle image for the edge size of 16 pixels, which means that this particle is mistakenly identified as two closely-located particle images. This is due to the cross-correlation coefficient distribution having two peaks that both exceed the threshold value. With the matrix size of 22 pixels, some of the particles in the second layer which are located in the gaps of the first layer of particles or on the surface of the particle bed are also identified. Meanwhile, the matrix size of 30 pixels shows a quite good performance with no obvious misjudgments and omissions.

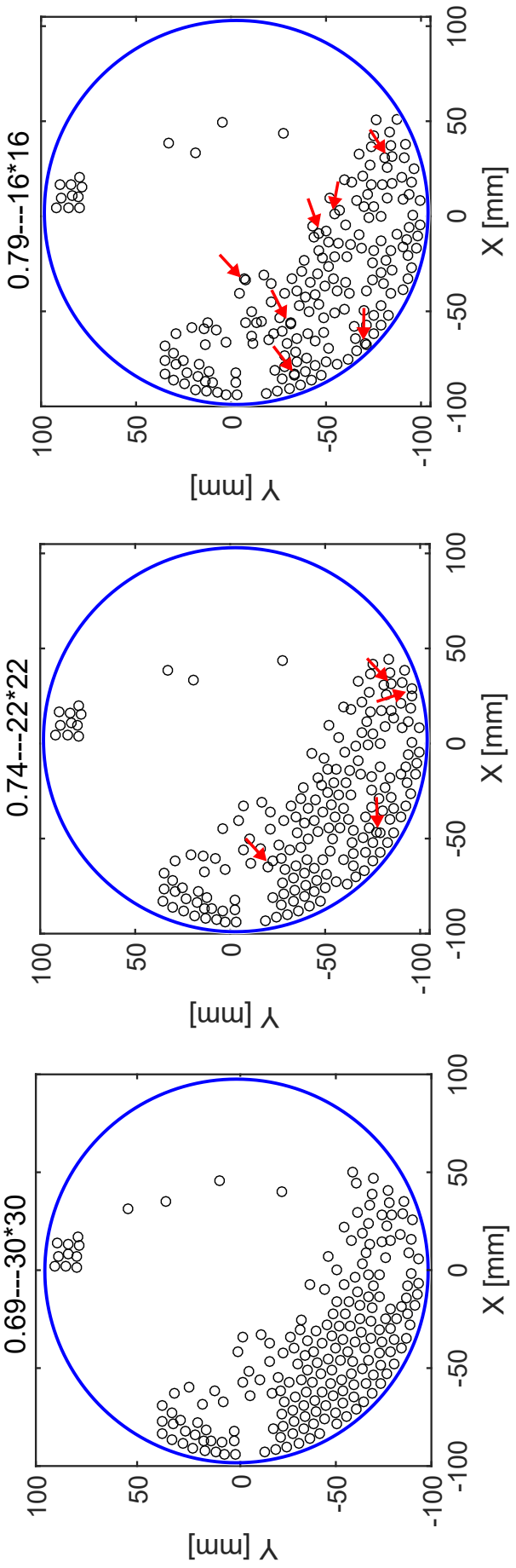

Figure 4.7: Particles identified by different edge sizes of the particle mask with the corresponding threshold values: (a) 30 pixels; (b) 22 pixels; (c) 16 pixels.

To evaluate the performance of the particle segmentation procedure, the number of particles identified per time step in the first axial layer is plotted over time, see Fig. 4.8. The total number of identified particles is illustrated for a period of 2 s, which represents a full drum rotation at 30 rpm. As the figure illustrates, the total number of detected particles is relatively stable and close to the theoretical particle number of 185 particles. Based on these results, the square matrix with an edge size of 30 pixels and a threshold value of 0.69 is selected and used in the following particle segmentation processes. The centroids of identified particles (x, y) from each image will be further used for particle tracking.

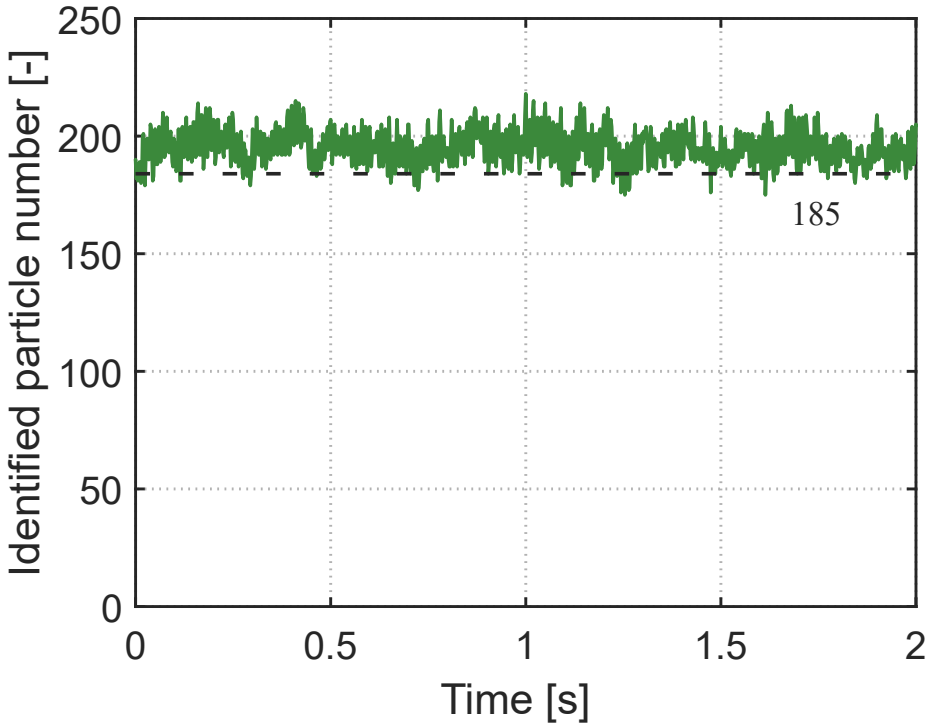

Figure 4.8: Number of particles detected in the first axial layer versus time. Matrix size 30 pixels, threshold value 0.69, filling degree 20 %, 30 rpm.

4.3.2 Verification of integrated tracking algorithm

As Jiang et al. [88] reported, the Voronoi tracking method and the relaxation probability method showed different tracking performances under different particle number density conditions. Considering the characteristics of particle motion in FRD (dilute and dense phase regions coexist), both tracking methods have initially been applied in this work for comparison purposes. Based on the tracking algorithms, the parameters required in the two tracking methods are listed in Table 4.1. In the Voronoi method, the discrepancy of Voronoi stars in two consecutive frames is considered as the measure of identification which was set as $U_{max} \cdot S_f \cdot \triangle t$ in this study. Three important radii in the probability relaxation method: *Maximum displacement radius*, *neighboring radius* and *quasi-rigidity*

radius are set at $U_{max} \cdot S_f \cdot \triangle t$, $1.5 \cdot U_{max} \cdot S_f \cdot \triangle t$ and $0.2 \cdot U_{max} \cdot S_f \cdot \triangle t$, respectively. Δt is the time interval of two images, which is 2 ms according to the frame rate of the high-speed camera in this study.

Table 4.1: Parameters used in particle tracking algorithms.

Parameter	**Value**	**Unit**
Voronoi method		
Maximum displacement filter	$U_{max} \cdot S_f \cdot \Delta t$	*pixel*
Probability relaxation method		
Maximum displacement radius R_m	$U_{max} \cdot S_f \cdot \Delta t$	*pixel*
Neighboring radius R_n	$1.5 \cdot U_{max} \cdot S_f \cdot \Delta t$	*pixel*
Quasi-rigidity radius R_q	$0.2 \cdot U_{max} \cdot S_f \cdot \Delta t$	*pixel*

Applying these two tracking algorithms, the displacement and velocity of individual particles in FRD are determined from two consecutive images. Figure 4.9 shows the velocity vector distribution of the particles over the cross-section of the FRD for 20 % filling degree and 30 rpm. Black vectors represent the particle velocities caught by both methods, while magenta and green vectors are the vectors traced only by either the Voronoi method or the probability relaxation method, respectively. Red vectors are the unreasonable vectors obtained from particle tracking. Black circles represent particles identified from the segmentation algorithm, but which are failed to pair in two consecutive frames. It is worth noting that all velocity vectors analyzed by the Voronoi method are also detected by the probability relaxation method at this time step. Therefore, there is no vector traced only by the Voronoi method.

At this time step, 192 particles are identified from the raw image. To verify the performance of the particle tracking algorithms, the recovery ratio R_r and the error ratio R_e are calculated, respectively [88]. The recovery ratio R_r is defined as the number of matched vectors divided by the number of segmented particles. The error ratio R_e is the ratio of the number of error vectors to the number of segmented particles. For the time step of 2 ms, the recovery ratios R_r for the Voronoi method and the probability relaxation method are 92.71 % and 96.35 %, respectively. The error ratios of both tracking algorithms are 1.04 %. Therefore, both tracking methods reflect good tracking performance.

For further comparison, the recovery ratios of the two tracking methods are obtained from consecutive frames over one rotation cycle, as shown in Fig. 4.10. The values of the recovery ratio are averaged from ten rotation cycles of the drum for a filling degree of 20 % and 30 rpm. As can be seen, the probability relaxation method displays a higher recovery ratio value than the Voronoi tracking method in most cases. A recovery ratio of at least 90 % is achieved by using the probability relaxation method in the whole process. It should

be noted that a relatively low recovery ratio is observed in the dilute phase region and in the surface layer of the granular bed at the bottom of the drum, where particles may move in axial direction. According to the comparison result, the probability relaxation method is selected as the only tracking method in the following study.

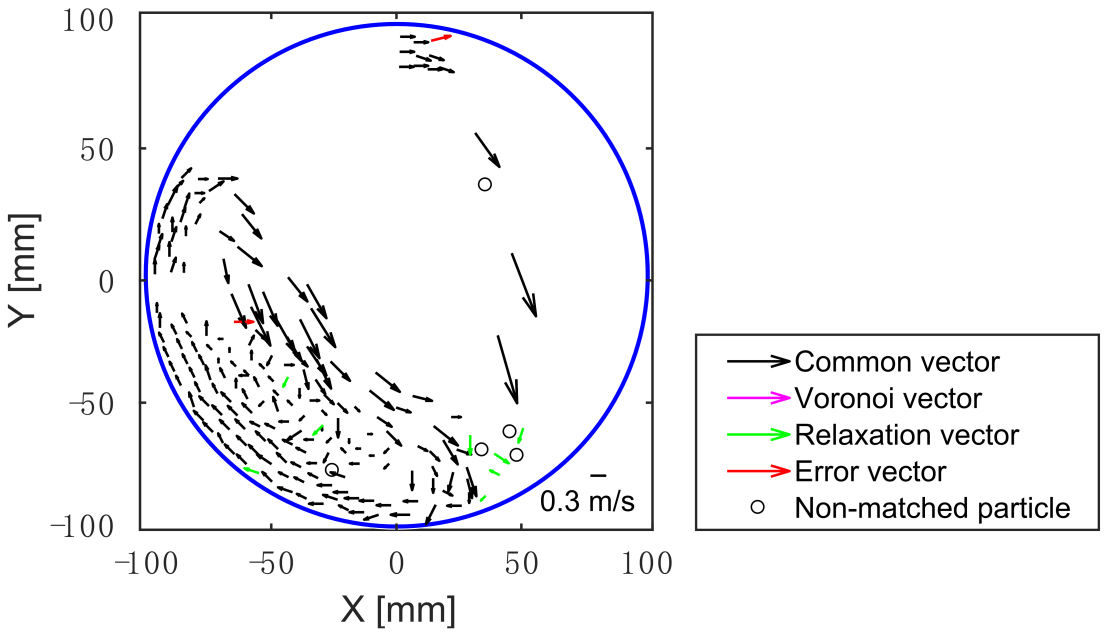

Figure 4.9: Performance of particle tracking: Comparison of velocity vector calculated for one time step, from the Voronoi method with probability relaxation methods (filling degree of 20 %, 30 rpm). Vector scale 0.3 m/s.

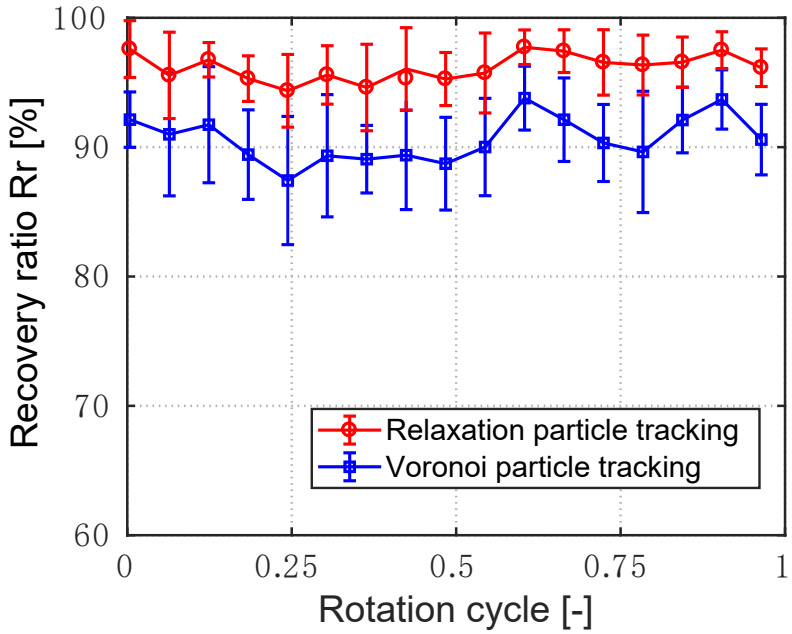

Figure 4.10: Performance of tracking algorithms: Recovery ratio R_r of Voronoi and probability relaxation methods, calculated for one rotating cycle at 20 % filling degree and 30 rpm.

Chapter 5

Experimental setup

Parts of this chapter are based on Zhang et al. [65], Zhang et al. [81] and Zhang et al. [103].

In this thesis, particle translational and rotational velocities in an FRD are measured by using a MPT system. Particle ratios of the three considered particle phases and the velocity characteristics of the granular system are investigated based on PTV measurements and DEM simulations. In addition, different numbers of flights are applied to study the particle transverse movement in the flight and in the dilute phase region. All associated experimental and simulation setups are presented in this chapter.

5.1 Flighted rotating drum

Laboratory-scale FRDs are utilized in the experiments. The diameter of the drum is 0.194 m and the length of the drum is 0.15 m, as listed in Table 5.1. Each drum is placed horizontally so that the materials have a uniform axial profile.

Table 5.1: Parameters of the flighted rotating drum.

Parameters	**Value**	**Unit**
Drum		
Diameter	0.194	m
Length	0.15	m
Flights		
Number	$1, 4, 8, 12$	$-$
Profile length	0.02	m
Angle to the wall	90	$^\circ$

The drum is made of acrylic glass and coated with fine sand (0.1 - 0.3 mm) at the inner wall to prevent particle slippage. The end walls are kept transparent and smooth to have a clear and full view. Different number of rectangular flights made of aluminum are mounted on the drum with the angle of 90°, as shown in Fig. 5.1. Each flight is composed of two segments of 0.02 m length each and the ratio of flight length to the drum size l_1/D is 0.1.

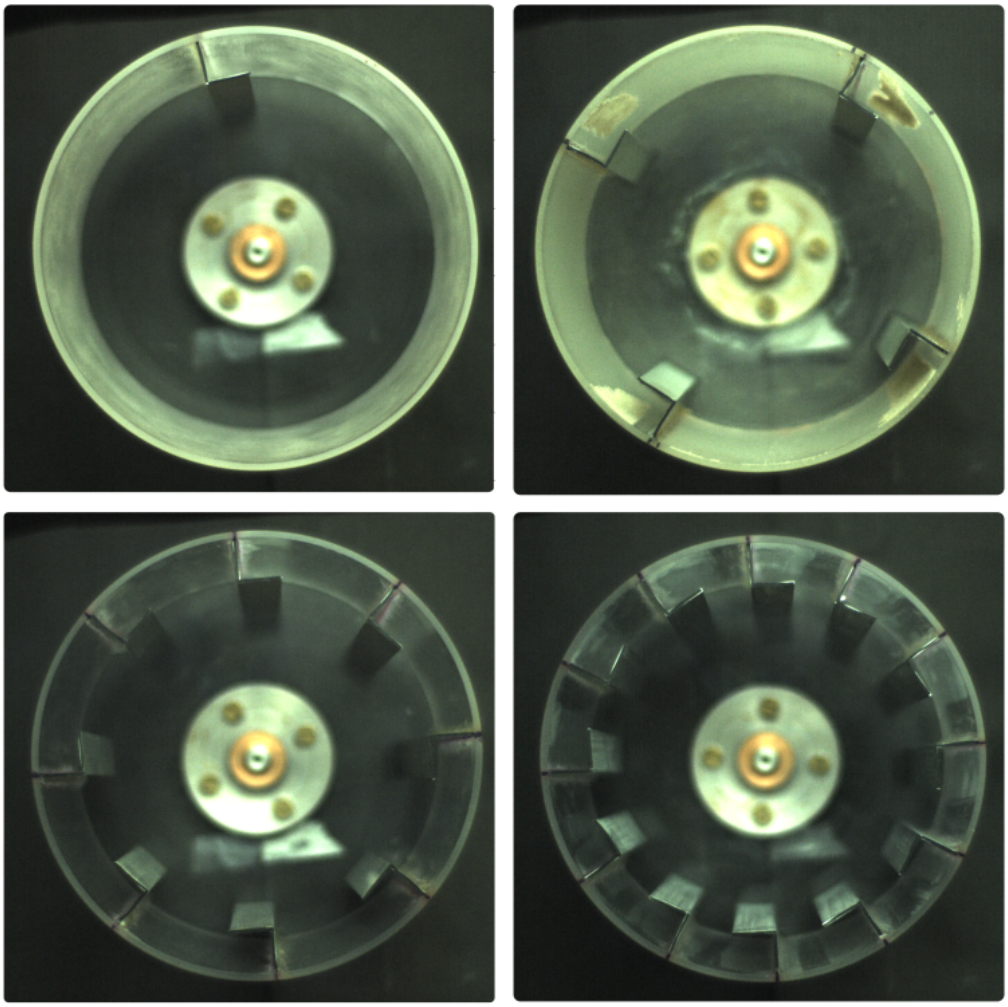

Figure 5.1: Experimental drums.

Plastic balls and soybeans are used as bed materials, as shown in Fig. 5.2. The physical properties of which are given in Table 5.2. Plastic balls have a mean diameter of 6 mm and a particle density of 1050 kg/m^3. Soybeans have a Sauter diameter of 7 mm and a particle density of 1300 kg/m^3. The dynamic angles of repose of the plastic balls and soybeans are 23.4° and 28.3°, respectively. These values are measured from images of a drum without flights which is filled with the corresponding materials to 10 % level and rotated at 10 rpm.

Figure 5.2: Bed materials used in this work: Plastic balls (left) and soybeans (right).

Table 5.2: The properties of bed materials.

Parameters	**Value**	**Unit**
Plastic balls		
Diameter	6	mm
Density	1050	kg/m^3
Bulk density	596	kg/m^3
Dynamic angle of repose	23.4 ± 0.5	$^\circ$
Soybeans		
Diameter	7	mm
Density	1300	kg/m^3
Bulk density	715	kg/m^3
Dynamic angle of repose	28.3 ± 0.4	$^\circ$

5.2 Magnetic particle tracking system

The magnetic tracking system consisted of four parts: the measuring device, data acquisition, online visualization system, as well as the magnetic tracer, as shown in Fig. 5.3. For detection, 12 anisotropic magneto resistive (AMR) sensors are installed on three acrylic glass plates. The magnetic capsule consists of a single NdFeB magnet coated with high molecular-weight polyethylene. The positions of the 12 sensors used in this study are arranged and calibrated with the help of the specialized company INNOVENT-Technologieentwicklung, Jena, Germany. The measuring range is approx. 300 mm × 400 mm × 130 mm, as listed in Table 5.3. The sensors are arranged and calibrated in order to provide an optimal measurement of the magnetic field strength. All sensors are connected to a data acquisition device, reading the data and sending it to a lab computer via USB interface.

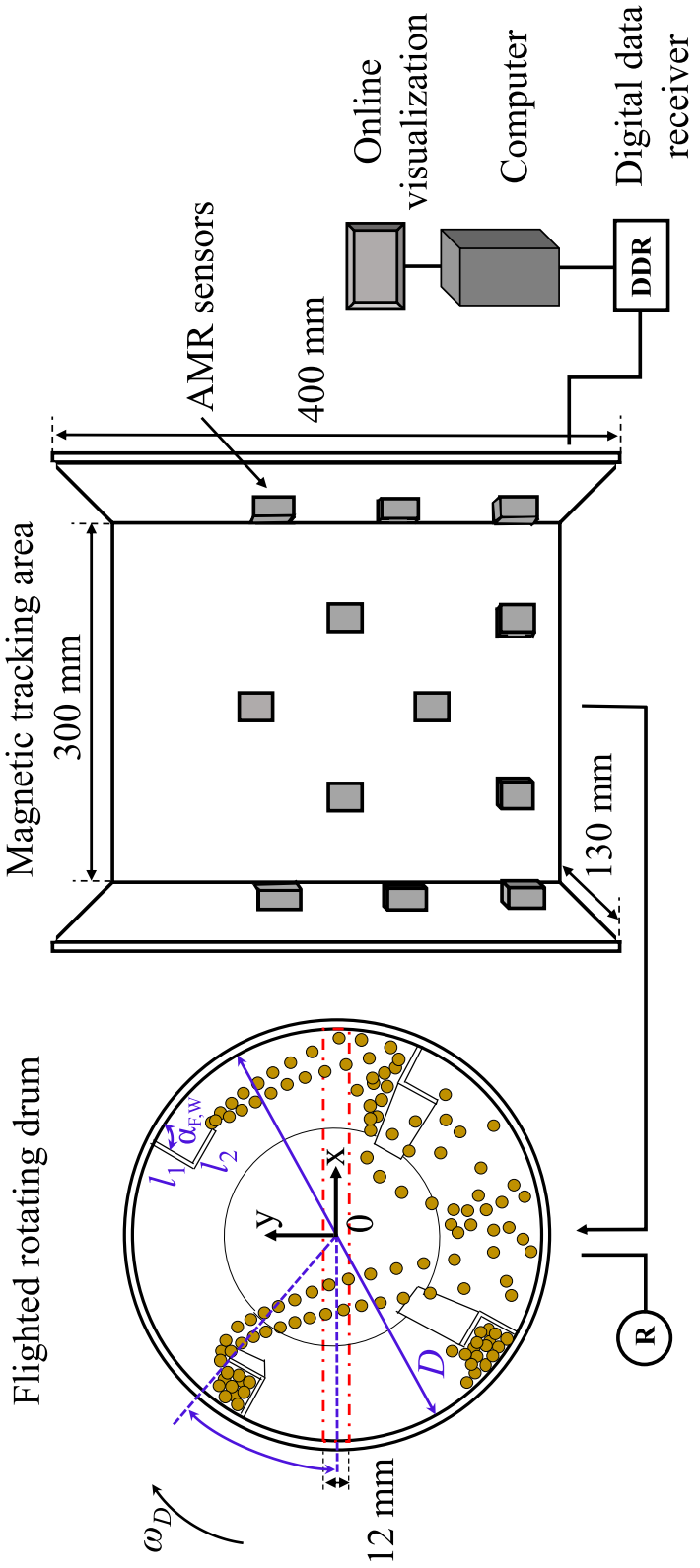

Figure 5.3: Schematic of the experimental setup: Flighted rotating drum (left) and magnetic tracking system (right).

Table 5.3: Parameters of magnetic tracking system, properties of tracer particles and operating conditions of the MPT experiments.

Parameters	**Value**	**Unit**
Monitoring volume	$300 \times 400 \times 130$	mm^3
Sensor type	AMR	–
Number of sensors	12	–
Frequency	250	Hz
Data record interval	6	ms
Tracer particle		
Magnetic cylinder size	3×5	mm
Tracer + Plastic ball density	2990	kg/m^3
Tracer + Soybean density	3590	kg/m^3
Drum operating conditions		
Flights number	4	–
Drum filling degree	5	%
Rotating speed	$10, 20, 30, 40$	rpm

Online visualization is achievable by the associated 'MagDat' software. As shown in Fig. 5.4, the white rectangles are the AMR sensors, the red and blue cylinder represents the magnetic marker. The data evaluation is performed using the 'MagCal' software installed on the computer. Before each experiment, the offset of the sensors is determined by measuring the field of an empty domain. After offset determination, a magnetic marker can be added to the domain and the change in magnetic field can be measured.

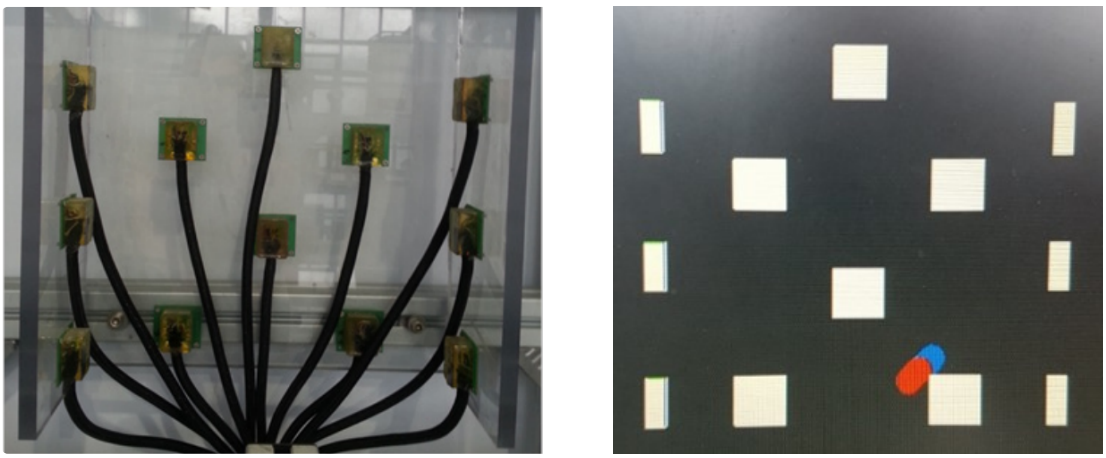

Figure 5.4: Comparison of the magnetic tracking area in the MPT system (left) and the online view on the computer (right).

Both plastic balls and soybeans are used as bed materials in the experiments with magnetic particle tracking. The tracer is a commercial cylinderical permanent magnet (NdFeB) with diameter of 3 mm and length of 5 mm, as shown in Fig. 5.5 (a). Such a

magnet is embedded in a plastic bead and a soybean, respectively, as Figs. 5.5 (b)-(c) show. The size of the tracer particles created is the same as that of the original particles, but particle density is nearly three times higher, see Table 5.3. According to the detailed analysis in Section 3.2 and the filling degree of this work of only 5 %, it can be considered that the effect of density difference on particle motion in the FRD is negligible.

Before each experiment, a certain amount of particles are filled into the drum. Then, the offset of the sensors in the 'MagDat' software is determined by measuring the field of the empty domain. After that, the tracer particle is added to the domain and the data recording starts when the movement of the particle system had reached a steady state. By using a measuring frequency of 250 Hz, the MPT system records data every 6 ms.

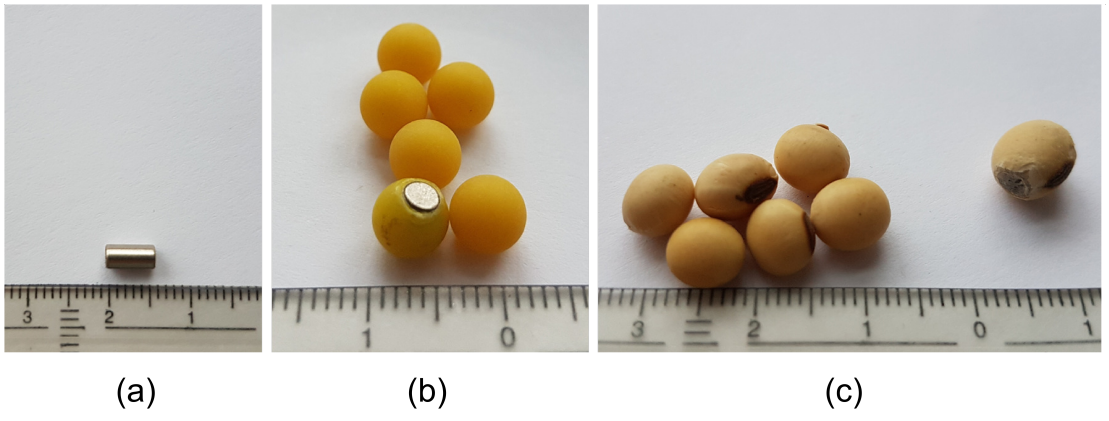

Figure 5.5: The magnet and the tracer particles created: (a) magnetic cylinder, (b) plastic balls and tracer, (c) soybeans and tracer.

The operating conditions of the drum in the magnetic tacking experiments are listed in Table 5.3. The rotating speeds of the drum is varied in four steps from 10 rpm to 40 rpm. According to the long-term practical experience, industrial rotary dryers are operated in the range of 1 - 15 rpm [104] or at a peripheral speed of the drum of 0.25 - 0.5 m/s [105]. Compared to that, the drum in this study is operated in the range of 10 rpm to 40 rpm, and the peripheral drum speed is 0.1 - 0.4 m/s.

Particle beds of 5 % filling degree are moved in the drum within four flights. This filling degree is selected since it is the optimum loading of the drum with plastic balls at 20 rpm rotating speed. It is determined for the bed material according to the method proposed by Karali et al. [2] by using the image analysis method. All the experimental measurements are performed after the drum condition was stable.

5.3 High-speed camera system

The high-speed imaging system used for the PTV experiments, including a Photron high-speed camera (LaVision, CMOS chip, 1024 × 1024 pixel), is shown in Fig. 5.6. The

camera is operated with a frame rate of 500 fps, an exposure time of $1/10,000$ s and a dynamic range of 10 bit, as listed in Table 5.4. An optical lens with 60 mm focal length is employed to obtain a suitable size of the field of view. The f-number, relative focal length to effective aperture, is set at the minimum value of 2.8, which yields a minimum depth of field and a maximum light exposure.

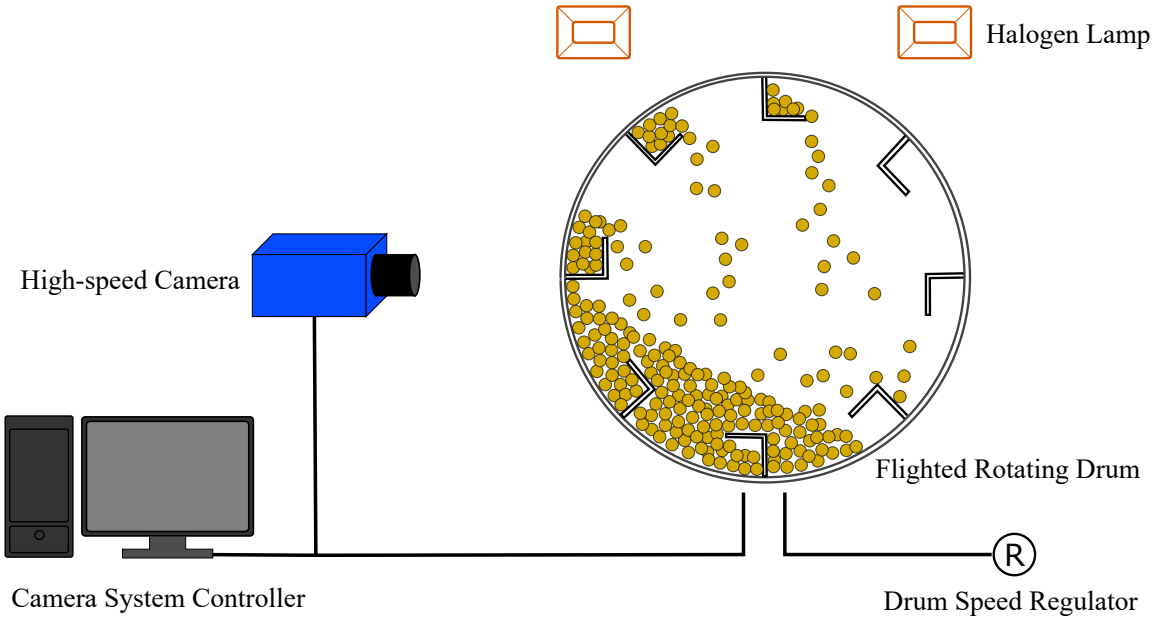

Figure 5.6: Schematic of the high-speed camera system and the experimental setup.

The system is controlled using DaVis image acquisition software (LaVision). Two continuously illuminated 400 W halogen lamps are utilized as light sources and are carefully placed to prevent overexposure caused by light reflection. The camera is positioned in front of the drum and adjusted to obtain a full view field of the drum with 200×200 mm^2. With this setting, an approximate spatial resolution scale factor S_f of 5.17 $pixels/mm$ is obtained from the standard geometry calibration process in the DaVis software.

Experiments are conducted using plastic balls with a mean diameter of $d_p = 6$ mm, as listed in Table 5.2. The drum with four flights is operated at three filling degrees of 10 %, 15 %, and 20 %, as listed in Table 5.4. With these filling degrees, the drum is overloaded and contained sufficient particles to study particle motion in the bed phase. Three drum rotating speeds of 10 rpm, 20 rpm, and 30 rpm are applied in this study by using a variable speed motor.The image recording begins after the movement of the particles in drum has been stabilized. Each experiment measures 19.2 s with a number of 9600 recorded images, which is sufficient to represent the periodicity of particle flow in the FRD.

Table 5.4: Parameters of the high-speed camera system and operating conditions of the PTV experiments.

Parameter	**Value**	**Unit**
High speed camera		
CMOS size	1024×1024	$pixel$
Frame rate	500	fps
Exposure time	$1/10\,000$	s
Dynamic range	10	bit
Focal length	60	mm
f-number	2.8	$-$
Halogen lamp	400	W
Experimental operating conditions		
Flights number	$1, 4, 8, 12$	$-$
Drum filling degree	$10, 15, 20$	%
Rotating speed	$10, 15, 20, 25, 30$	rpm

Chapter 6

DEM model of particle motion

Parts of this chapter are based on Zhang et al. [81] and Zhang et al. [103].

The Discrete Element Method (DEM) is a particle-scale numerical method for modeling the bulk behavior of granular materials. Each particle in the computational domain is tracked at every time step in a Lagrangian framework.

6.1 Governing equations

In the DEM, originally proposed by Cundall and Strack [106], the motion of the individual particle i is calculated in a Lagrangian frame by Newton's laws of motion:

$$m_{p,i}\frac{d\boldsymbol{u}_{p,i}}{dt} = \boldsymbol{f}_{pf,i} + \sum_{j=1,j\neq i}^{N_p}(\boldsymbol{f}_{c,ij}^{n} + \boldsymbol{f}_{c,ij}^{t}) + m_{p,i}g, \tag{6.1}$$

$$I_i\frac{d\boldsymbol{\omega}_i}{dt} = \sum_{j=1,j\neq i}^{N_p}(\boldsymbol{T}_{t,ij} + \boldsymbol{T}_{r,ij}), \tag{6.2}$$

where $\boldsymbol{u}_i$ and $\boldsymbol{\omega}_i$ are respectively the translational and rotational velocity of particle i; $m_{p,i}$ and $\boldsymbol{I}_i$ stand respectively for the mass and the moment of inertia; $\boldsymbol{f}_{c,ij}^{n}$ and $\boldsymbol{f}_{c,ij}^{t}$ represent the normal and tangential components of the interaction forces between particle i and particle j; $\boldsymbol{f}_{pf,i}$ is the particle-fluid interaction force on the particle i (ignored in this work, because the air force acting on the particles is negligible compared to the other forces, especially in closed drums); $\boldsymbol{T}_{t,ij}$ and $\boldsymbol{T}_{r,ij}$ represent the tangential torque and rolling torque between the interacting pair of particles i and j; N_p and $\boldsymbol{g}$ are the number of particles in interaction with particle i and the gravitational acceleration, respectively.

6.2 Contact model

In DEM simulations, two contact models can theoretically be used to deal with the interactions between particles, i.e. the hard-sphere model and the soft-sphere model.

6.2.1 Hard-sphere model

In the hard-sphere model, particles are treated as rigid and collisions occur instantaneously between two particles. Collisions that involve three or more particles are not considered in this model. Dynamics of each collision is solved by the conservation of linear and angular momentum, which means that the velocity after collision is a function of the velocity before collision. This model tracks particles by handling each collision in sequence - one collision at a time. Particle trajectories can be obtained by a simple repetition of finding the next collision pair, advancing all particles to the time of collision of this pair, handing the collision dynamics of the pair, and moving on to detect the next collision. For dilute systems, this algorithm is very efficient since no numerical integration of motion equations is performed. However, the adaptability of the hard-sphere model to dense systems is poor due to the high possibility of enduring contacts and multi-particle collisions [107].

6.2.2 Soft-sphere model

In the soft-sphere model, particles are typically assumed to remain geometrically rigid during contact. But a slight overlap (or overlap volume) δ_{ij} is allowed during the collision period to represent the deformation at particle contacting surface [106], as shown in Fig. 6.1. For two particles in the positions $\boldsymbol{r_i}$ and $\boldsymbol{r_j}$ with the corresponding linear and angular velocities, the relative velocity of the contact point is

$$\boldsymbol{u}_r = (\boldsymbol{u}_i - \boldsymbol{u}_j) + (\boldsymbol{r}_i\boldsymbol{\omega}_i - \boldsymbol{r}_j\boldsymbol{\omega}_j). \tag{6.3}$$

The normal component $\boldsymbol{u}_r^n$ and tangential component $\boldsymbol{u}_r^t$ of relative contact velocity are calculated as

$$\boldsymbol{u}_r^n = (\boldsymbol{u}_r \cdot \boldsymbol{n}^n)\boldsymbol{n}^n, \tag{6.4}$$

$$\boldsymbol{u}_r^t = \boldsymbol{u}_r - \boldsymbol{u}_r^n. \tag{6.5}$$

Here, $\boldsymbol{n}^n = (\boldsymbol{r}_i - \boldsymbol{r}_j)/|\boldsymbol{r}_i - \boldsymbol{r}_j|$ is the normal unit vector along the contact line pointing from particle i to particle j. Besides, the unit vecor in tangential direction is $\boldsymbol{n}^t = \boldsymbol{u}_r^t/|\boldsymbol{u}_r^t|$.

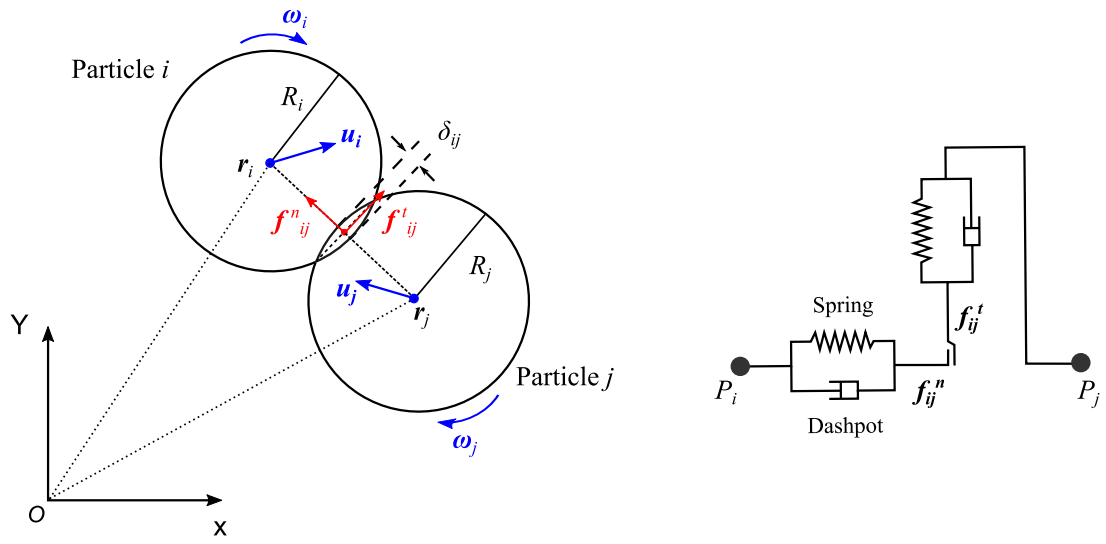

Figure 6.1: The soft-sphere contact model used in DEM: (a) contact of two particles with notation; (b) simple spring-dashpot model.

In the soft-sphere model, two spherical particles are in mechanical contact if $(R_i + R_j - |\boldsymbol{r}_i - \boldsymbol{r}_j|) > 0$. When the sum of radii of the two particles exceeds the distance of the two centers of particles, the overlap can be expressed as

$$\delta_{ij} = max[0, (R_i + R_j - |\boldsymbol{r}_i - \boldsymbol{r}_j|)]. \tag{6.6}$$

The normal and tangential components of contact force can be written in the form of

$$\boldsymbol{f}^n_{c,ij} = f^n_{c,ij} \cdot \boldsymbol{n}^n, \tag{6.7}$$

$$\boldsymbol{f}^t_{c,ij} = f^t_{c,ij} \cdot \boldsymbol{n}^t; \tag{6.8}$$

The normal force $\boldsymbol{f}^n_{c,ij}$ changes the translational motion of particles, where the tangential force $\boldsymbol{f}^t_{c,ij}$ changes the rotational motion of particles. Both components of the contact force are related to the relative position of particles $(\boldsymbol{r}_i - \boldsymbol{r}_j)$ and the relative velocity of particles $\boldsymbol{u}_r$.

The total torque acting on particle i is calculated by

$$\boldsymbol{T}_{t,i} = \boldsymbol{r}_i \times \boldsymbol{f}_{t,ij}. \tag{6.9}$$

In the soft-sphere model, the normal and tangential components of the contact force are decomposed into a conservative spring force and a dissipative dashpot force. They are

expressed by

$$\boldsymbol{f}_{ij}^{n} = \boldsymbol{f}_{con,ij}^{n} + \boldsymbol{f}_{dis,ij}^{n}. \tag{6.10}$$

$$\boldsymbol{f}_{ij}^{t} = \boldsymbol{f}_{con,ij}^{t} + \boldsymbol{f}_{dis,ij}^{t}. \tag{6.11}$$

For the case of Coulomb friction between the particles, if the condition

$$|\boldsymbol{f}_{ij}^{t}| > \mu |\boldsymbol{f}_{ij}^{n}| \tag{6.12}$$

is satisfied during any contact time, then sliding occurs and the tangential contact force is calculated as

$$\boldsymbol{f}_{ij}^{t} = -\mu |\boldsymbol{f}_{ij}^{n}| \boldsymbol{t}_{ij}, \tag{6.13}$$

where μ is the friction coefficient and $\boldsymbol{t}_{ij} = \boldsymbol{u}_{t,ij}/|\boldsymbol{u}_{t,ij}|$ is the tangential unit vector.

Linear spring-dashpot model

Considering Hooke's law, the normal and tangential spring forces in this model, $\boldsymbol{f}_{con,ij}^{n}$ and $\boldsymbol{f}_{con,ij}^{t}$, are calculated by

$$\boldsymbol{f}_{con,ij}^{n} = -k_n \delta_{ij,n} \boldsymbol{n}^{n}, \tag{6.14}$$

$$\boldsymbol{f}_{con,ij}^{t} = -k_t \delta_{ij,t} \boldsymbol{n}^{t}. \tag{6.15}$$

Where, k_n is the normal stiffness spring coefficient (or elastic coefficient) and k_t is the tangential stiffness spring coefficient; $\delta_{ij,n}$ and $\delta_{ij,t}$ are the normal overlap and the vector of tangential displacement between particles i and j, respectively.

The normal and tangential dashpot forces ($\boldsymbol{f}_{dis,ij}^{n}$ and $\boldsymbol{f}_{dis,ij}^{t}$) are determined based on the normal and tangential components of relative contact velocity:

$$\boldsymbol{f}_{dis,ij}^{n} = -\eta_n \boldsymbol{u}_{ij}^{n}, \tag{6.16}$$

$$\boldsymbol{f}_{dis,ij}^{t} = -\eta_t \boldsymbol{u}_{ij}^{t}, \tag{6.17}$$

where η_n and η_t are normal and tangential damping coefficients, respectively.

This linear model is applicable for particles that collide at low relative impact velocities. There is no plastic deformation at the contact, so that all of the kinetic energy is recovered when the particles separate.

Hertzian spring-dashpot model

The Hertzian spring-dashpot model is a non-linear model developed to describe the inelastic collision of particles. Integration of Hooke's law over the deformation area is conducted and results in a non-linear relationship. In this model, the normal and tangential spring forces are calculated by

$$\boldsymbol{f}_{con,ij}^{n} = -k_{Hz}^{n}\delta_{ij,n}^{\frac{3}{2}}\boldsymbol{n}_{ij}, \tag{6.18}$$

$$\boldsymbol{f}_{con,ij}^{t} = -k_{Hz}^{t}\delta_{ij,t}^{\frac{3}{2}}. \tag{6.19}$$

The tangential deformation of the particle surfaces $\delta_{ij,t}$ since the time when the two particles came into contact, $t_{c,0}$, can be calculated by

$$\delta_{ij,t} = \int_{t_{c,0}}^{t} u_{r,t}dt. \tag{6.20}$$

The normal and tangential dashpot forces are calculated from

$$\boldsymbol{f}_{dis,ij}^{n} = -\eta_{Hz}^{n}\delta_{ij,n}^{\frac{1}{4}}\boldsymbol{u}_{ij}^{n}, \tag{6.21}$$

$$\boldsymbol{f}_{dis,ij}^{t} = -\eta_{Hz}^{t}\delta_{ij,t}^{\frac{1}{4}}\boldsymbol{u}_{ij}^{t}. \tag{6.22}$$

The expressions for relevant particle pair variables are listed in Table 6.1.

6.3 Rolling model

According to the work of Ai et al. [108], rolling friction torque $\boldsymbol{T}_{r,ij}$ can be modelled by

$$\boldsymbol{T}_{r,ij} = -k_r k_n \delta_{ij} R^* \frac{\boldsymbol{\omega}_r}{|\boldsymbol{\omega}_r|}. \tag{6.23}$$

Here k_r is the coefficient of rolling friction, k_n is the normal stiffness coefficient, and the relative angular velocity is defined as

$$\boldsymbol{\omega}_r = \frac{R_i\boldsymbol{\omega}_i + R_j\boldsymbol{\omega}_j}{R_i + R_j}. \tag{6.24}$$

Table 6.1: Model coefficients used in the Hertzian spring-dashpot model.

Parameter	**Equation**
Model coefficients	
Normal stiffness coefficient	$k^n_{Hz} = \frac{4}{3}E^*\sqrt{R^*}$
Normal damping coefficient	$\eta^n(e)_{Hz} = \alpha(e)_{Hz}\sqrt{m^*_p k_{Hz}}$
Tangential stiffness coefficient	$k^t_{Hz} = 8G^*\sqrt{R^*}$
Tangential damping coefficient	$\eta^t(e)_{Hz} = \sqrt{\frac{2}{3}}\alpha(e)_{Hz}\sqrt{m^*_p k_{Hz}}$
Damping ratio	$\alpha(e)_{Hz} = -\sqrt{5}\,ln\,e/\sqrt{(ln\,e)^2+\pi^2}, e>0$
	$= -\sqrt{5}, \quad e = 0$
Equivalent properties	
Young's modulus	$\frac{1}{E^*} = \frac{1-\sigma_i^2}{E_i} + \frac{1-\sigma_j^2}{E_j}$
Radius	$\frac{1}{R^*} = \frac{1}{R_i} + \frac{1}{R_j}$
Shear modulus	$\frac{1}{G^*} = \frac{2(1-\sigma_i)(1+\sigma_i)}{E_i} + \frac{2(1-\sigma_j)(1+\sigma_j)}{E_j}$
Mass	$\frac{1}{m^*_p} = \frac{1}{m_{p,i}} + \frac{1}{m_{p,j}}$

6.4 DEM simulation setup

DEM simulations are conducted by applying open source software LIGGGHTS and are implemented by using the same configuration and operation conditions of the FRD as in reality, as well as the same particle properties. The physical properties and simulation parameters are summarized in Table 6.2. Particle interactions are calculated by the Hertzian contact model with tangential history tracking (Section 6.2).

In the soft-sphere contact model, the effects of spring and dashpot appear through stiffness k and damping coefficient η, which are determined by the physical material properties of Poisson ratio σ, Young's modulus E and the coefficient of restitution e. Young's modulus E of 10^7 Pa is used which is smaller than the typical Young's modulus of 10^9 Pa of polystyrene [109]. With confirmed negligible difference, particles are commonly assumed to be less stiff than in reality to avoid the requirement of excessively small time step in DEM simulation. The Poisson's ratio σ of 0.32 is taken from [110]. For stiff spheres such as the plastic balls in this study, the rolling resistance for both particle-particle and particle-wall is extremely weak. Thus, the rolling friction coefficient k_r is set as 0.1 for both particle-particle and particle-wall interactions [111].

Table 6.2: Physical properties and parameters used in DEM simulation.

Parameter	**Value**	**Unit**
Particle properties		
Young's modulus E	10^7	Pa
Poisson ratio σ	0.32	–
Coefficient of restitution e_{pp}	0.75	–
Coefficient of restitution e_{pw}	0.68	–
Coefficient of restitution e_{pf}	0.85	–
Friction coefficient μ_{pp}	0.6	–
Friction coefficient μ_{pw}	0.5	–
Friction coefficient μ_{pf}	0.06	–
Rolling coefficient k_r	0.1	–
Simulation parameters		
Time step Δt_{DEM}	10^{-5}	s
Simulation time t_{sim}	30	s

6.4.1 Restitution coefficient

The restitution coefficient, which is the ratio of particle velocities after and before a collision, is an essential parameter characterizing the impact behavior of particles. Here, the restitution coefficient is measured from collision events that are generated by a vibratory feeder and captured by a high-speed imaging system [112]. The restitution coefficients of 0.75, 0.68 and 0.85 are evaluated from the experimental measurements for particle-particle, particle-wall, and particle-flight interactions, respectively.

6.4.2 Friction coefficient

The coefficient of friction is obtained by combing experiments and simulations: Several numerical simulations with changing parameters are conducted to approach the actual value obtained in the experiment, similarly as in [113]. For a rotary drum without internal flights operated under rolling motion, the angle between the free surface of the material and the horizontal is called the dynamic angle of repose. This angle depends on the drum rotating speed, wall roughness, and the particle properties. In this work, the dynamic angle of repose in a non-flighted rotating drum, with 20 % filling degree at 30 rpm rotating speed, is measured to calibrate the friction coefficients of particle-particle and particle-wall interactions, as shown in Fig. 6.2. Each experiment or simulation is repeated three times, and the CV value is calculated from the repeated data.

Values between 0.4 and 0.7 are evaluated for both, the particle-particle and the particle-wall friction coefficients, as listed in Table 6.3. As the simulations revealed, slumping motion of the granular bed in the cross-section sometimes occurred. In this case, the surface of the bed is distorted so that two different angles of repose are generated at the upper and lower part of the particle bed. This phenomenon has deviated from the real

particle movement observed in the experiment under the same conditions, thus the result was marked as '-' in Table 6.3. The dynamic angle of repose Θ_D determined experimentally under the same operating conditions is 26.99°. In the simulations, the smallest deviation is obtained with the parameters $\mu_{pw} = 0.5$, $\mu_{pp} = 0.6$. Therefore, these two values are selected and used for the subsequent simulations.

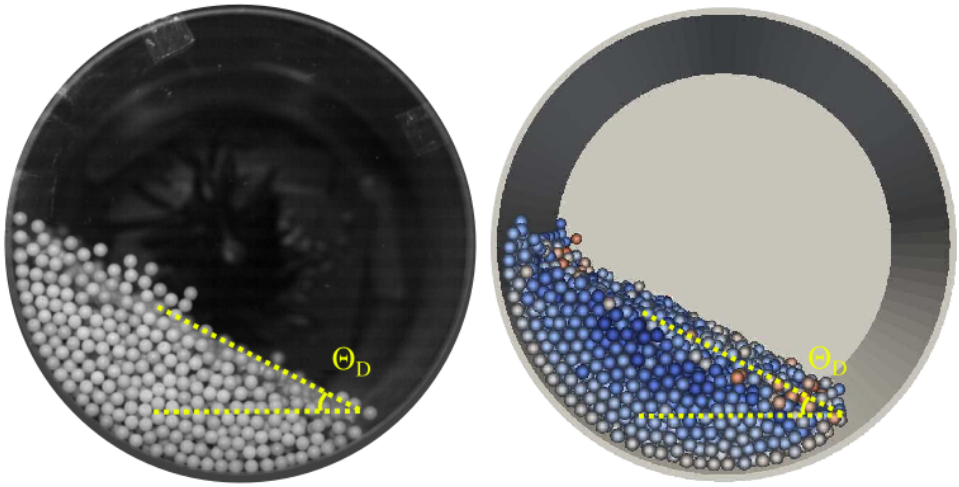

Figure 6.2: Dynamic angle of repose of plastic balls: Comparison between experimental and simulated images to determine the coefficients of friction (drum without flights, 20 % filling degree, 30 rpm rotating speed).

Table 6.3: Numerical analysis of the dynamics angle of repose as a function of the particle-wall and particle-particle friction coefficient. Filling degree 20 %, 30 rpm.

$Nr.$	μ_{pw}	μ_{pp}	Θ_D (°)	CV(%)
1	0.4	0.4	-	-
2	0.4	0.5	27.99	3.11
3	0.4	0.6	29.56	1.83
4	0.4	0.7	32.45	2.25
5	0.5	0.4	-	-
6	0.5	0.5	-	-
7	0.5	0.6	26.69	1.21
8	0.5	0.7	28.21	3.05
9	0.6	0.4	-	-
10	0.6	0.5	-	-
11	0.6	0.6	28.20	1.88
12	0.6	0.7	29.45	2.78
13	0.7	0.4	-	-
14	0.7	0.5	-	-
15	0.7	0.6	26.55	3.97
16	0.7	0.7	28.63	0.99
Exp			26.99	0.85

In an FRD, the free surface of particles in a flight also displays a kinetic angle of repose with the horizontal. This angle is affected by the drum rotating speed, particle properties, flight roughness, but also by the flight's angle position. When the particles are about to completely discharge from the flight, the angular position of the flight tip is defined as the final discharge angle. At this discharging point, a very small number of particles roll or slide over the flight surface. These particles are only subjected to friction between the particles and the flight, as well as to collisional stress between the particles. The investigation of particle-flight friction coefficient is performed in the FRD of the present work with 10 % filling degree and rotating speed of 30 rpm. The kinetic angle of particles γ when the flight moved to the 12 o'clock position, and the final discharge angle δ_L are predicted and compared with the experimental results, as depicted in Fig. 6.3.

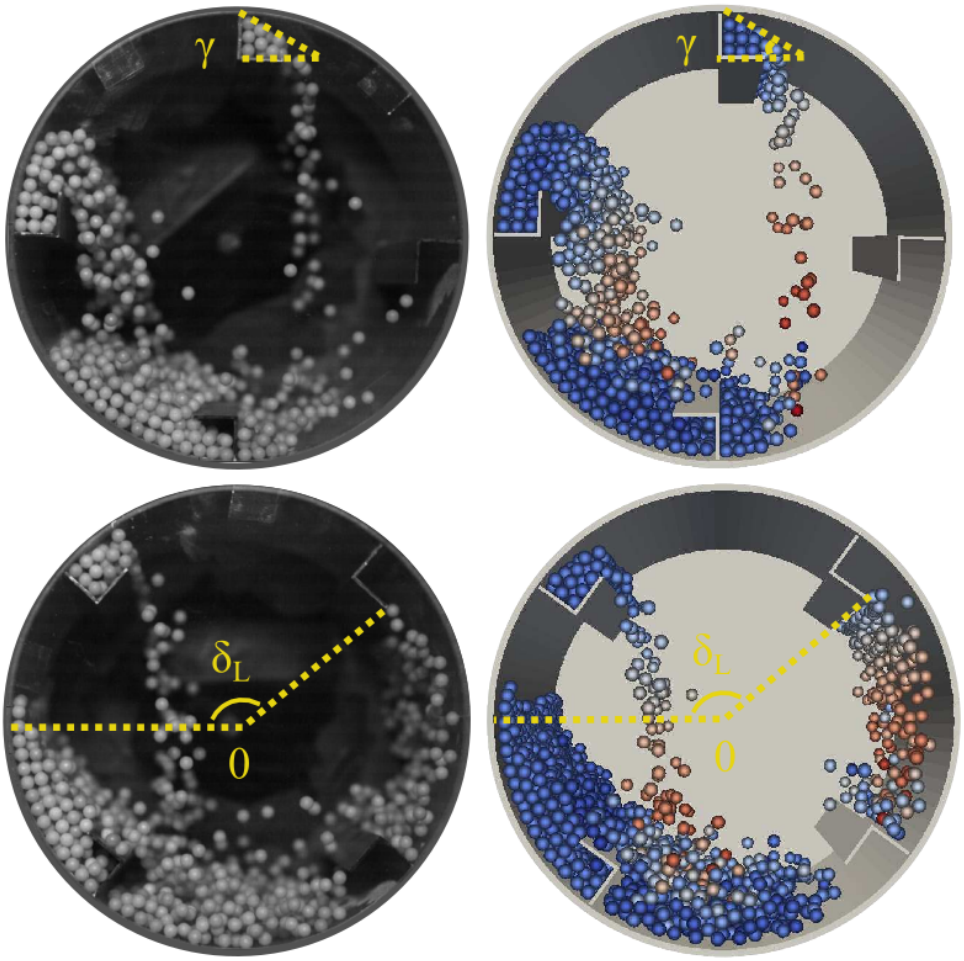

Figure 6.3: Kinetic angle of repose of plastic balls in the flight: Comparison between experimental and simulated images to determine the coefficient of particle-flight friction (10 % filling degree, 30 rpm rotating speed).

The simulated and experimental kinetic angles of repose for flight particles are shown in Table 6.4, which are obtained under various particle-flight friction coefficients. Each

experiment or simulation is repeated three times, and the CV value is calculated from the repeated data. As can be seen, the predicted results from $\mu_{pf} = 0.06$ agree well with the experimental data for both γ and δ_L, with values of 30.25° and 140.34°. The particle-flight friction coefficient 0.06 is hence selected for DEM simulations.

Table 6.4: Numerical analysis of the kinetic angle of repose as a function of particle-flight friction coefficient. Filling degree 10 %, 30 rpm.

Nr.	μ_{pf}	γ (°)	CV_γ (%)	δ_L (°)	CV_{δ_L} (%)
1	0.03	15.10	3.31	138.91	1.04
2	0.04	19.10	8.90	138.95	0.50
3	0.05	27.75	4.14	139.10	1.40
4	0.06	30.25	4.13	140.34	2.69
5	0.07	25.65	0.19	141.40	2.95
6	0.08	23.55	5.31	141.73	2.83
Exp	-	30.15	1.50	140.20	2.13

6.4.3 Time step selection

The collision time τ_H is estimated based on Hertz contact theory [114] to

$$\tau_H = 2.87 \left(\frac{(m^*)^2}{R^*(E^*)^2 u_{c,max}} \right)^{0.2} \tag{6.25}$$

Assuming a maximum collision velocity $u_{c,max}$ of 2 m/s in the drum system, the estimated collision time τ_H for two particles with diameter of 6 mm is approximately 2.99×10^{-4} s. Hence, the DEM time step is selected as $10^{-5}s$, less than $\tau_H/20$, to ensure an accurate performance of the contact model.

6.4.4 Simulation procedure and exemplary results

Using the previously discussed calibrated parameters, various DEM simulations have been conducted. In each of them, a homogeneous packed bed is first initiated by random generation and free fall in the domain before starting the simulation. Then, the drum is rotated with the selected speed for 30 s. However, only the last 20 s of this period are exploited for further analysis, by extracting data in intervals of 0.002 s. Figure 6.4 shows an example of DEM results in visual comparison with experimental data. The calculation time for one case is 2 - 4 h on one PC (CPU: 4.0 GHz).

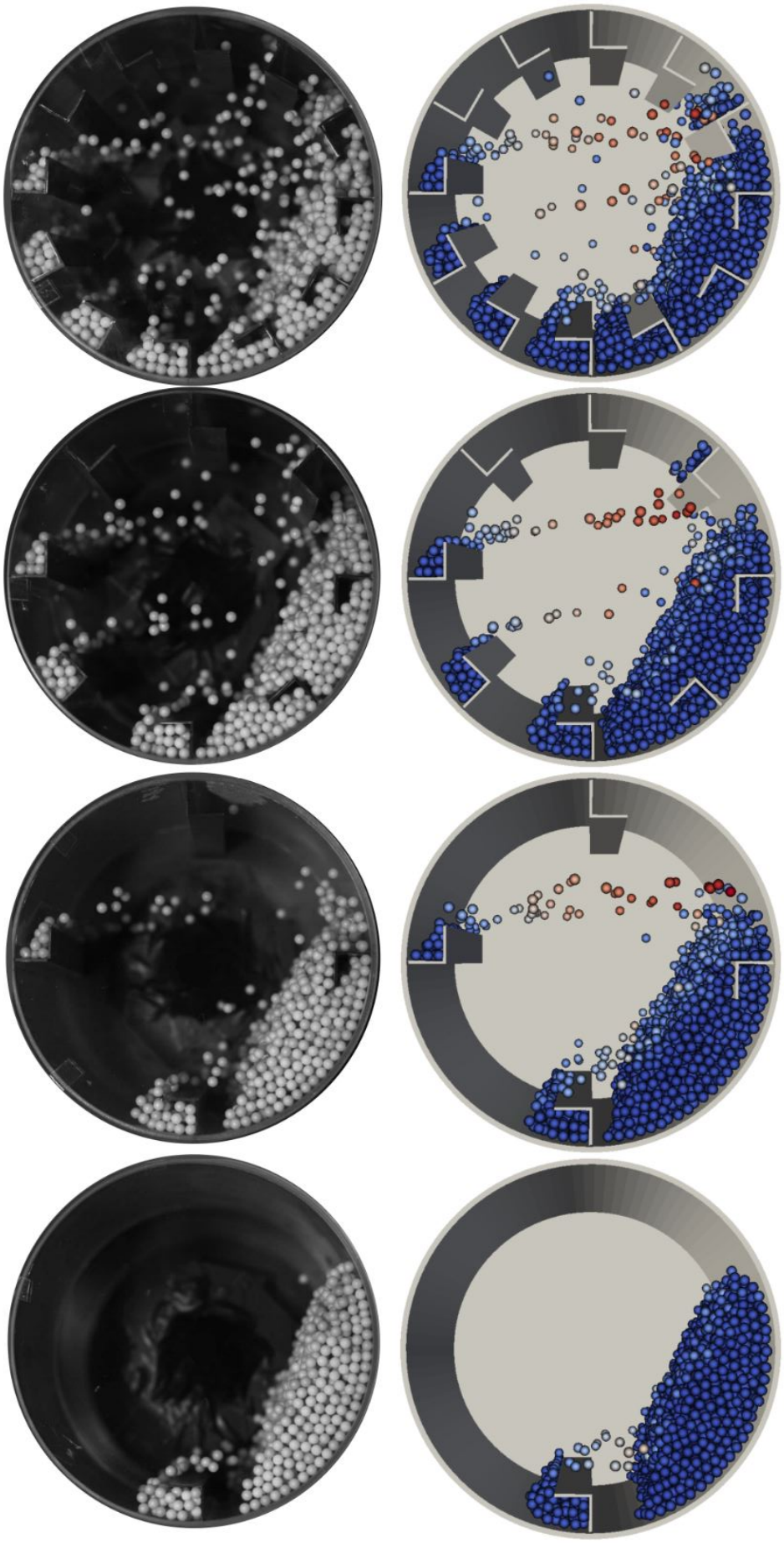

Figure 6.4: Image comparisons between DEM simulations and PTV measurements. The drum was filled to 15 % and rotated at 10 rpm; it had one, four, eight, or twelve rectangular flights.

Chapter 7

MPT measurements of particle velocity characteristics

This chapter is based on Zhang et al. [65].

7.1 Particle dynamics in MPT system

Due to the close relationship between particle motion and drum performance, it is necessary to better understand the particle dynamics in FRD. With the MPT method, the position, translational velocity, and rotational speed of the tracer particle can be studied at each time step. Due to the ability to track particles in dense granular flows, the MPT technique has been successfully used to study particle movement, mixing and segregation in prismatic spouted beds and fluidized beds [18, 66, 67, 69].

Here, the MPT technique is applied for continuous 3D tracking of particles in a horizontally arranged laboratory-scale FRD for the first time. A rotating drum with four flights is filled to 5 % and rotated at four speeds of 10, 20, 30 and 40 rpm (Table 5.3). The experiments are conducted with plastic balls and soybeans. Experimental setup and operating process have been described in Chapters 3 and 5.

The effect of drum rotating speed on particle motion in the FRD is investigated. The time-averaged translational and rotational velocity distributions are evaluated in dependence on the type of bed material and drum rotating speed. Furthermore, the falling time of particles in the dilute phase is determined as a function of discharge angle. In addition, translational velocities are measured in the dilute phase in the equatorial region of the drum.

7.1.1 Particle translational velocity

With the Cartesian coordinate values x, y and z at time step t_i, the particle translation velocity components V_k (k represents the Cartesian coordinate x, y or z) are computed by

$$V_k(t_i) = \lim_{t_{i+1} \to t_i} \frac{r_k(t_{i+1}) - r_k(t_i)}{t_{i+1} - t_i} = \frac{dr_k}{dt}. \tag{7.1}$$

With the velocity components, the particle total velocity V at time step t_i is determined as

$$V = \sqrt{V_x(t)^2 + V_y(t)^2 + V_z(t)^2}. \tag{7.2}$$

7.1.2 Particle rotational velocity

By using the MPT method, the particle rotation characteristics are detected at each time step and described with the alignment values $E_x^{'}$, $E_y^{'}$ and $E_z^{'}$. Thereafter, the angular velocity of particle ω at the time t_i is computed by

$$\omega = |\frac{\phi_{i+1} - \phi_i}{t_{i+1} - t_i}|. \tag{7.3}$$

In this equation, the angle of rotation ϕ is obtained from

$$\sin(\frac{\phi}{2}) = \frac{1}{|r|} \cdot \frac{S_{rot}}{2}. \tag{7.4}$$

The rotation path S_{rot} is calculated by

$$S_{rot} = \sqrt{(E_{x2}^{'} - E_{x1}^{'})^2 + (E_{y2}^{'} - E_{y1}^{'})^2 + (E_{z2}^{'} - E_{z1}^{'})^2}. \tag{7.5}$$

7.1.3 Particle velocity vector

To visualize the velocity vector distribution inside the FRD, the drum is separated into $72 \times 32 \times 15$ cells in circumferential, radial and axial direction, respectively, as shown in Fig. 7.1. All data received from measurement and calculation can be distributed into these small cells according to their coordinate value. Then, average values could be calculated for every cell to represent its physical properties.

7.1.4 Falling time of the dilute phase

The free fall motion in a single curtain is recorded by consecutive points from the MPT system with the constant recording interval of 6 ms. By counting the number of these points from particle leaving a flight tip to the first collision with the dense phase, the rotating wall or a flight, the falling time of the dilute phase could be computed. All the curtains received from the MPT measurement are checked. The data of the falling time

obtained is distributed over the range of discharge angle δ from -10° to 140°. Then average values of the falling time are calculated for every 10°.

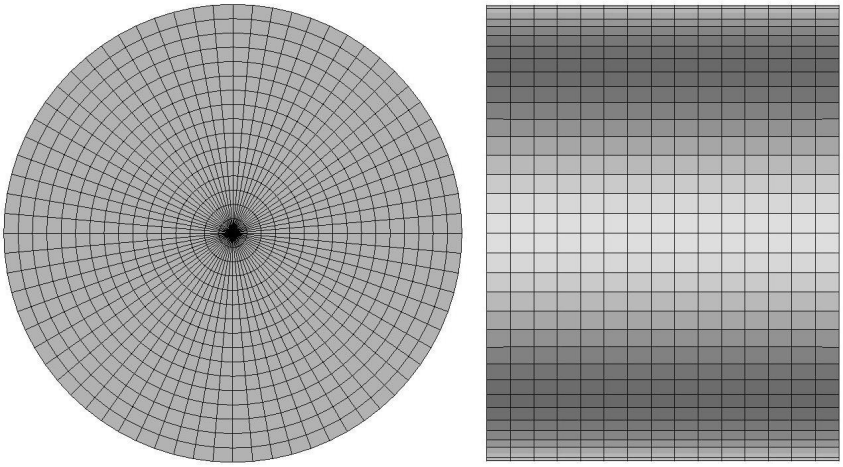

Figure 7.1: Front view (left) and side view (right) of the polyhedral mesh adopted to map the particle velocity from MPT test.

7.1.5 Dilute phase velocity

To characterize the movement of particles in the dilute phase, a planar slice is spanned over the equatorial drum cross-section, as depicted by red dotted lines in Fig. 5.3. In the horizontal plane, this slice is divided into 16 segments of $\Delta X = 12.1$ mm in width and a height of $\Delta Y = 12$ mm (ranged from -6 mm to +6 mm). Based on the coordinate values X and Y, the data located in this region can be clearly selected in advance. For each segment, average values are calculated of the particle velocities. All the data analyses are performed using the 'Matlab' software.

7.2 Results and discussion

7.2.1 Spatial and temporal particle distributions

To characterize the particle motion, occupancy plots are generated from the measurements for the example of 10 rpm drum rotating speed with plastic balls of 5 % filling degree, as shown in Fig. 7.2. These parameters are chosen to verify the influence of measurement duration time and data repeatability.

In Fig. 7.2 (a), the red line denotes the wall of the drum and the small blue circles depict the tracer position measured each 6 ms for 6 min of experimental time. Figures 7.2 (a)-(b) show the front and side view, respectively. These figures give an example of the tracer movement inside the drum, containing information on the particle positions in the two phases defined (dilute phase and dense phase).

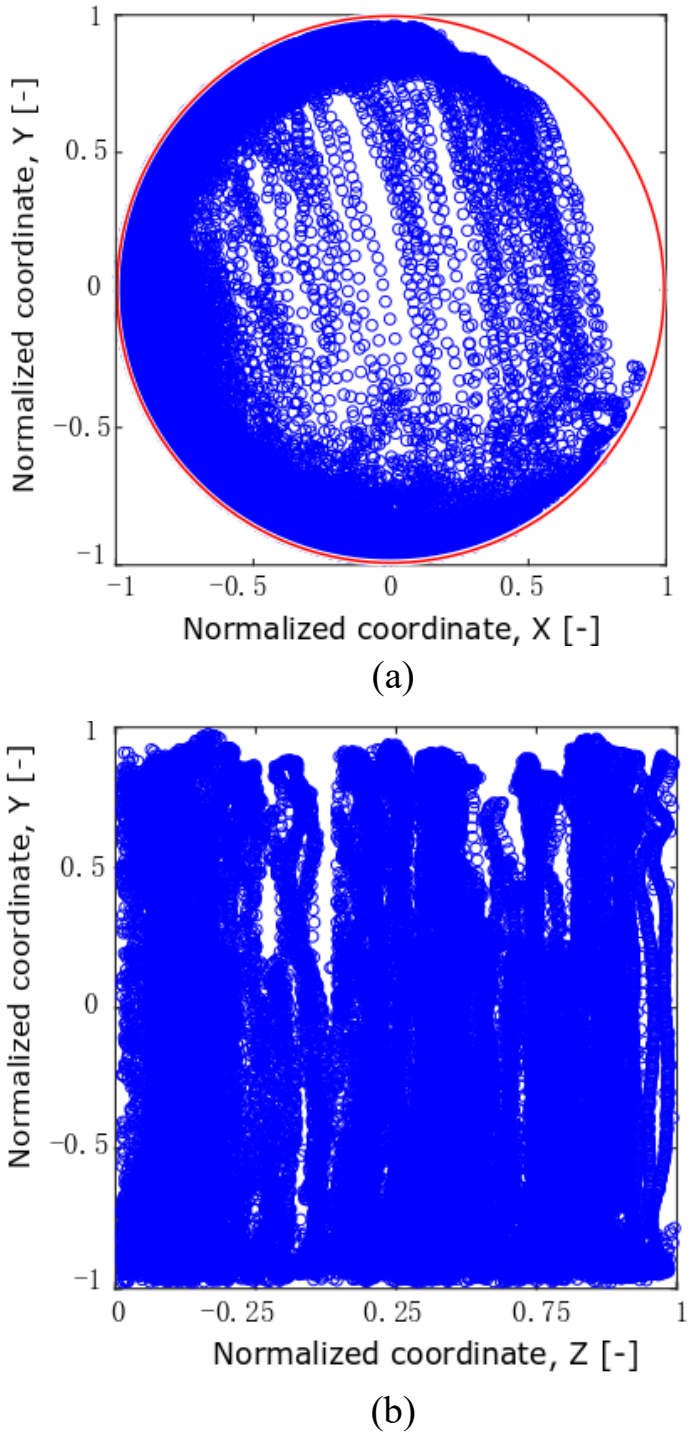

Figure 7.2: Tracer trajectories in the FRD obtained from MPT data for 5 % filling degree and 10 rpm drum rotating speed with plastic balls: (a) front view, (b) side view. The red solid line depicts the drum wall, blue circles denote the tracer position recorded at each time step.

In Fig. 7.3, the probability density functions of the vertical tracer position are illustrated for each time of three identical tests (plastic balls with 5 % filling degree and 10 rpm) with measurement durations of 120 s, 240 s and 360 s. Similar data density distributions

are visible from the three plots in Figs 7.3 (a)-(c). As the measurement duration time increases, the PDFs from the repetition tests become more similar, and the repeatability clearly improves. Based on these results, a measurement duration of 360 s is chosen for further experiments. Additionally, each experiment is repeated three times, and all data from the three trials is put together (18 min in total) for the following data analysis.

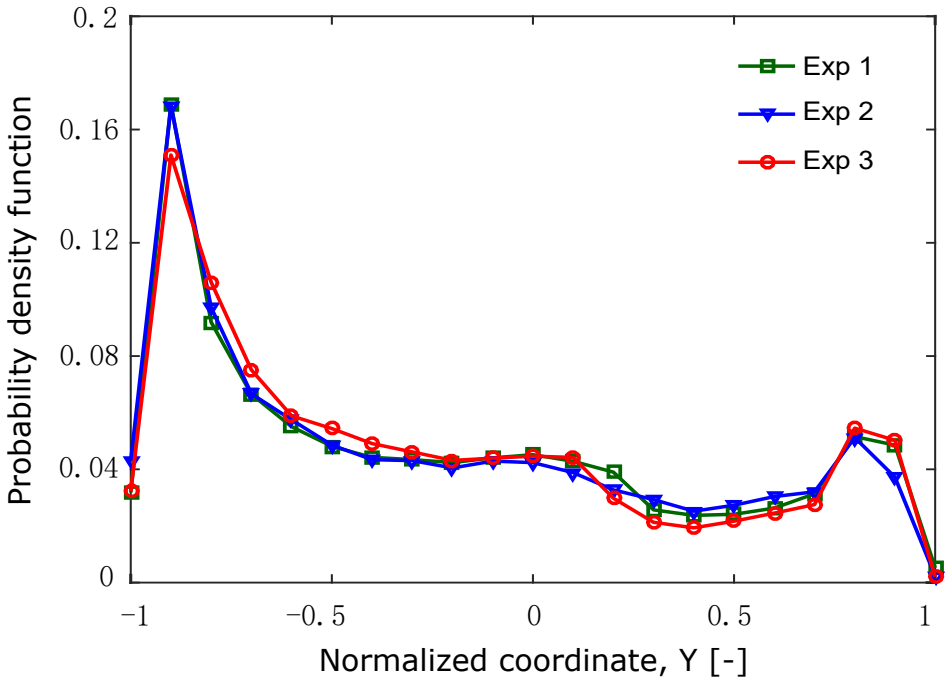

(a)

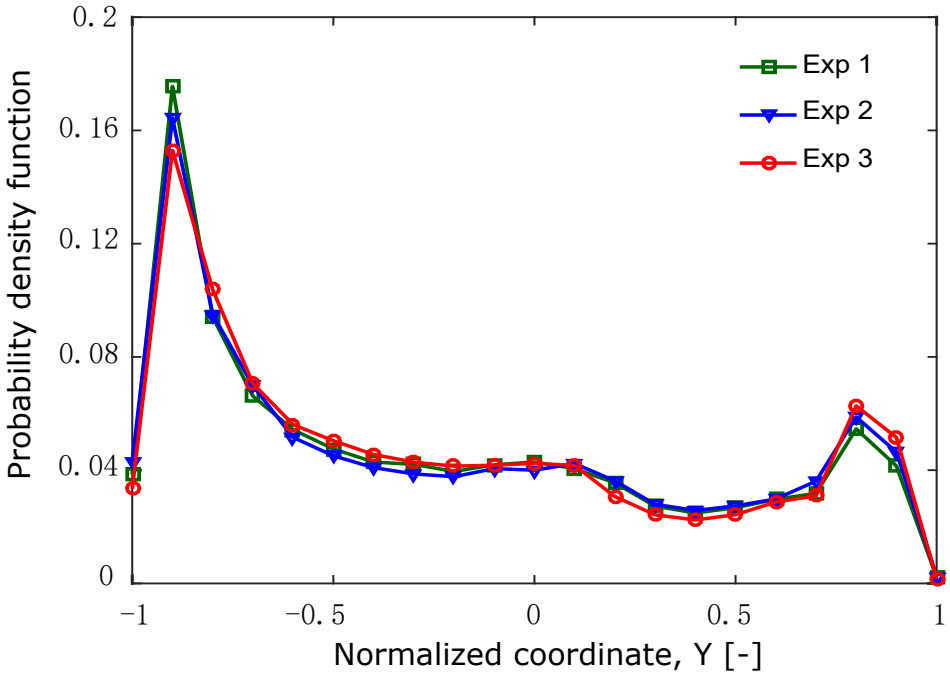

(b)

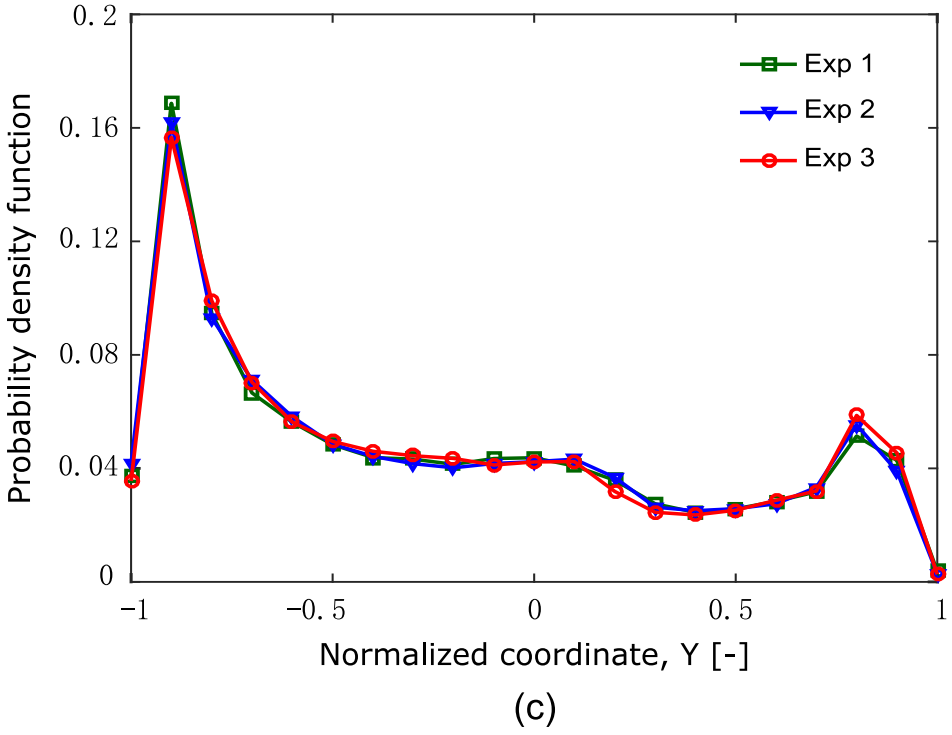

Figure 7.3: Probability density function of the particle vertical position in the FRD, plastic beads of 5 % filling degree with 10 rpm drum rotating speed, calculated for different experimental duration times: (a) 120 s, (b) 240 s, (c) 360 s.

7.2.2 Velocity vector distribution

The time-averaged velocity distribution of the tracer particle is investigated by moving in a bed of plastic balls of 5 % filling degree at 10 rpm drum rotating speed. The results are evaluated over the transverse cross-section in a specific axial slice of the FRD. In order to present the velocity vectors clearly over the transverse cross-section, only the data of 0.01 m axial length are shown in Fig. 7.4 within the z coordinate range from 0.085 m to 0.095 m.

As can be seen from Fig. 7.4 (a), the tracer particles in the dilute phase are subjected to free fall motion with an initial velocity and display relatively high translational velocities. The particles on the flights move with the rotating flights showing a quite regular velocity distribution. The particle bouncing phenomenon is observed at the bottom part of the drum. It occurs when a particle in free-falling motion collides with another particle, the rotating wall or a flight. This phenomenon is commonly observed in under-loaded drums and has a major effect on particle motion in this case [115].

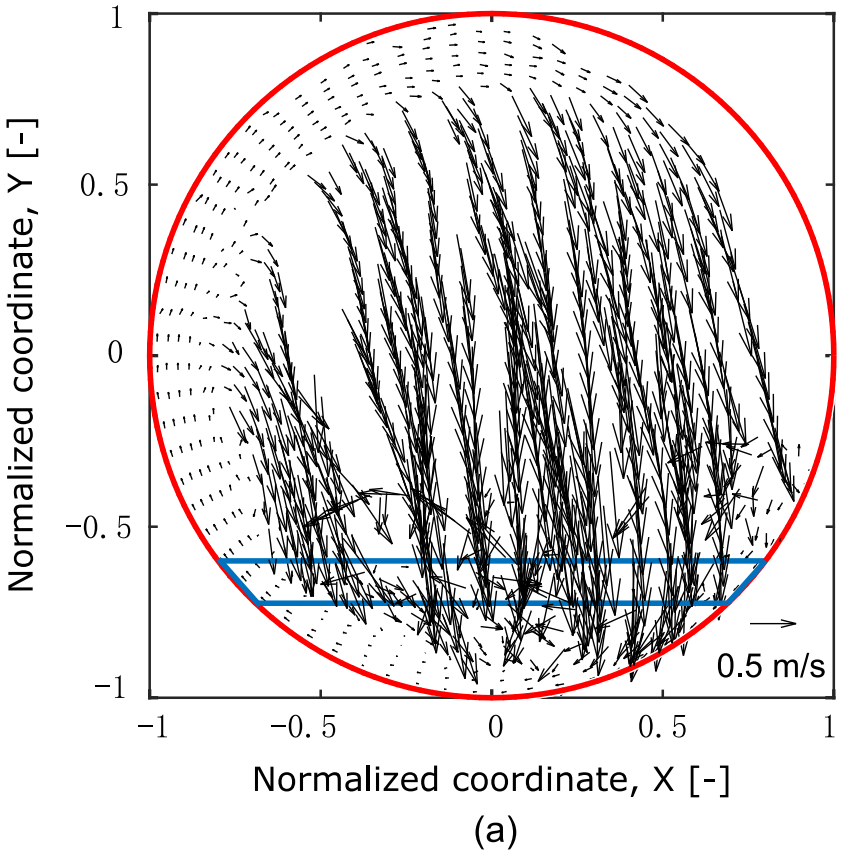

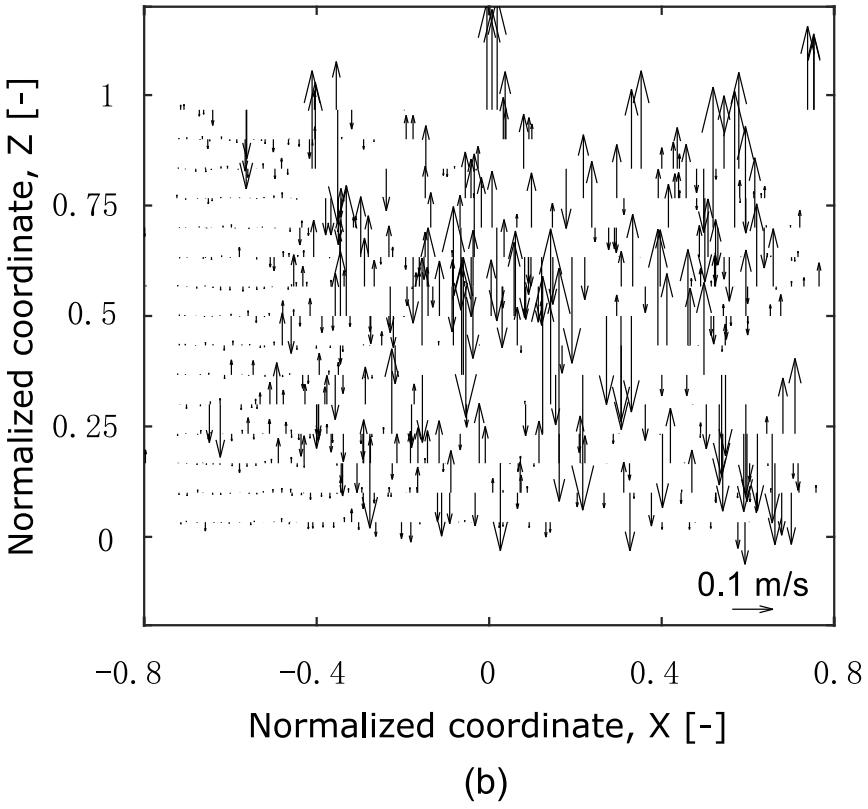

Figure 7.4: Time and space averaged velocity vectors of tracer measured with plastic beads of 5 % filling degree at 10 rpm drum rotating speed: (a) transversal vector magnitudes for the z coordinate range from 0.085 m to 0.095 m, (b) axial velocity distribution in a slice as depicted in (a) with blue lines.

In order to depict the axial velocity distribution of the particles, data are extracted from a slice of the cross-section marked with blue lines in Fig. 7.4 (a). These data are displayed in Fig. 7.4 (b). The particles in the dense phase region (left side) represent negligibly small axial velocities. While, visibly different and relatively large axial velocities are observed over the longitudinal coordinate for the dilute phase region. This result reflects that the bouncing effect has a positive impact on axial particle mixing.

7.2.3 Translational velocity

To obtain a complete picture of the three-dimensional particle velocity distribution in the FRD, the particle translational velocities V_x, V_y, V_z and the total velocity V are calculated from the MPT data using Eq. 7.1 and Eq. 7.2. The velocity distribution is investigated in dependence on the type of bed material (plastic balls, denoted by P; soybeans, denoted by S) and the drum rotation speed (10 - 40 rpm) at a drum filling degree of 5 %.

As can be seen from the Fig. 7.5, the three velocity components and the total velocity show a strong dependence on the drum rotation speed as expected. While plastic balls and soybeans display very similar distributions of the V_x and V_y velocities, the PDF of the velocity component V_z and that of the total velocity V exhibit differences between the bed materials. This can be seen in that the high-velocity tails of the distributions are more pronounced for soybeans. This result agrees with observations from Njeng et al. [41] who attained higher axial dispersion coefficients for larger particles in their experiments. The probability density functions obtained for the velocity components V_x, V_y, and the total velocity V display pronounced peaks triggered by the drum rotation, the maxima of which are near the absolute radial velocities of the flight tips $\omega_D \cdot r_H$. For better comprehension, the different radial velocities of the flight tip are illustrated in the diagrams as colored vertical lines for the respective rotating speeds. This effect is a result of the driving force of the flights acting on the particle flow.

As Fig. 7.5 (a) illustrates, the probability density functions of the translational velocity V_x exhibit two maxima for each of the different rotation speeds in the negative and positive velocity region, respectively. The first peak (left) is caused by particles in the lower part of the drum moving with the rotating drum wall and flights, whereas the second peak (right) represents particles moving on the flights in the upper part of the drum. As the rotation speed increases, the width of the profiles increases and the two maxima shift toward higher absolute values.

The translational velocity distributions of V_y (Fig. 7.5 (b)) also display a maximum that shifts to higher positive values and decreases in height as the rotation speed increases. These peaks mainly result from the driving effect of the flights. This is clear from the fact that the maxima are close to the radial velocities of the flight tip $\omega_D \cdot r_H$. In the negative velocity region, the profiles measured for different rotation speeds exhibit a similar trend. This is because particles undergo a free fall motion with an initial velocity in the gas phase

after they discharge from the flights, which is mainly influenced by gravity.

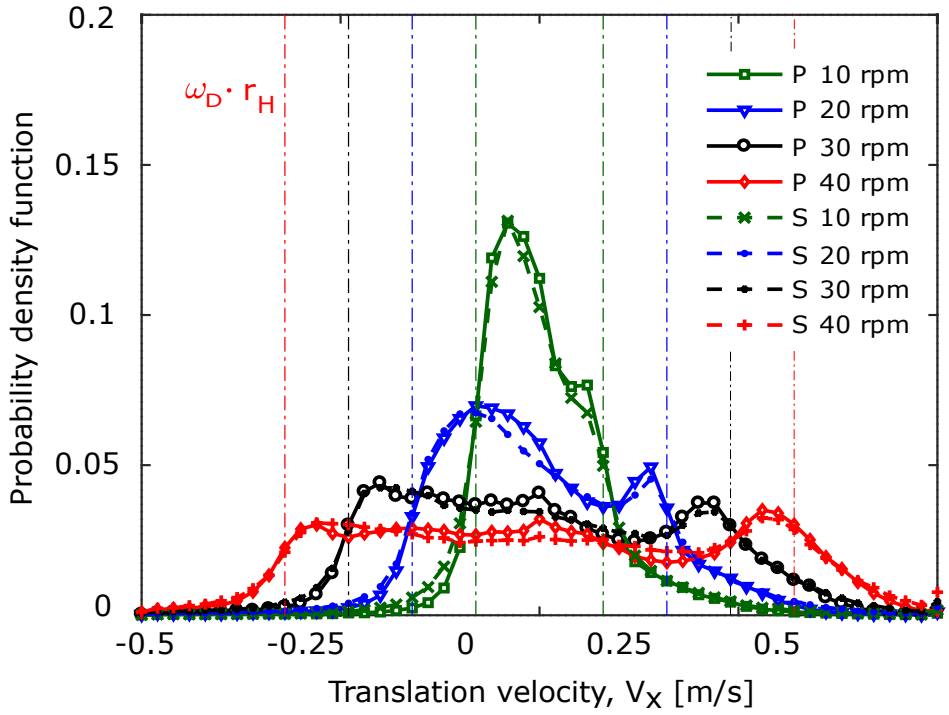

(a)

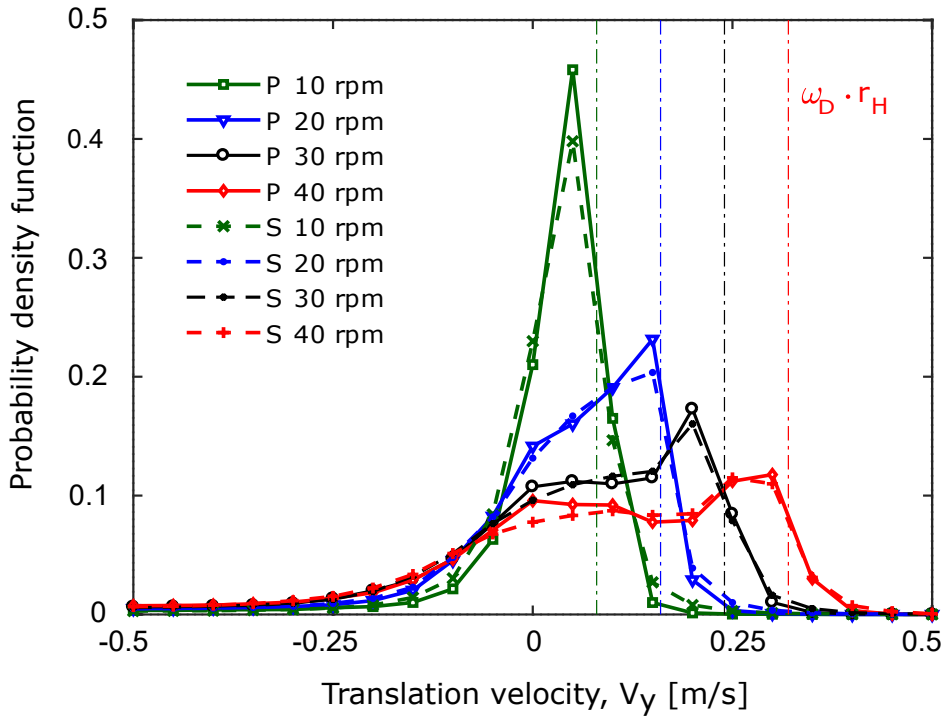

(b)

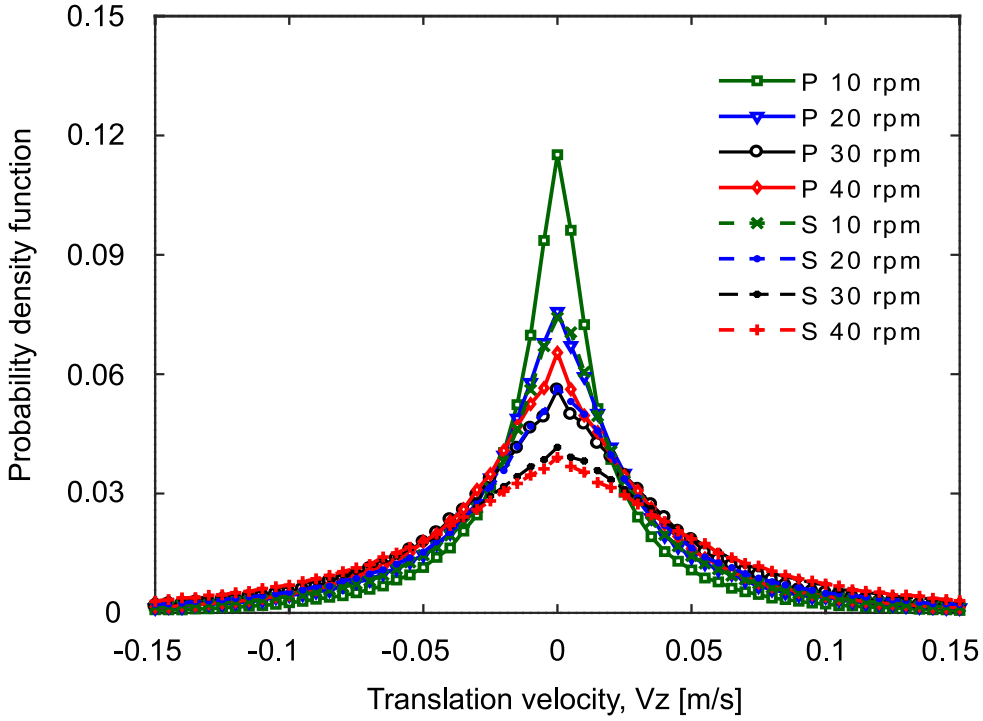

(c)

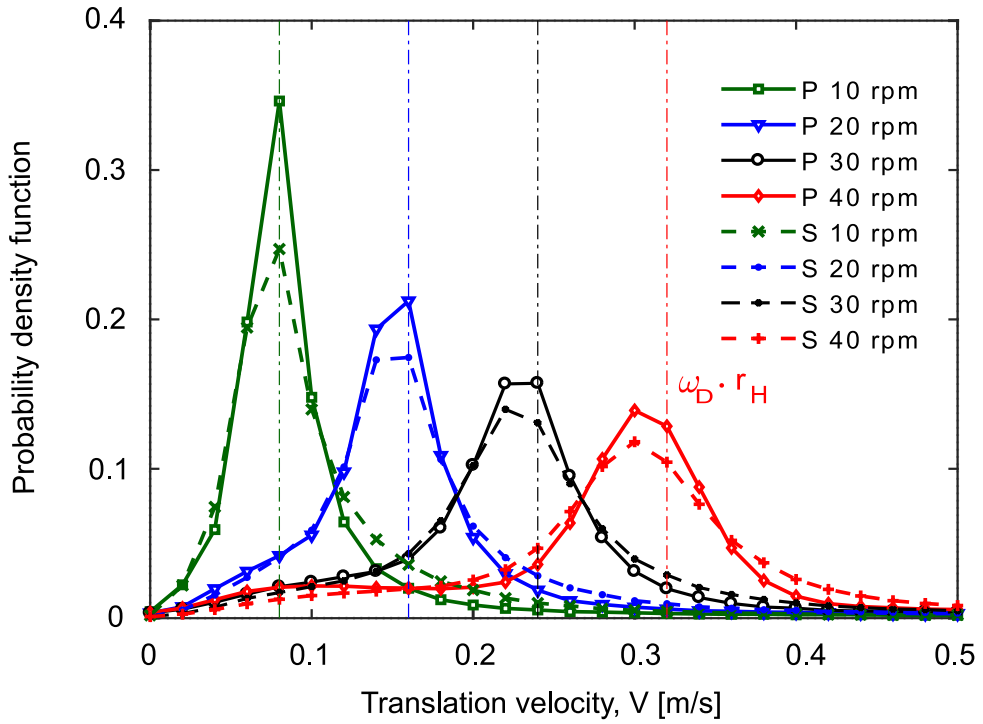

(d)

Figure 7.5: Effect of rotation speed on the translational velocity distributions of particles with 5 % filling degree. Probability density distributions of particle translational velocity components: (a) V_x, (b) V_y, (c) V_z and (d) total velocity V. Bed materials: plastic beads (P) and soybeans (S).

In axial direction, the velocity distributions display profiles which are similar in shape and symmetric, as shown in Fig. 7.5 (c). The axial velocities observed are positive or negative, indicating that the particles in the FRD move forward to the back wall or backward to the front wall with nearly the same probability. However, the axial velocity distribution widens as the rotation speed increases. This illustrates that axial dispersion increases accordingly. Certainly, the axial dispersion is enhanced due to the mixing effect of the flights and a faster granular circulating motion in the granular bed at higher rotating speeds.

The total translational velocity distributions shown in Fig. 7.5 (d) indicates the particle motion in the FRD is significantly influenced by the drum rotation speed in general. This is clear since the total velocities exhibit pronounced and separate probability density functions for each drum rotation speed. The measured distributions widen as the rotation speed increases.

7.2.4 Rotational velocity

From the MPT measurements conducted with plastic balls (denoted by P) and soybeans (denoted by S), the particle rotational velocity distributions are evaluated in dependence on the rotation speed at a drum filling degree of 5 %. The results are shown in Fig. 7.6. As the rotation speed is increased from 10 rpm to 40 rpm, the peak of the probability density distribution shifts towards higher absolute rotational velocities and becomes less sharp. This indicates that particles gain higher rotational velocities at increased drum rotation speeds, as expected. It should be noted that the curves have small positive intercepts with the ordinate of the diagram, meaning that non-zero values of the probability density function are attained at zero rotational velocity. This phenomenon is caused by particles located at the bottom of the flight holdup. In addition, the probability of these particles having zero rotational velocity is higher at lower drum rotating speeds.

As can be seen from the diagram (Fig. 7.6), soybeans present higher rotational velocities than plastic balls at all four rotating speeds. This is mainly confirmed by our own measurements of the dynamic angle of repose, which was considerably higher for soybeans than for plastic balls (Table 5.2). As reported by Jalaal and Granji [116] and Martino et al. [117], the particle motion on an inclined bed surface increases as the inclination angle, the particle density, and the particle diameter increase. Furthermore, as the rotating speed increases, the influence of the bed material - this means the differences between plastic balls and soybeans - gradually decreases.

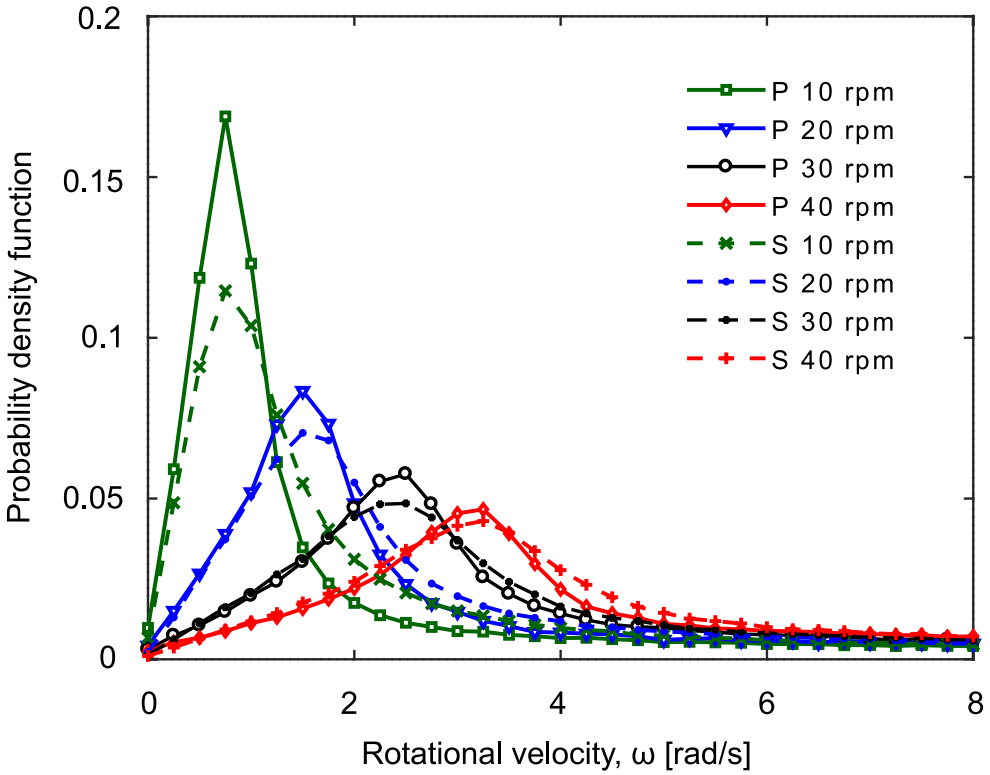

Figure 7.6: Effect of rotation speed on the rotational velocity distributions of particles with 5 % drum filling degree. Bed materials: plastic beads (P) and soybeans (S).

7.2.5 Falling time of dilute phase

The falling time of particles in the dilute phase determines the period of time in which the particles are fully exposed to the gas and directly affects the efficiency of heat exchange in practical applications. Using the method introduced in Section 7.1.4, curtains falling time can be measured by using the MPT system. Figure 7.7 illustrates the falling time as a function of the discharge angle at the conditions of 5 % filling degree and 10 to 40 rpm rotating speed for plastic balls and soybeans.

As is clear from the figure, the falling time of the two bed materials shows a similar trend over the discharge angle for the different drum rotating speeds. This confirms that gravity is the main factor affecting the motion of the dilute phase. Besides, it can be observed that the falling time attains a maximum value within the range from 40° to 70° of the discharge angle (flight located at the top left of drum) depending on the bed material and the drum rotating speed. Similar results were reported by Sunkara et al. [38] who measured the curtain height related to the discharge angle by analyzing images from experimental videos. This means, that the higher the rotating speed, the more the discharge point at which the longest falling time is attained is shifted to lower discharge angles. Thereby, the filling degree of the bed at the bottom decreases and, accordingly, the total filling degree of the flights increases. Furthermore, at higher drum rotating speeds, the falling time is slightly

longer in the lower region of the discharge angle before attaining the maximum (Fig. 7.7). The opposite phenomenon can be observed in the decreasing part of the curves.

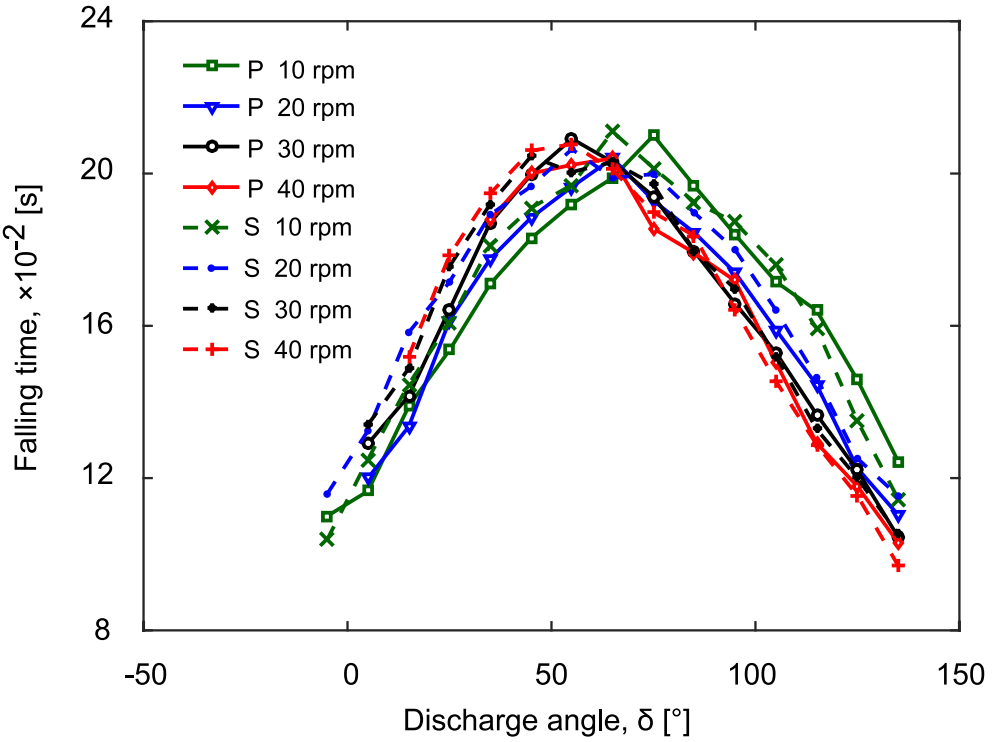

Figure 7.7: The falling time of dilute phase as a function of discharge angle. Bed materials: plastic balls (P) and soybeans (S). Filling degree: 5 %.

7.2.6 Velocity distribution in the dilute phase

In Fig. 7.8, the particle velocity components and total velocity of the dilute phase are illustrated against the normalized coordinate X in the equatorial region of the drum, see Fig. 5.3. The data are evaluated for plastic balls and soybeans of 5 % filling degree at various rotating speeds from 10 rpm to 40 rpm.

Figure 7.8 (a) shows that the drum rotating speed significantly influences the velocity component V_x of the dilute phase. Furthermore, the particle horizontal velocities V_x represent higher values than the corresponding radial velocities of the flight tip $\omega_D \cdot r_H$. This illustrates that the particles have obtained their initial velocity before discharging from the flight tip. This initial velocity is caused by the rolling motion of the particles on the top layer of flights holdup or on the surface of the flight. It should be noted that just few measuring values could be obtained in the lower region of the X axis at the high rotating speed of 40 rpm. This is because no curtains are observed in this region.

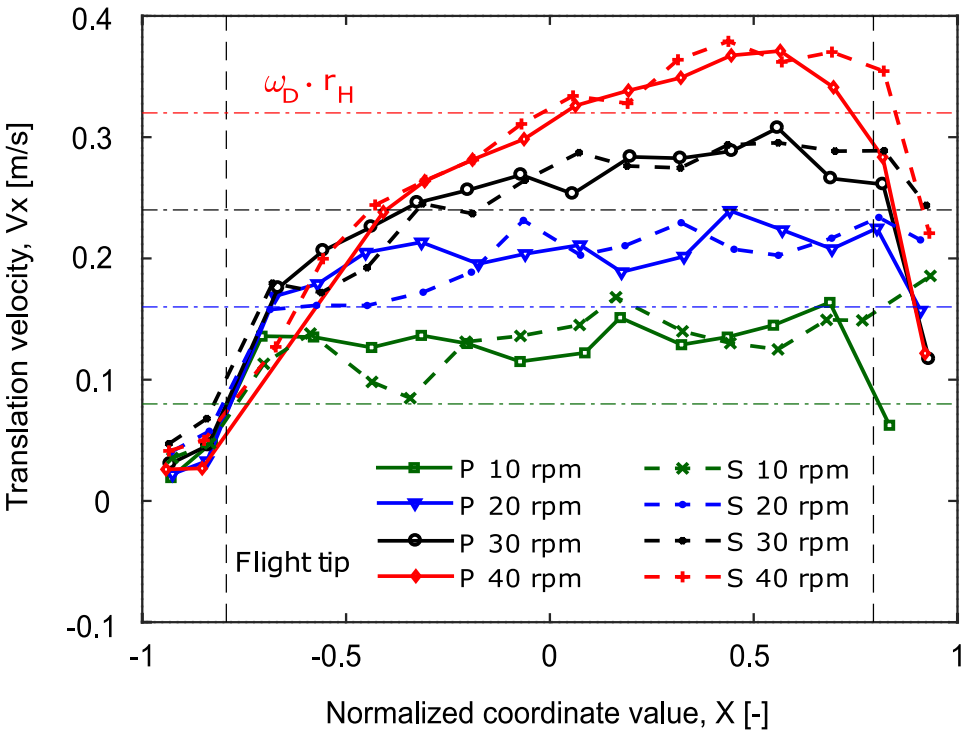
0.4
0.3
0.2
0.1
0
-0.1
-1
-0.5
0
0.5
1
Translation velocity, Vx [m/s]
Normalized coordinate value, X [-]
ω_D · r_H
Flight tip
P 10 rpm
P 20 rpm
P 30 rpm
P 40 rpm
S 10 rpm
S 20 rpm
S 30 rpm
S 40 rpm

(a)

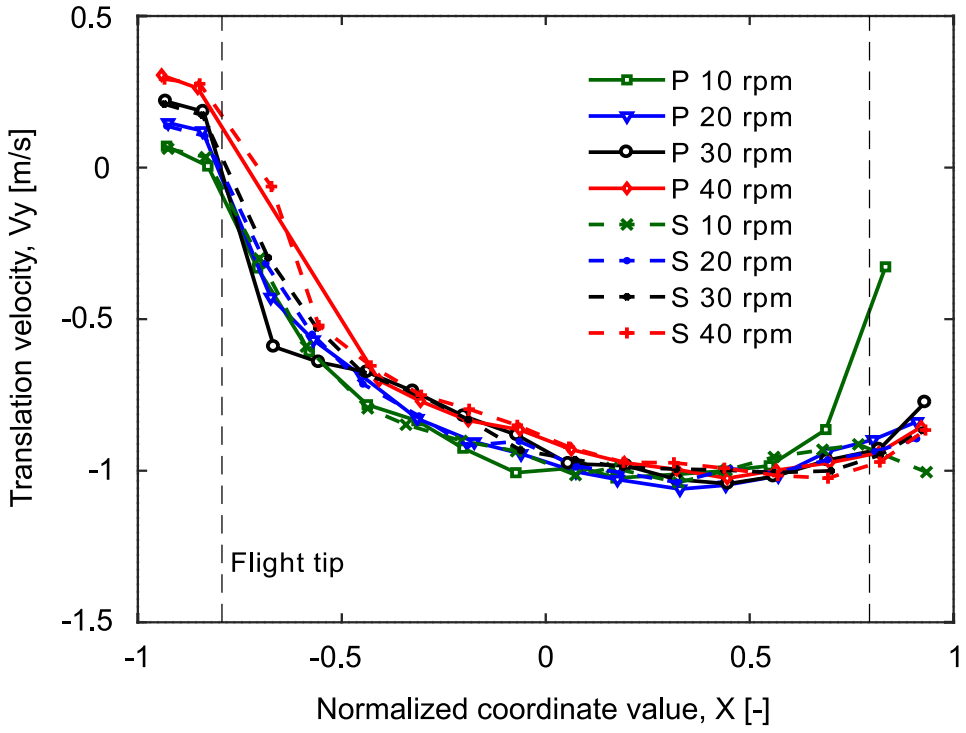
0.5
0
-0.5
-1
-1.5
-1
-0.5
0
0.5
1
Translation velocity, Vy [m/s]
Normalized coordinate value, X [-]
Flight tip
P 10 rpm
P 20 rpm
P 30 rpm
P 40 rpm
S 10 rpm
S 20 rpm
S 30 rpm
S 40 rpm

(b)

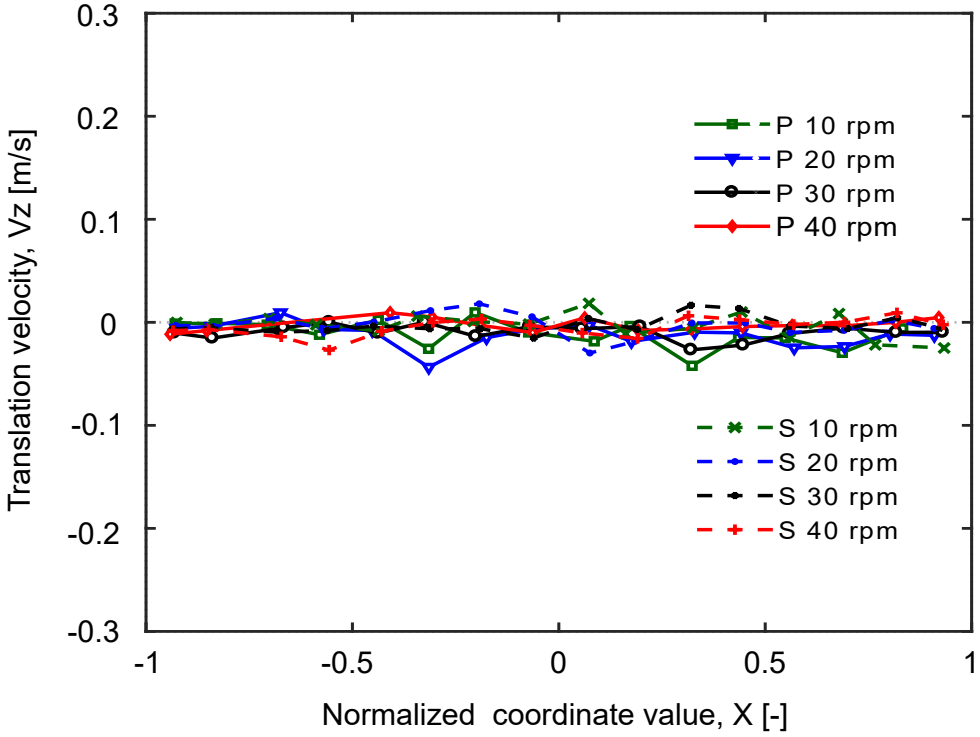

(c)

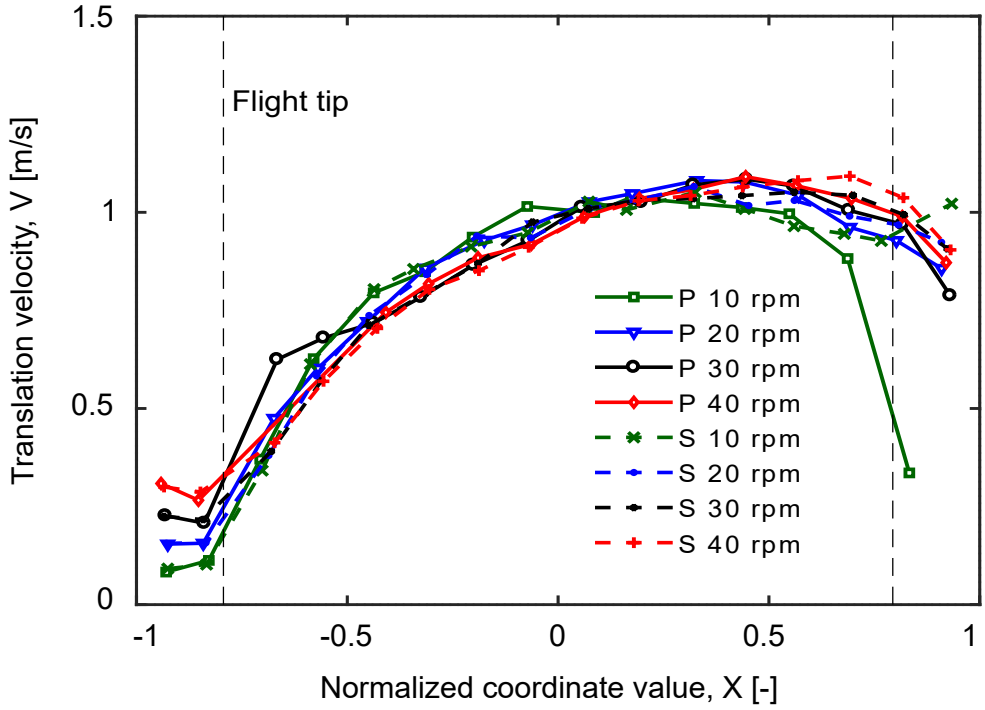

(d)

Figure 7.8: Effect of drum rotating speed on the translational velocity of the dilute phase in the equatorial region of the drum. Particle translational velocity components: (a) V_x, (b) V_y, (c) V_z and (d) total velocity V. Bed materials: plastic balls (P) and soybeans (S). Filling degree: 5 %.

The measurements of the vertical velocity component V_y are depicted in Fig. 7.8 (b). The figure illustrates that particles still located on the flights display obviously different vertical velocities at different rotating speeds as expected, see the region left from the flight tip position (auxiliary vertical line). Whereas, these differences are quickly eliminated in the dilute phase as soon as the particles cascade from the flights. In the left half of the drum, i. e. in the negative region of the X coordinate, the vertical velocity is higher at lower drum rotating speeds. However, this tendency gradually changes along the X axis and develops to the opposite in the positive region of the abscissa. To reach a certain point at the zero line ($Y = 0$, see Fig. 5.3), the discharge angle of a particle elevated at lower rotating speed is always higher than that of a particle elevated at higher rotating speed. In other words, the falling height from the flight tip to the zero line is bigger before the 12 o'clock position at lower drum rotating speed. The opposite phenomenon happens after the 12 o'clock position. The axial particle velocity in the dilute phase does not change as the rotating speed varies, as it is shown in Fig. 7.8 (c). From the total translational velocity distribution depicted in Fig. 7.8 (d), a quite similar curve tendency is shown compared to the velocity component V_y. This is clear since the absolute values of the particle vertical velocity are much higher than those of the other two velocity components.

Chapter 8

PTV measurements and DEM simulations of particle behavior

This chapter is based on Zhang et al. [81].

8.1 Transverse particle motion

As the drum rotates, particles switch continuously among the bed phase, flight phase, and dilute phase. The heat and mass transfer between particles and the gas takes place mainly in the dilute phase region during the drying or cooling processes. The number of particles in the dilute phase and the particle distribution in the cross-section of the drum are directly related to the drum performance [9].

By taking photos from the transparent front wall of an FRD, the image analysis method is commonly utilized to investigate the dynamic angle of repose, first discharge angle, flight holdup ratio, the falling height of curtains, as well as the particle residence time [10, 50, 51]. However, conventional processing of images is very time-consuming and difficult. Besides, there are few studies on the moving characteristics of particles, which may be due to the limitations of experimental techniques.

The PTV method can reveal particle distribution and instantaneous velocities by identifying and tracking the trajectory of individual particles [24, 118]. According to its tracking ability, the PTV method has been used on various granular media to study the velocity of spherical or non-spherical particles, particle dispersion, particle collision frequency, and particle exchange rate [82, 83, 85, 87, 89]. However, no other application of the PTV method to FRD has been reported.

Compared with conventional image analyses of FRD, which are based on the particle area in the region of interest, the PTV method calculates the particle ratios in the three

phases based on the corresponding numbers of particles. This means the PTV method can avoid the problems of identifying the drum edge and determining the porosity between falling particles in the FRD.

The aim of this chapter is to apply the PTV technique to FRD in order to study the motion of particles in detail. The drum with four rectangular flights is horizontally placed and filled with plastic balls. To easily analyze the particle motion in each of the three phases that can occur in the cross-section of the drum, the drum is over-loaded with filling degrees of 10 %, 15 %, or 20 %. Three rotating speeds of 10 rpm, 20 rpm, and 30 rpm are used in this work. Detailed information about experiment setups is given in Chapter 5. The parameters used in the segmentation and tracking processes of the PTV method have been calibrated in Section 4.3.

DEM simulations are also conducted to predict the particle motion in the FRD, as introduced in Chapter 6. A total of 2316, 3474 or 4632 particles are inserted into the simulation chamber, corresponding to filling degrees of 10 %, 15 %, and 20 %. The parameters used in the DEM simulations have been calibrated and verified in Section 6.4.

The results from PTV measurements and DEM simulations are presented and compared in terms of the holdup ratio and cascading rate of a single flight, the residence time distribution in the dilute phase, the particle ratios of the three phases, as well as the average velocity and granular temperature of the particle system. The effects of drum rotating speed and drum filling degree on the particle motion are studied in detail.

8.2 Results and discussion

8.2.1 Holdup and cascading ratio of single flight

To study the influence of drum rotating speeds on the particle motion in the flight phase, the holdup ratio (mass of particles in the flight to total mass of particles) and cascading rate of a single flight are investigated by PTV measurements and DEM simulations. Figure 8.1 illustrates the holdup ratio of a single flight as a function of the discharge angle attained in the drum operated at 10 % filling degree and 10 - 30 rpm. Symbols in the figure represent the experimental results from the PTV measurements. The error bars on the symbols are the standard deviations of the repeated measurements. The lines represent the data from DEM simulations. The data analysis starts at a discharge angle of 0° although the flight already starts to discharge before this angle. For the particles leaving from the flight in the lower half of the drum, the spacing between the particles is very small and the falling height is quite short. Hence, the contact between particles and hot air is low in this region $\delta < 0°$ and can be neglected. Thus, the flight and dilute phases are only detected for discharge angle $\delta \geq 0°$.

As Fig. 8.1 depicts, as the drum rotating speed increases, the final discharge angle

increases from 124.0° to 133.5° and 140.0° at 10, 20, and 30 rpm, respectively. The one-way ANOVA analysis evidences that there is a positive effect between the drum rotating speeds in the discharging range of $0 < \delta < 36.00°$ and $102.96° < \delta < \delta_L$. Combined with the Tukey-Kramer multiple comparison test, the results reveal that there is a significant difference between 10 and 20 rpm when the $0 < \delta < 19.44°$ and $106.56° < \delta < 133.20°$. For the rotating speeds between 10 and 30 rpm, these range are $0 < \delta < 36.00°$ and $102.96° < \delta < 139.68°$. Comparing 20 and 30 rpm, a higher holdup ratio of single flight is indicated at 30 rpm in the range of $0 < \delta < 33.84°$ and $119.52° < \delta < 139.68°$. These results illustrate the positive effect of the drum rotating speed on the drum operation by increasing the flight filling degree and widening the flight discharging region. It should be noted that almost one-third of the total particles are captured by a single flight when the drum rotates at 30 rpm. This result is caused by the low filling degree of 10 % and the high drum speed.

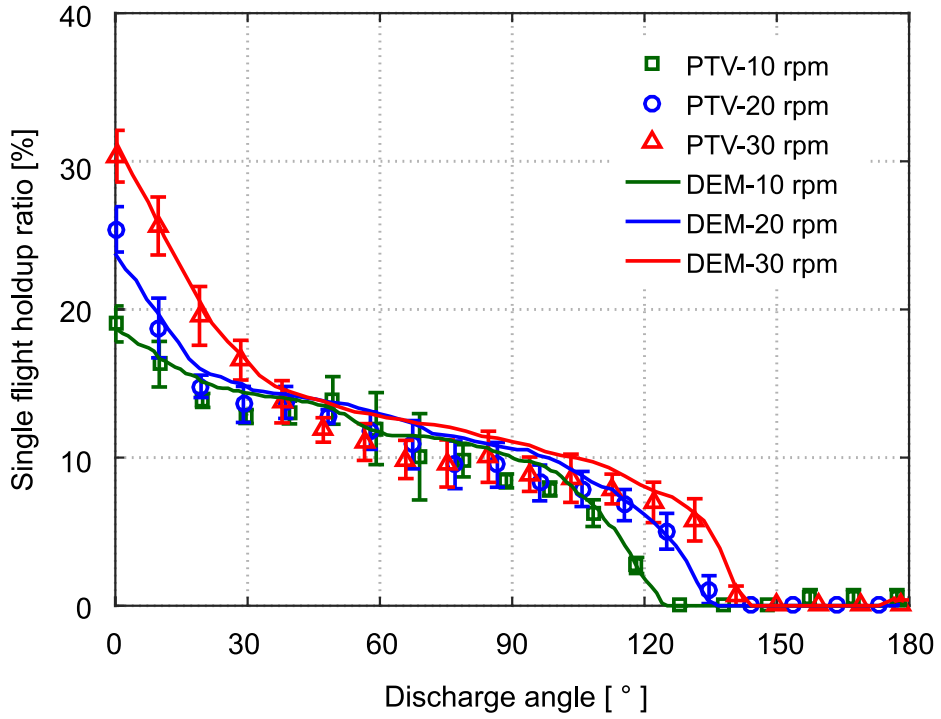

Figure 8.1: Single flight holdup ratio as a function of the discharge angle for the drum filled with 10 % degree at the rotating speeds of 10, 20 and 30 rpm. Bed material: plastic balls. Symbols denote experimental data and the lines represent simulation results.

As can be seen from the graphs, the DEM model predictions agree well with the PTV measurements, except some deviations in the middle region of flight unloading at higher drum rotating speeds. It is worth mentioning that the solids area of the first unloading flight (FUF) achieves saturation when the drum is design-loaded. As the drum loading is increased, the carrying capacity of the FUF does not change. The additional bed material will just increase the particle ratio in the bed phase. Moreover, in this study, the FUF

position is lower than the zero discharge angle because the drum is overloaded at all three filling degrees. This means that the single flight holdup ratio at $\delta \geq 0°$ is the same for the three filling degrees (Fig. 8.1).

Based on these data, the cascading rate of a single flight is studied by calculating the relative change in flight holdup ratio as a function of the discharge angle. The cascading rate of the flight f_{ca} is estimated from the following equation

$$f_{ca}(\delta) = \frac{f_F(\delta) - f_F(\delta + \triangle\delta)}{f_F(\delta = 0)}. \tag{8.1}$$

In the equation, $f_F(\delta)$ is the holdup ratio of the flight at the discharge angle δ and the $\triangle\delta$ is equal to 7.2°. The influence of drum rotating speed is investigated for a drum filling degree of 10 %. The results are shown in Fig. 8.2. As the figure depicts, the flight unloading rate is relatively high in the initial period, which is caused by the high flight filling degree in this region among other things. Then the cascading rate continues to decrease. This is because the discharge angle reaches the local kinetic angle of repose $\delta = \gamma$, see Sunkara et al. [119]. The state of low cascading rate remains for a period of time. After that, the cascading rate steeply increases and attains a second maximum. This increase and the maximum are mainly geometrically based and influenced by the design of the rectangular flight and the kinetic angle of repose. Thereby, as the drum rotates the length of the surface line increases and hence also the length and depth of the active layer at the flight. Finally, the cascading rate sharply declines until the flight gets empty. As compared to other bed materials, this decrease is quite steep and mainly caused by the relatively big particle size of the plastic balls rolling easily down the inclined lip of the flight l_2. A similar flight discharging behavior was confirmed by Sunkara et al. [8] through mathematical model prediction and image-based experimental measurement.

According to the ANOVA, the cascading rates of the single flight show significant difference among the three rotating speeds ($P < 0.05$) in the discharge regions of $5.76° < \delta < 34.56°$ and $95.76° < \delta < \delta_L$ (except in individual cases). According to the multiple comparisons, the cascading rates of the single flight between two rotating speeds of 10 and 20 rpm, 10 and 30 rpm, and 20 and 30 rpm have significant differences in the initial discharging period of $5.76° < \delta < 19.44°$, $6.48° < \delta < 25.20°$, $7.20° < \delta < 34.56°$, respectively. In the last discharging period, significant differences in the above three groups appear from the discharge angles of 98.64°, 95.76°, and 113.04°, respectively. Combining with the results on flight holdup ratio illustrates that the drum speed has a positive effect on the particles of flight phase. Moreover, this influence is mainly in the early and last periods of flight discharge.

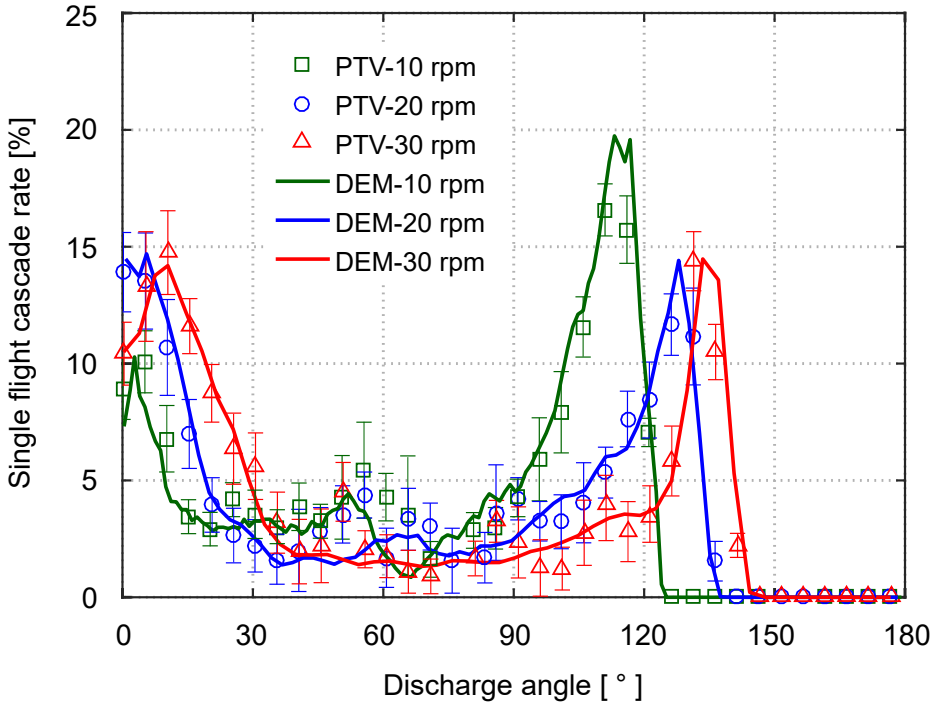

Figure 8.2: Cascading rate of a single flight versus discharge angle, measured and calculated at 10 % filling degree and rotating speeds of 10, 20 and 30 rpm. Bed material: plastic balls.

8.2.2 Falling time distribution of dilute phase

The falling time of particles in the dilute phase, leaving from the flight tip to the bottom of the drum or colliding with the rotating flight and wall, is estimated to study the particle motion by the PTV method and DEM simulation. The results are shown in Fig. 8.3 illustrating the effect of drum rotating speed on the falling time distribution in the dilute phase. The drum is operated at a filling degree of 10 % and rotating speeds of 10, 20 and 30 rpm. As the graph shows, the probability density function (PDF) of the falling time displays a maximum in the range between 0.08 s and 0.17 s depending on the drum rotating speed. Furthermore, both the falling time distribution and its maximum are shifted to higher values for the lowest drum rotating speed of 10 rpm. This means that although the flight holdup is smaller at 10 rpm, the particles are more intensively in contact with the air as compared to higher drum rotating speeds.

As compared to the PDF obtained at 20 rpm, the curve of the drum operating at 30 rpm has a lower peak and shows a more noticeable distribution after attaining the maximum. This illustrates that as the drum speed continues to increase, the overall falling time of particles is extended. As confirmed by our previous study in Section 7.2.5, the falling time in the dilute phase increases in the lower region of the discharge angle before attaining the longest falling time, and the opposite phenomenon can be observed after the maximum [65]. Combined with the study in Section 9.2.1, this illustrates that as the drum rotating speed

increases, the influence of the drum speed on the flight and dilute phases in the early period of discharging will gradually be greater than that in the last period.

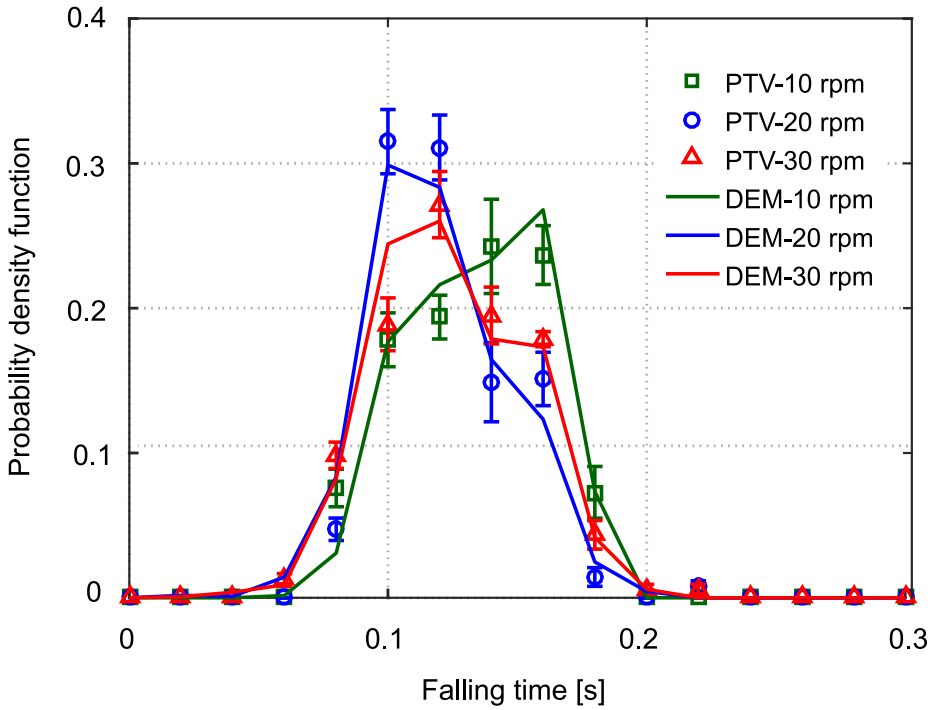

Figure 8.3: Falling time distribution in the dilute phase, measured and predicted at a filling degree of 10 % and rotating speeds of 10, 20 and 30 rpm. Bed material: plastic balls.

8.2.3 Particle ratios of bed, flight and dilute phases

When a drum is rotating, particles continuously switch between the bed phase, flight phase and dilute phase. The particle ratios of the three phases are calculated as

$$f_\lambda = \frac{N_\lambda}{N_F + N_D + N_B}, \quad \lambda = F, D, B. \tag{8.2}$$

f_F, f_D and f_B represent the particle ratio of dilute phase, flight phase and bed phase in the particle system, respectively. N_F, N_D and N_B are the numbers of particles in the flight phase, dilute phase and bed phase, respectively.

The particle ratios are obtained from the PTV measurements and DEM simulations, which have been conducted for a filling degree of 10 % and rotation speeds of 10, 20, and 30 rpm. The results are shown in Fig. 8.4 illustrating the particle ratios as a function of time. Generally, all the particle phases undergo periodic changes in every quarter of the drum rotating cycle, which is 1.5 s, 0.75 s, and 0.5 s for the rotating speeds of 10 rpm, 20 rpm, and 30 rpm, respectively. By comparison with the sub-figures (a), (b) and (c), a major portion of the total number of particles corresponds to dense phase in the entire rotation cycle. This high ratio comes from the relatively high filling degree used in this work with the aim to provide sufficient information about the bed phase.

As Fig. 8.4 (a) depicts, the drum rotating speed exerts a positive effect on the ratio in the flight phase. The minimum values in the flight phase obtained from the measurements at different rotating speeds are similar, about 10.0 %. The average maximum ratios of flight phase are 27.7 %, 33.0 %, 36.2 % for rotating speeds of 10 rpm, 20 rpm, and 30 rpm.

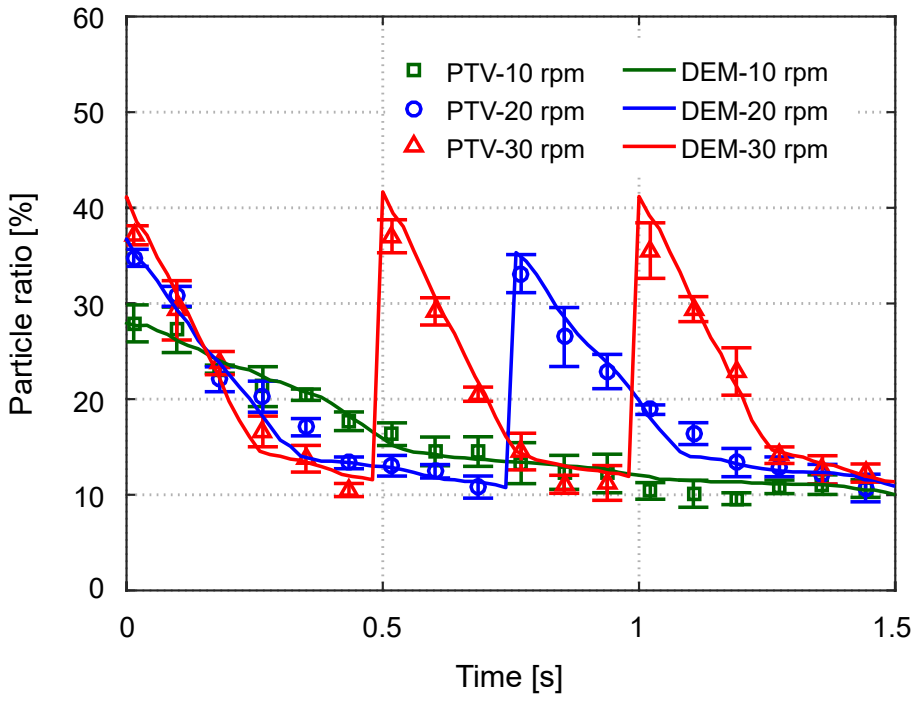

(a)

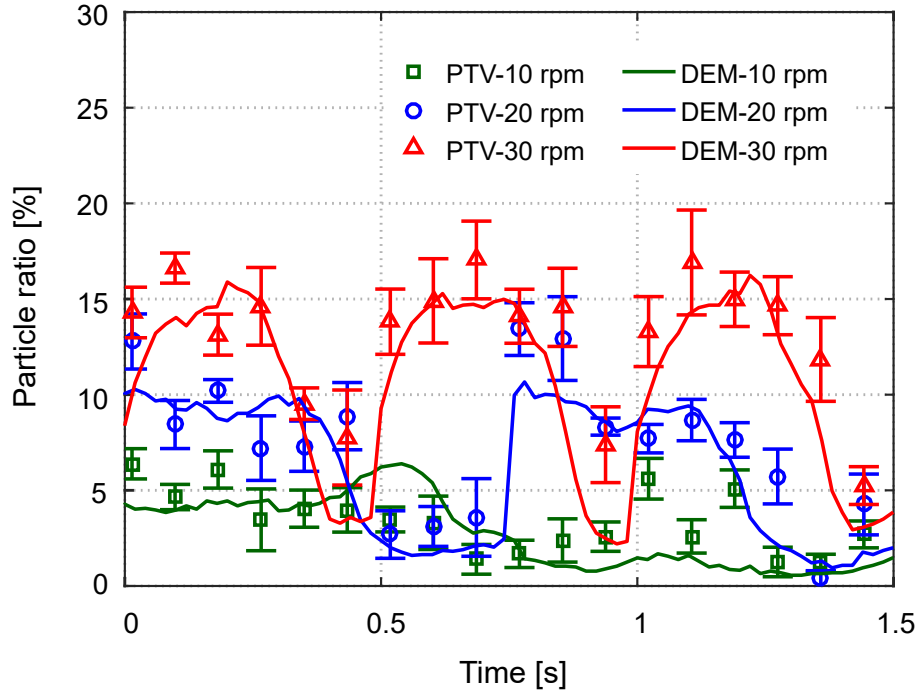

(b)

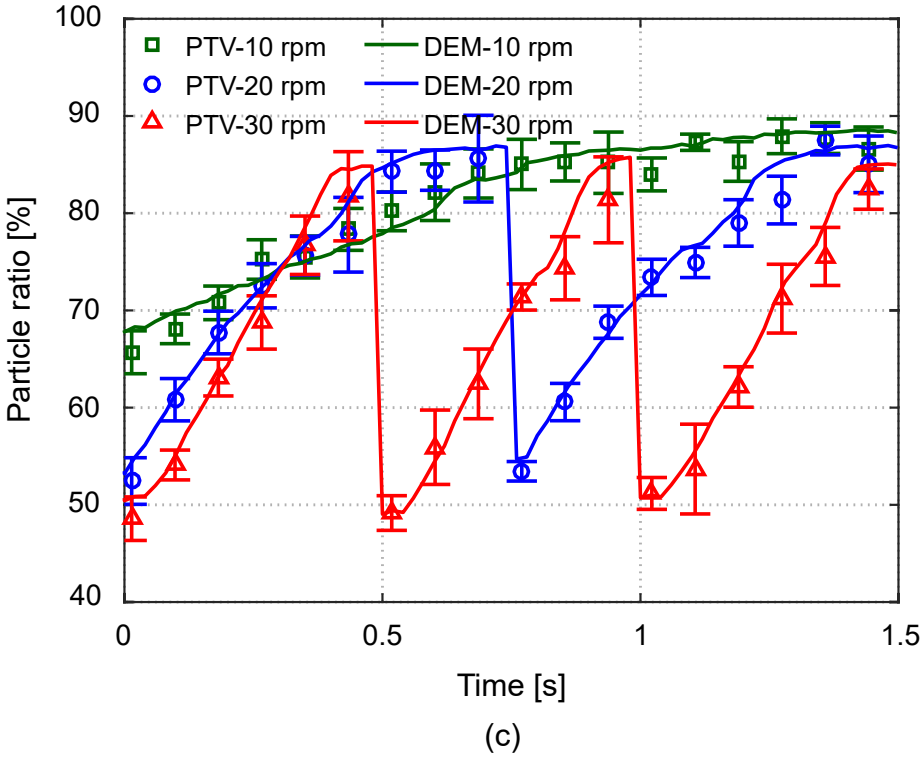

Figure 8.4: Particle ratios of three particle phases as a function of time: (a) flight phase, (b) dilute phase, (c) bed phase. The drum was operated at 10 % filling degree and rotating speeds of 10, 20, and 30 rpm. Bed material: plastic balls. $t = 0$ at $\delta = 0°$.

The particle ratio in the dilute phase (Fig. 8.4 (b)) also shows a strong dependence on the drum rotating speed. This is mainly due to the fact that more flight phase exists at higher drum rotating speeds, which further produces more dilute phase. Consequently, the particle ratio in the bed phase slightly decreases as the drum speed increases, see Fig. 8.4 (c). Besides, the lower ratio in the bed phase at higher drum speeds results in more intense particle-flight and particle-wall collisions.

As Fig. 8.4 illustrates, a good agreement is observed for the particle ratios in the three phases, especially the flight phase and bed phase. In the dilute phase, the PTV data are consistent with the trend of DEM data, but with slightly higher values and standard deviation. This may be caused by the fact that particles located on the surface of the granular bed but not in the first layer, which have relatively high vertical coordinate values and velocities, are incorrectly detected and counted as belonging to the dilute phase.

Averaged particle ratios of the three phases calculated from 1.5 s of DEM simulations for drum rotated at various speeds are listed in Table 8.1.

Table 8.1: Averaged particle ratios of three phases calculated from DEM simulations.

Drum speed [rpm]	Flight phase [%]	Dilute phase [%]	Bed phase [%]
10	16.02	2.82	81.16
20	18.44	6.28	75.28
30	20.93	11.63	67.44

8.2.4 Average velocity of the particle system

The translational average velocity values $V_{2D}(t)$, $V_x(t)$ and $V_y(t)$ in the particle system at time step t are calculated as

$$V_k(t) = \frac{1}{N_p} \sum_{i=1}^{N_p} |u_k(i,t)|, \quad k = x, y; \tag{8.3}$$

$$V_{2D}(t) = \frac{1}{N_p} \sum_{i=1}^{N_p} \sqrt{V_x(t)^2 + V_y(t)^2}. \tag{8.4}$$

$u_k(i,t)$ is the value of the velocity component k of individual particle i at time step t. N_p is the total number of particles in the FRD.

The influence of different drum rotating speeds on the particle system in FRD is also studied by evaluating the average velocity of all particles as a function of the rotating time. The results are illustrated in Fig. 8.5. The data are obtained from experimental investigations and DEM simulations for the cases with a filling degree of 10 % at rotating speeds of 10 rpm, 20 rpm and 30 rpm.

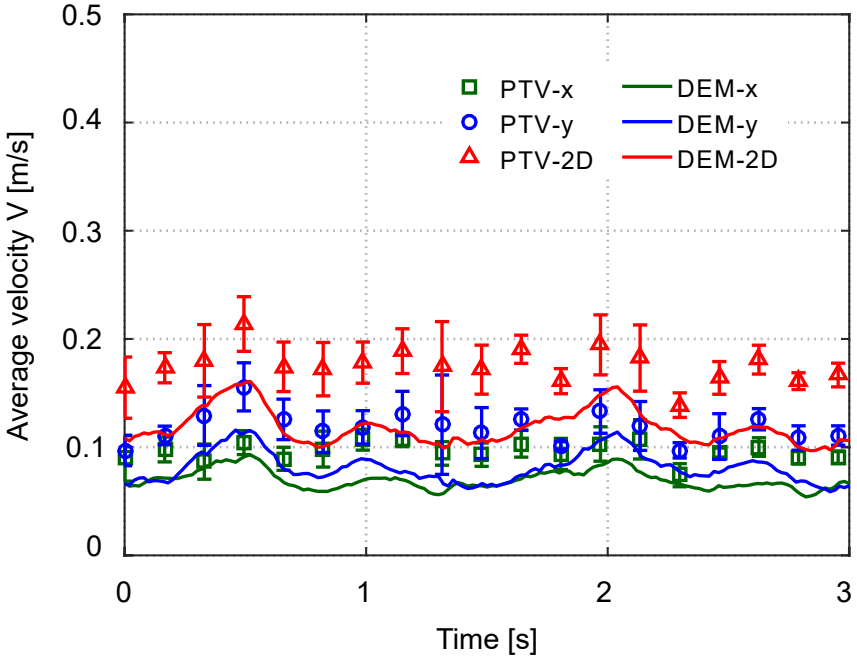

(a)

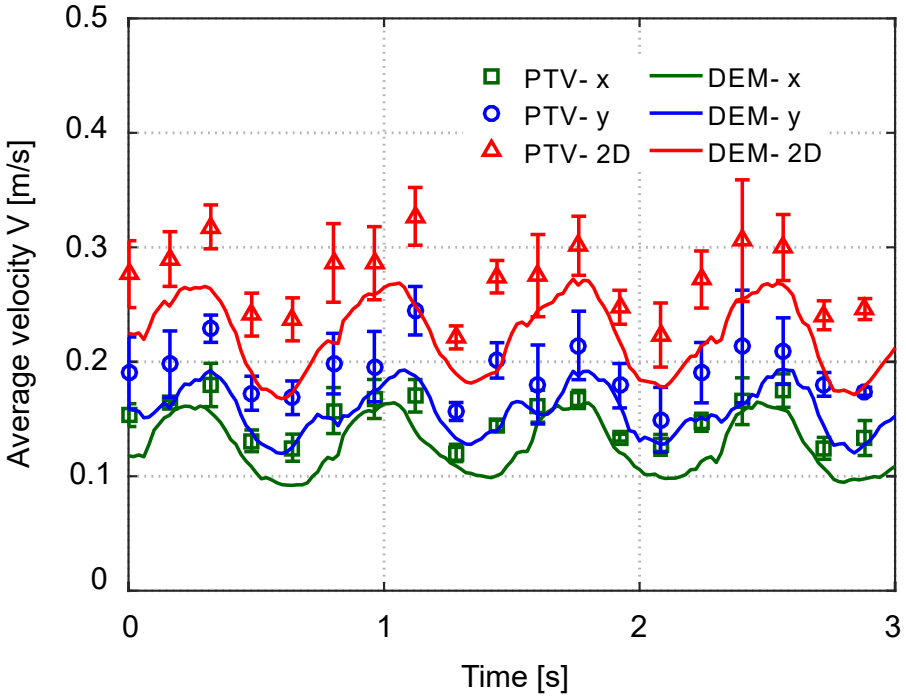

(b)

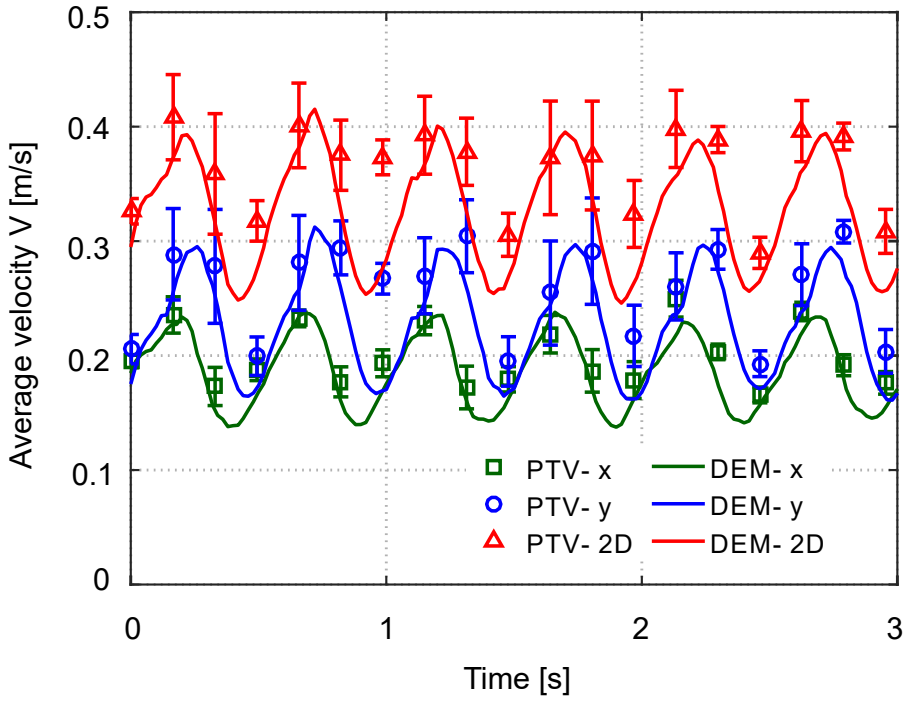

(c)

Figure 8.5: Averaged velocity of all particles as a function of time for the drum with 10 % filling degree operated at three different rotating speeds, together with components in x and y directions: (a) 10 rpm, (b) 20 rpm, (c) 30 rpm. Bed material: plastic balls. $t = 0$ at $\delta = 0°$.

As the figure depicts, all velocities undergo periodic fluctuations over time with a

corresponding frequency, which is 1.5, 0.75 and 0.5 s for the rotating speeds of 10 rpm, 20 rpm and 30 rpm, respectively. As the rotating speed increases, the particle velocity components and the total velocity increase. The reason for this is that higher rotating speeds introduce more energy into the granular system and raise interactions between particles. Compared with the velocity component $V_x(t)$, the velocity component $V_y(t)$ of particles in the FRD has a larger value. This is caused by the effect of gravity acting on the particles, especially in the dilute phase. Figure 8.5 also illustrates that the DEM results agree reasonably with the measurements and that the data trend is consistent. However, as the drum rotating speed decreases the deviations increase.

With the same method, the effect of the drum filling degree on the particle system is investigated for the drum operated at 30 rpm and filling degrees of 10 %, 15 % and 20 %. The results calculated from experimental and simulation data are illustrated in Fig. 8.6. As can be seen from the graphs, the degree of fluctuations of the average velocities $V_x(t)$, $V_y(t)$ and $V_{2D}(t)$ becomes flat when the filling degree increases. This is because more particles move in the bed phase at higher filling degree. Moreover, the vertical velocity component comes closer to the horizontal velocity component as the fraction of dilute phase is reduced.

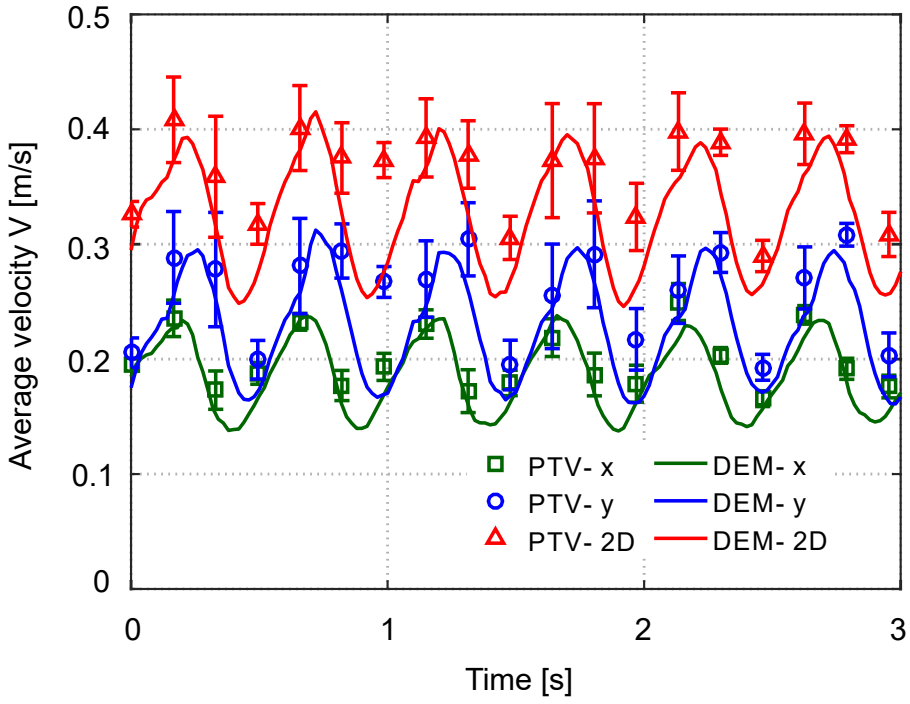

(a)

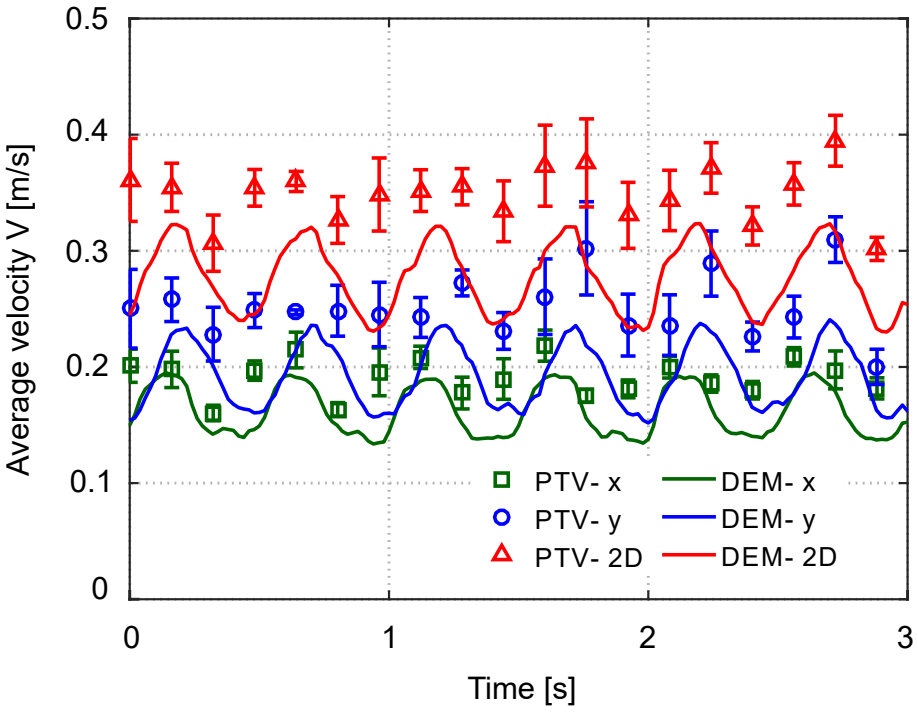

(b)

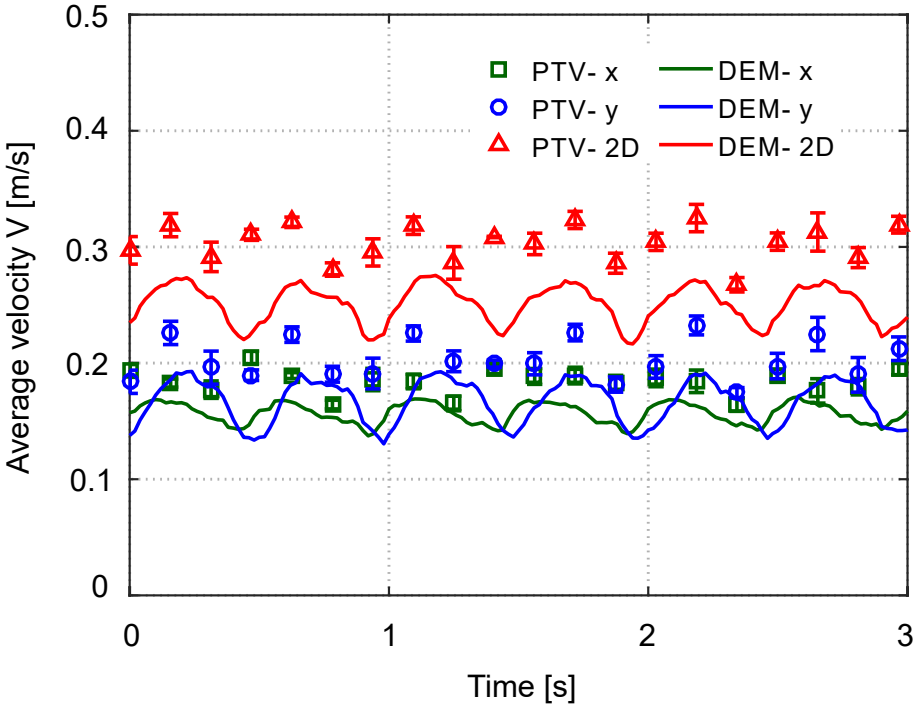

(c)

Figure 8.6: Averaged velocity of all particles as a function of time for the drum rotated at 30 rpm with three filling degrees, together with components in x and y directions: (a) 10 %, (b) 15 %, (c) 20 %. Bed material: plastic balls. $t = 0$ at $\delta = 0°$.

In addition, the DEM predictions also agree well with the PTV data at lower filling

degrees, see Fig. 8.6. However, there are some deviations in the cases of the drum at filling degrees of 15 % and 20 %, especially for the vertical velocity V_y and total velocity V_{2D}. It could be explained by the effects of end wall friction in the rotating drum [120–122]. Although the end wall is smooth, there is still some friction between the solids and the wall. This friction causes the dynamic angle of repose near the wall to be bigger than that in the axial center of the drum. With the filling degree of 10 %, the movement of the particles in the material bed is mainly driven by the rotating flights. However, as the filling degree increases to 15 % and 20 %, the bed height is higher than the radial flight length l_1. In this condition, the bed particles undergo a rolling or cascading motion in the bottom part of the drum which is subjected to the end wall friction. The particles near the wall have a larger vertical velocity due to a bigger dynamic angle of repose, in which case the corresponding PTV data from 2D measurement is larger than the DEM results.

As discussed above, both the drum filling degree and rotating speed have a great influence on the particle system in FRD. To study the effects of these two parameters quantitatively, the time averaged velocity $V_{2D}(T)$ is calculated for a duration of 3 s as

$$V_{2D}(T) = \frac{1}{N_t} \sum_{t=1}^{N_t} V_{2D}(t). \tag{8.5}$$

N_t is the total number of time steps in a rotation cycle.

The results are shown in Fig. 8.7 where the time averaged velocity is plotted as a function of the drum rotating speed. The filling degree is varied from 10 % to 20 %.

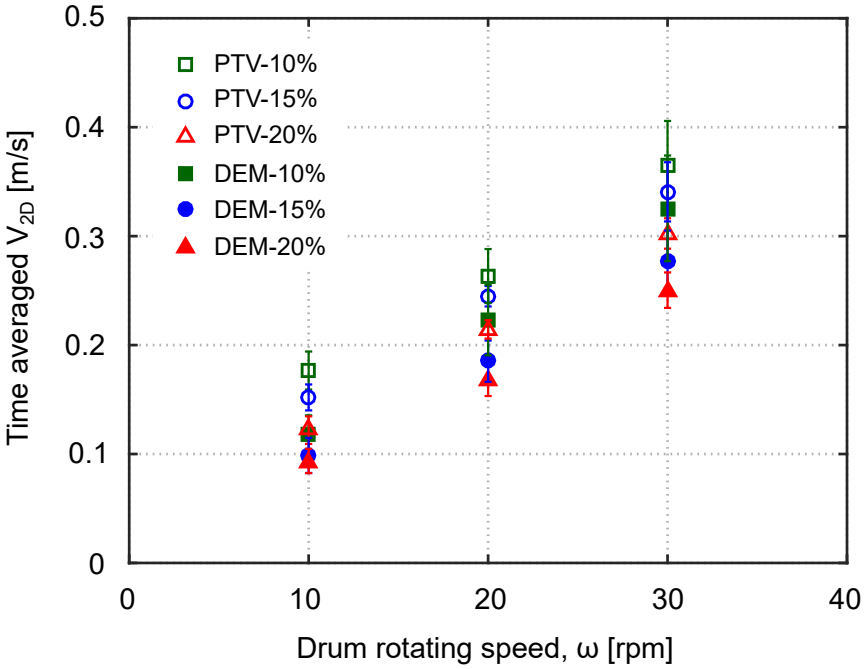

Figure 8.7: Time averaged velocity of all particles in the drum, measured and predicted for a period of 3 s, at different filling degrees and various rotating speeds of the drum. Bed material: plastic balls.

As can be seen from the graph, the changes in time averaged velocity, $V_{2D}(T)$, clearly correlate with the drum rotating speed, even if the filling degree of the drum increases from 10 % to 20 %. This uniform change further indicates that the flights have a large impact on the motion of the particle system in FRD. As the comparison in Fig. 8.7 shows, the DEM predictions are slightly lower than the experimental results. But their data trends are similar.

8.2.5 Granular temperature of particle system

The granular temperature is a term used to quantify the random motion of particles about the mean velocity. In FRD, the fluctuations of granular temperature are caused by the motion of flights and the effect of the gravity. When a flight carries away particles with a velocity different from the average velocity of particles, the granular temperature increases due to the addition of particle kinetic energy. Besides, the granular temperature increases when particles in the dilute phase convert potential energy into kinetic energy. By ongoing particle-particle, particle-flight and particle-wall collisions, this kinetic energy is dissipated and the granular temperature gradually decreases until the next uptake or unloading motion of a flight.

The granular temperatures $\sqrt{\theta_{2D}}$, $\sqrt{\theta_x}$ and $\sqrt{\theta_y}$ of the particle system at time t are calculated as

$$\theta_{2D}(t) = \frac{1}{2}(\theta_x(t) + \theta_y(t)); \tag{8.6}$$

$$\theta_k(t) = \frac{1}{N_p}\sum_{i=1}^{N_p}(u_k(i,t) - u_k(t))^2, \quad k = x, y; \tag{8.7}$$

$$u_k(t) = \frac{1}{N_p}\sum_{i=1}^{N_p} u_k(i,t). \tag{8.8}$$

Where N_p is the total number of particles; $u_k(i,t)$ is component k of the instantaneous velocity of individual particle i at time t; $u_k(t)$ is the average velocity of all particles at time t in direction k.

Figure 8.8 depicts profiles of the square root of granular temperature $\sqrt{\theta_{2D}}$ over detection time obtained from PTV measurements and DEM predictions, including components in x and y directions. These results are for the case of drum operating with a filling degree of 10 % at rotating speeds of 10, 20 and 30 rpm.

As can be seen from the graphs, the values of the average square root of granular temperatures $\sqrt{\theta_{2D}}$, $\sqrt{\theta_x}$ and $\sqrt{\theta_y}$ periodically fluctuate with the measurement time. The fluctuating frequency is consistent with the motion period of one flight, which is one quarter of the drum rotation period. As expected, the square roots of granular temperatures increase on average as the drum rotating speed increases. It is clear that the particle motion is more intensive because more energy is introduced when the drum rotates at a

higher speed.

As can be seen from sub-figures (a), (b) and (c), the granular temperature component $\sqrt{\theta_y}$ is always higher than $\sqrt{\theta_x}$ and $\sqrt{\theta_{2D}}$. This illustrates that the fluctuation of particle velocities is markedly stronger in the vertical direction than in the horizontal direction, which is caused by the gravity. Moreover, the difference between $\sqrt{\theta_y}$ and $\sqrt{\theta_x}$ increases when the drum rotating speed increases, indicating that the rotating speed of the drum has a big effect on the dilute phase.

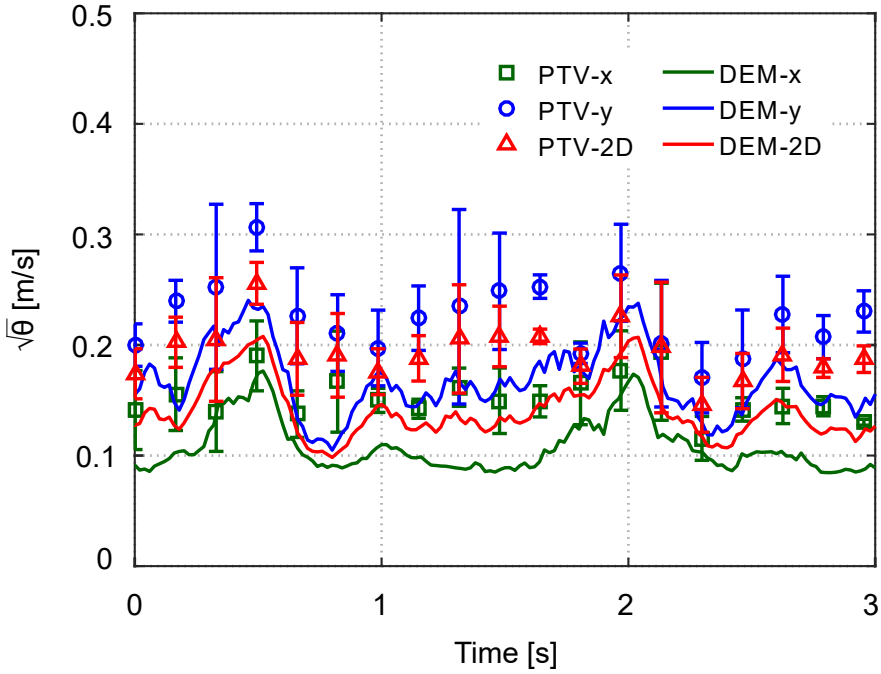

(a)

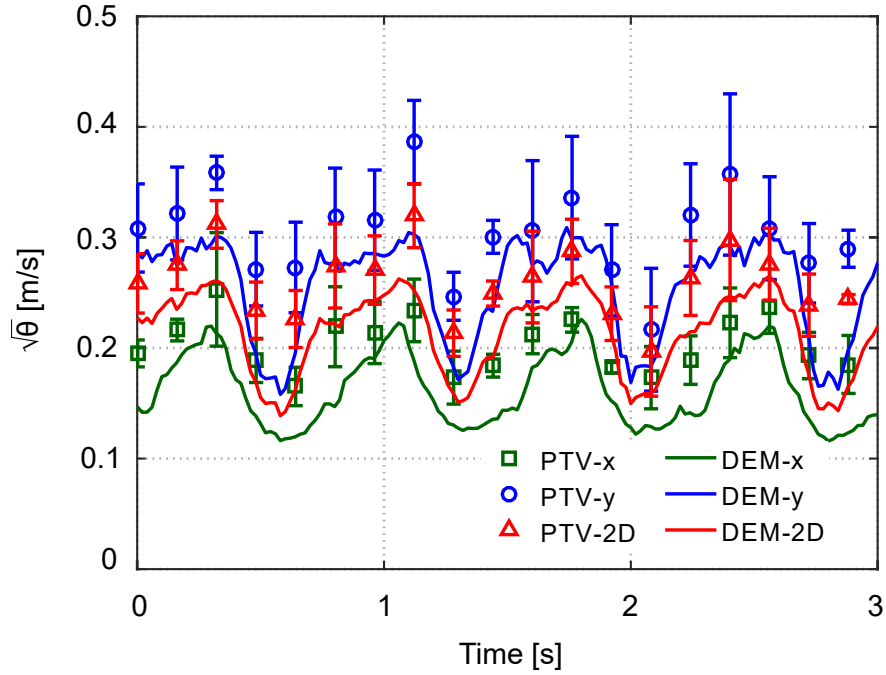

(b)

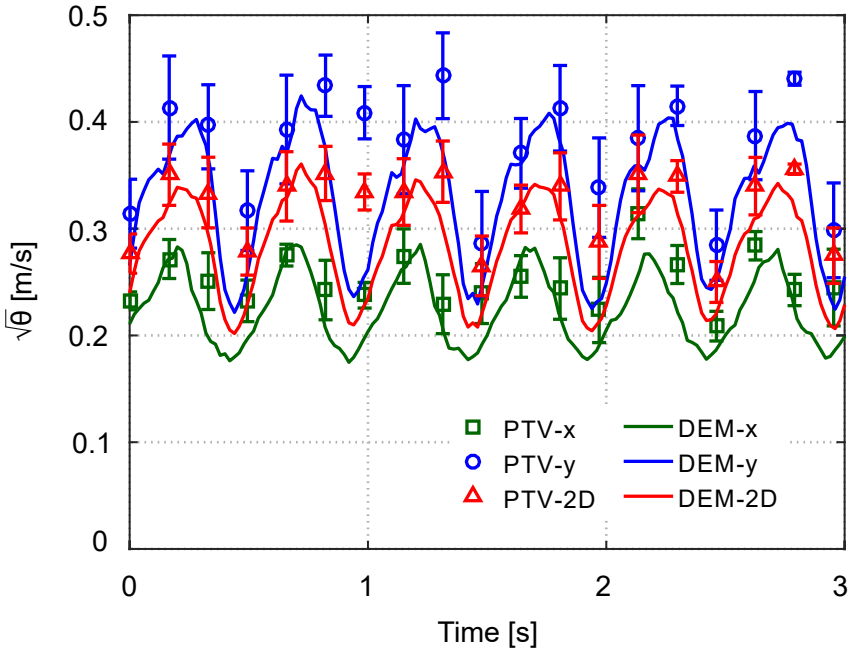

(c)

Figure 8.8: The square root of granular temperatures of all particles as a function of time using a 10 % filling degree, together with components in x and y direction. Rotating speeds of (a) 10 rpm, (b) 20 rpm, (c) 30 rpm. Bed material: plastic balls. $t = 0$ at $\delta = 0°$.

Furthermore, the impact of the filling degree on the particle system is studied. Figure 8.9 shows the square root of granular temperatures $\sqrt{\theta_{2D}}$, $\sqrt{\theta_x}$ and $\sqrt{\theta_y}$ in dependence on measurement time, depicted for the drum operating at 30 rpm with various filling degrees of 10 %, 15 % and 20 %.

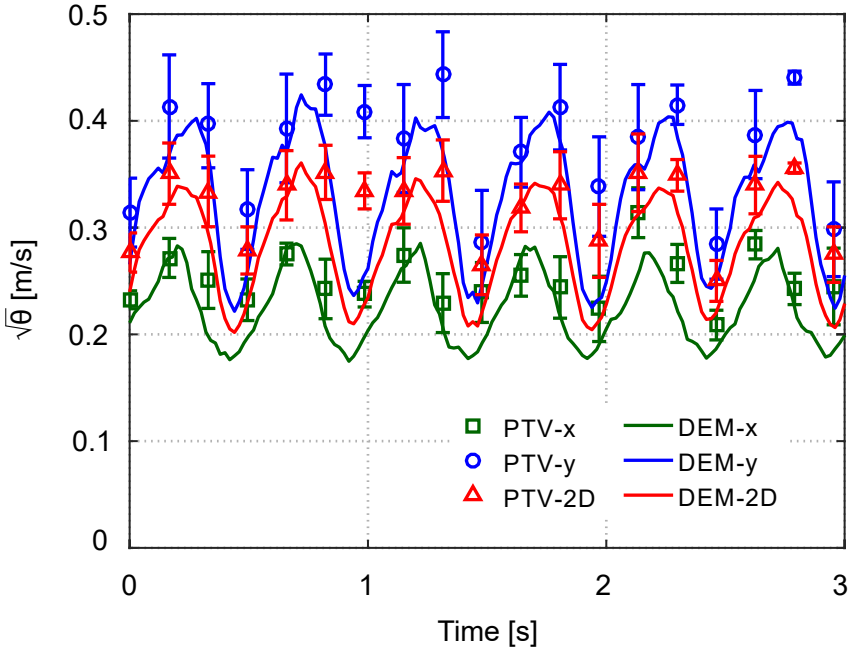

(a)

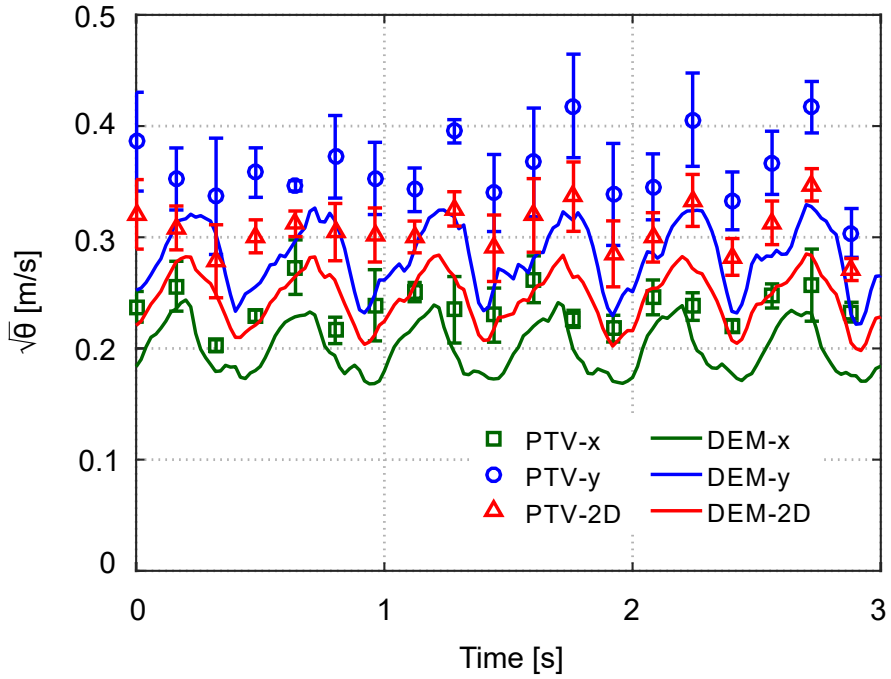

(b)

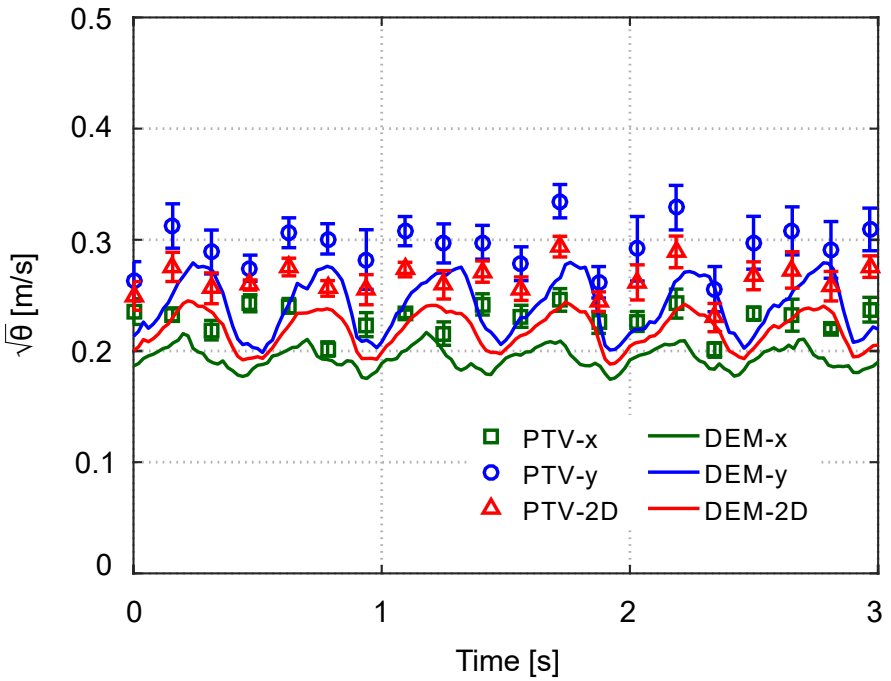

(c)

Figure 8.9: The square root of granular temperatures of all particles as a function of time at 30 rpm, together with components in x and y direction. Filling degrees of (a) 10 %, (b) 15 %, (c) 20 %. Bed material: plastic balls. $t = 0$ at $\delta = 0°$.

For those three filling degrees, the square root of granular temperatures fluctuate with the same frequency but different amplitudes. As the drum filling degree increases, the

square roots of granular temperatures $\sqrt{\theta_x}$, $\sqrt{\theta_y}$ and $\sqrt{\theta_{2D}}$ decrease significantly. This is due to the fact that, as the filling degree increases from 10 % to 20 %, a larger portion of the drum cross-section is occupied by the bed phase at the bottom of the drum. Thereby, the particle ratios of flight phase and dilute phase decrease accordingly. In addition, the particle-wall and particle-flight collisions reduce as the bed phase increases.

Similar to the particle average velocity, the time-averaged granular temperature is evaluated for different rotating speeds and filling degrees for a duration time of 3 s. The time-averaged square root of the granular temperature is calculated as

$$\sqrt{\theta_{2D}(T)} = \frac{1}{N_t} \sum_{t=1}^{N_t} \sqrt{\theta_{2D}(t)}. \tag{8.9}$$

As depicted in Fig. 8.10, the time-averaged square root of the granular temperature $\sqrt{\theta_{2D}}$ increases for each of the three drum filling degrees as the rotating speed increases, according to both the PTV measurements and the DEM predictions. Meanwhile, the time-averaged square root of granular temperature decreases for all rotating speeds when the drum filling degree increases. With a similar trend, the values calculated from the DEM model are a little lower than the PTV experimental results.

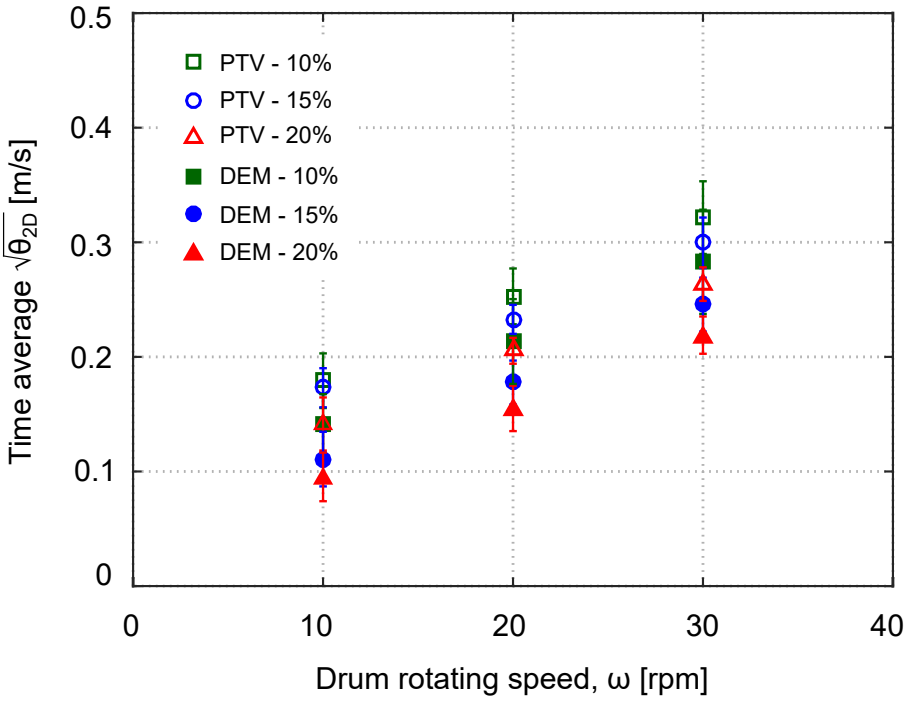

Figure 8.10: Time-averaged square root of granular temperature in the drum, measured and predicted for a period of 3 s, at different filling degrees and various rotating speeds of the drum. Bed material: plastic balls.

Chapter 9

Influence of the number of flights on particle motion

This chapter is based on Zhang et al. [103].

9.1 The number of flights

The aim of this chapter is to study the influence of the number of flights on the particle moving characteristics in the three particle phases. Plastic balls are used as the bed material in the FRD. The drums with different flight numbers of 1, 4, 8 and 12 are filled to 15 % and operated at five different rotating speeds (10 - 30 rpm). The experimental setup has been described in detail in Chapter 5.

By using the PTV method, the holdup ratio and discharging rate of single flight and active flights, particle falling time, and the particle ratio of the dilute phase can be investigated from a series of experimental images. These parameters can also be calculated from previous models (Lee & Sheehan model and Sunkara et al. model). In addition, a series of DEM simulations are performed to predict the movement of particles in the drums with different numbers of flights. A comparison between the PTV measurements, model calculations, and the DEM simulations is presented to study the particle dynamics in the cross-section of the FRD.

9.2 Results and discussion

9.2.1 Holdup ratio of single flight

The angle position of the flight tip at 9 o'clock ($\delta = 0°$) separates the whole drum chamber into two parts: the upper half of the drum and the lower part of the drum. It

is usual to classify the loading status of the drum by comparing this angle to the first discharge angle [1, 3, 5]. Since particles that discharge from the flights below this angle have very limited time to contact the gas, the loading and unloading behavior of the flights is estimated from the 0° discharge angle in this work.

The flight holdup ratio measured in the drum with just one flight (mass of particles in the flight to total mass of particles in the drum) is compared with the calculations from the Lee & Sheehan model (Eqs. 2.6 in Table 2.1) and the Sunkara et al. model (Eqs. 2.7 in Table 2.1). Figure 9.1 shows the dependency of the holdup ratio of single flight on the discharge angle at drum rotating speeds of 10 rpm and 30 rpm. Symbols in the figure represent the PTV measurement results, the lines represent the model calculations. Error bars indicate the standard deviations of the repeated data.

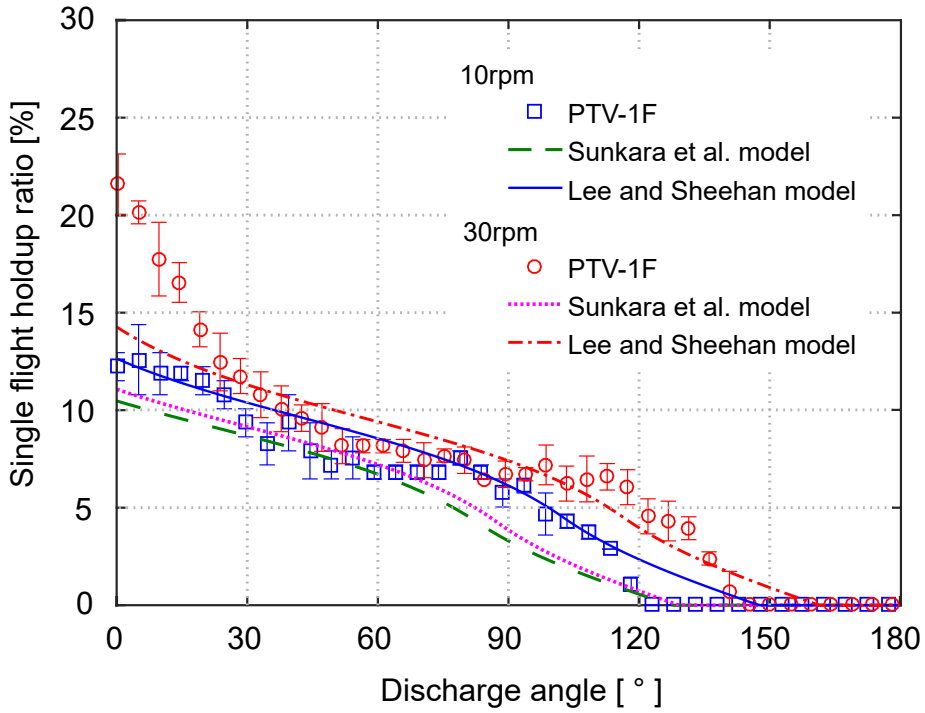

Figure 9.1: Single flight holdup ratio obtained from PTV measurements and model calculations as a function of the discharge angle. The drum with one flight is filled to 15 % and operated 10 rpm and 30 rpm. Bed material: plastic balls.

Compared with experimental data, the model of Sunkara et al. clearly underestimates the holdup ratio of the single flight, especially at the higher drum rotating speed of 30 rpm. As mentioned in Section 2.1.2, the kinetic angle of repose in the model of Sunkara et al. is calculated from the model of Schofield and Glikin [25]. However, this model does not take into account the inertial force acting in the cascading layer at the flight surface, resulting in too small values [26]. In case of the Lee and Sheehan model, the predictions of holdup ratio alternate between overestimation and underestimation. This model shows more gradual and uniform changes than the measured data. This is due to the kinetic

angle of repose γ in this model, which is the mean surface angle and averaged from the measured kinetic angle of repose over the whole unloading process.

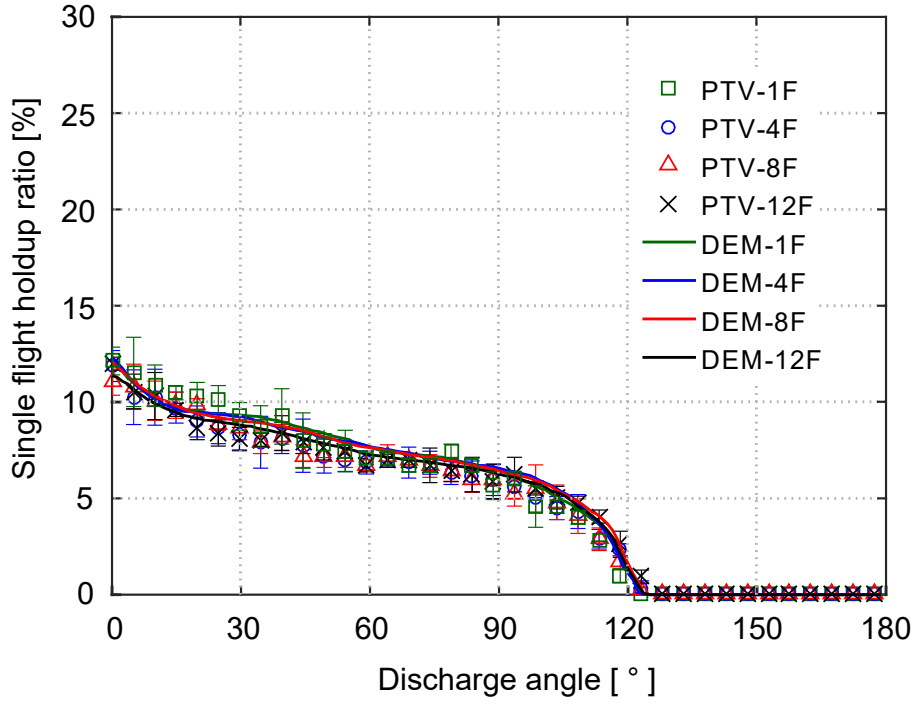

(a)

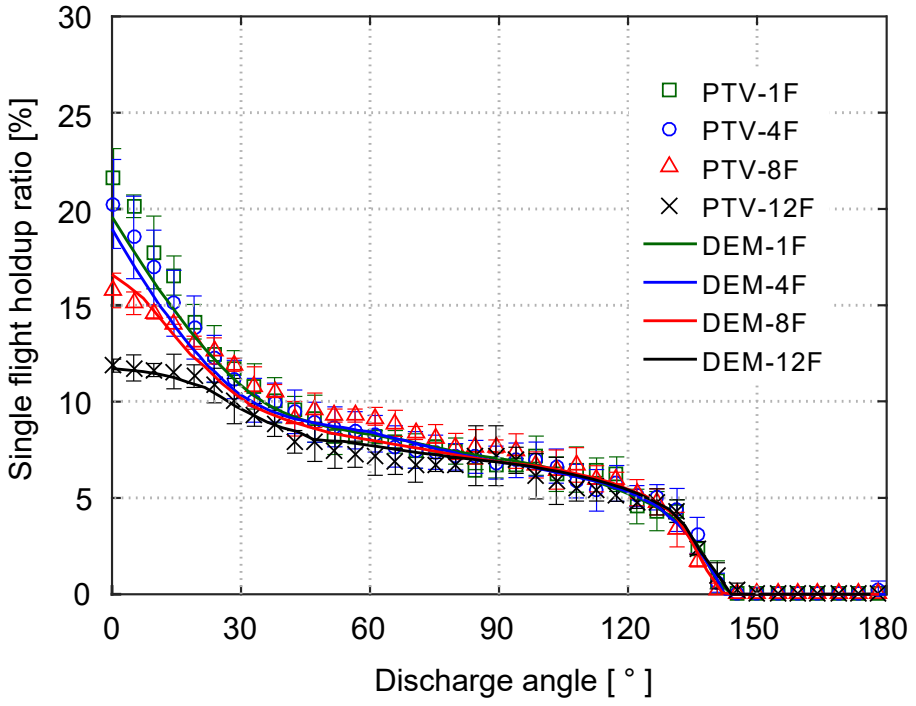

(b)

Figure 9.2: Single flight holdup ratio as a function of the discharge angle. The drum with different number of flights is filled to 15 % and operated at: (a) 10 rpm, and (b) 30 rpm. Bed material: plastic balls.

Next, results from PTV measurements and DEM simulations have been evaluated to study the influence of the number of flights on the single flight holdup ratio. The drum operated at 10 rpm shows very similar results of single flight holdup ratio when 1, 4, 8 or 12 flights are installed (Fig. 9.2 (a)). When the drum rotating speed is changed from 10 rpm to 30 rpm, different results are obtained, as shown in Fig. 9.2 (b). Although an enhancement of the flight holdup ratio of single flight is observed for all the cases, the drums with less flights (1, 4 or 8) display a larger increment. This can be explained by the fact that the angular space between two adjacent flights decreases with increasing the number of flights in the drums. When this space becomes insufficient, the kinetic angle of repose on the flight is smaller than the original value, thereby resulting in lower flight holdup.

It should also be noticed that increasing drum rotating speed could expand the range of flight loading. As observed by Silbert et al. [123] and Lee and Sheehan [35], the kinetic angle of repose and the final discharge angle of a flight increase at higher drum rotating speed. According to the PTV results, the final discharge angles are 124.8°, 131.4°, 134.4°, 139.5° and 144° for the drum operated at 10, 15, 20, 25 and 30 rpm, respectively. Good agreement between the experimental data and the DEM predictions illustrates that the DEM can capture the particle ratio of flight phase accurately and better than previous models from literature.

9.2.2 Cascading rate of single flight

Flight cascading rate is investigated by calculating the change of particle mass on the flight in Chapter 9. The cascading rate of just one flight from measurements is compared with the predictions of the Lee & Sheehan model and the Sunkara et al. model. Figure 9.3 shows the single flight cascading rate as a function of the discharge angle for two rotating speeds of 10 rpm and 30 rpm.

For the PTV measurements, a large cascading rate of the single flight is observed at the beginning, then it gradually decreases to a minimum and remains stable until the flight passes its highest position (12 o'clock position). After that, the curves increase quickly to a maximum, and then decrease sharply to zero (empty flight). When the drum rotating speed increases from 10 rpm to 30 rpm, the cascading rate increases significantly in the early and last discharge periods.

Calculated cascading rates of the two models are quite different from the PTV measurements. Although the Lee and Sheehan model shows better performance than the Sunkara et al. model, the relatively flat curves of the cascading rates in both models do not reflect the unloading characteristics of the flight. This is might be due to the assumption in both models that the solids are free-flowing and flow continuously over the flight tip. However, the deviations between model predictions and the measured data indicate that the unloading of the flight occurs discontinuously, which is in accordance

with observations of Revol et al. [30] and Lee and Sheehan [35] in FRD studies.

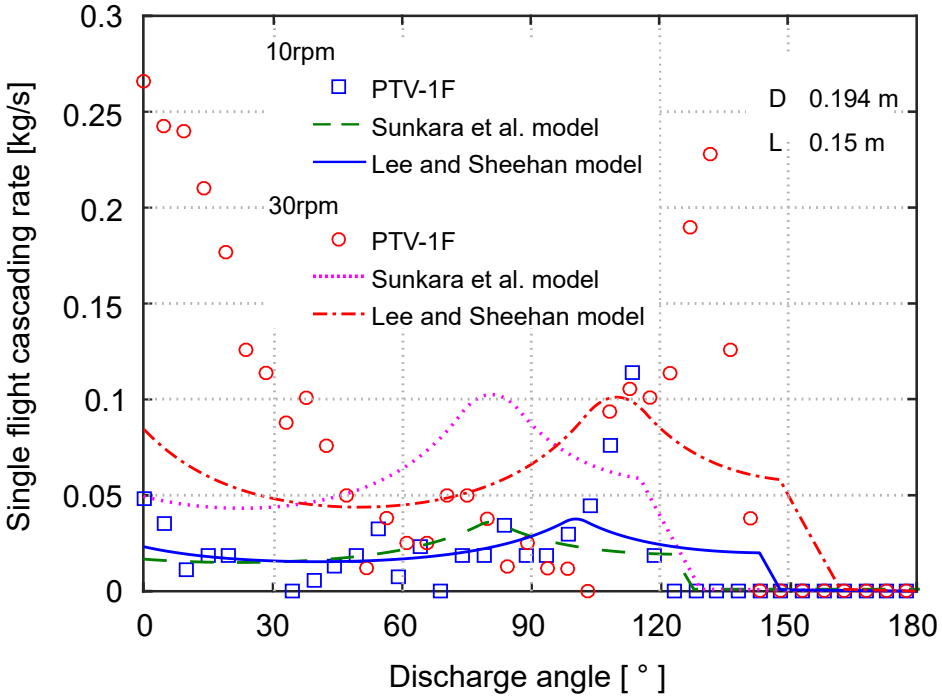

Figure 9.3: Single flight cascading rate obtained from PTV measurements and previous model predictions as a function of the discharge angle. The drum with one flight is filled to 15 % and operated 10 rpm and 30 rpm. Bed material: plastic balls.

Figure 9.4 (a) compares PTV measurements and DEM simulations in terms of the cascading rate of a single flight for drums with different numbers of flights operated at 10 rpm. Results indicate that the number of flights has no significant influence on the cascading rate of a single flight when the drum is rotated at low speed. For the drum operated at 30 rpm, Figure 9.4 (b) shows that the cascading rate of the single flight increases significantly as the drum rotating speed increases. Comparing the cases with different number of flights at 30 rpm, the lowest cascading rate in the initial period is observed when the drum contains 12 flights. This illustrates that the cascading rate of the single flight is greater at the initial charging period for a drum with 1 and 4 flights than for a drum with 8 and 12 flights at high drum rotating speed.

There is a small deviation between the experimental results and the DEM simulation results. This can be explained as follows: On the one hand, the unloading of solids from the flight is discontinuous, in a series of avalanches. On the other hand, in PTV measurements, large gaps between particles may be filled by particles from the background layer, which changes the observable solids holdup of the flight. Nevertheless, the DEM simulations agree better with the experimental results than the literature models.

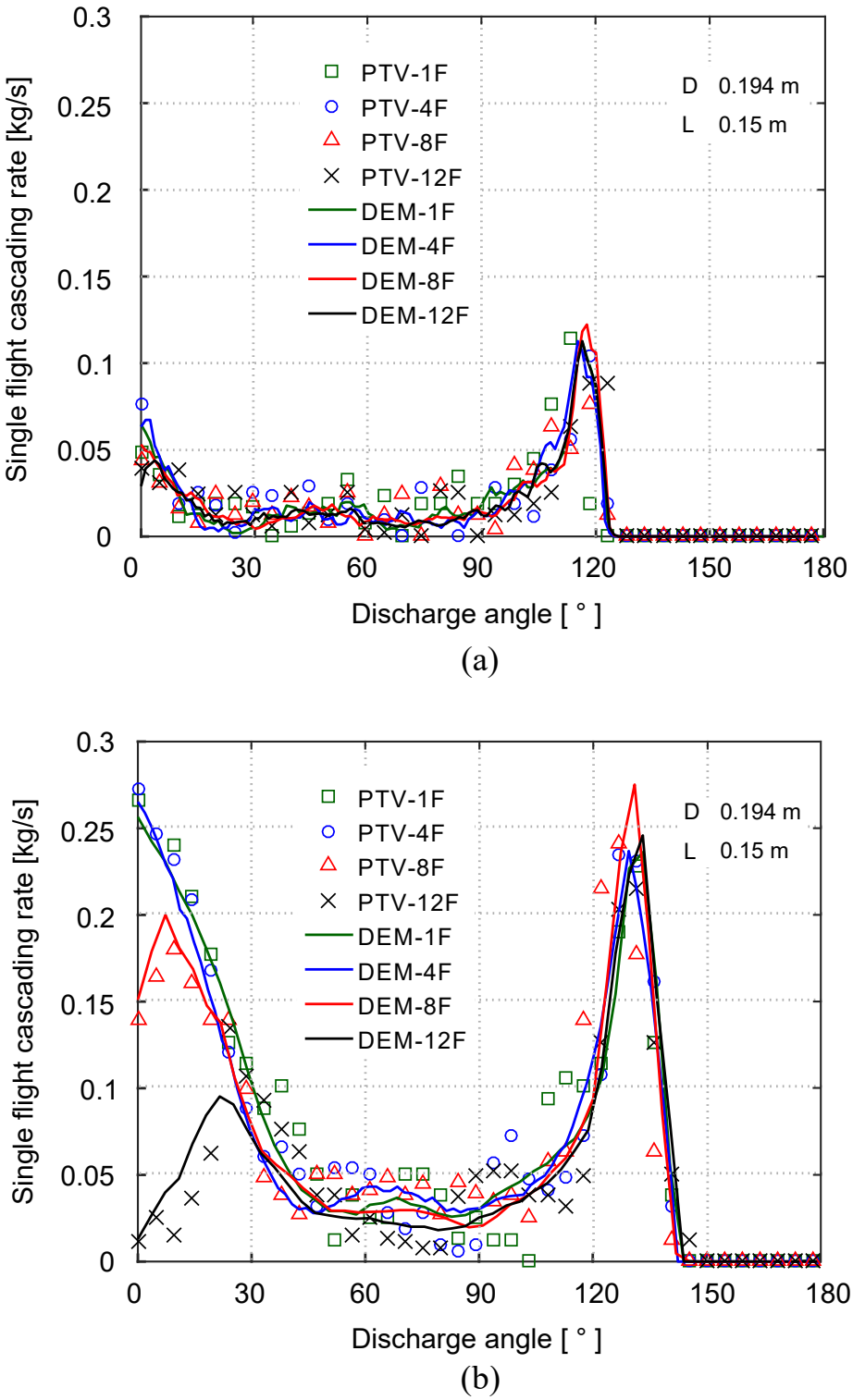

Figure 9.4: Single flight cascading rate as a function of the discharge angle. Drum with different number of flights is filled to 15 % and operated at: (a) 10 rpm, and (b) 30 rpm. Bed material: plastic balls.

9.2.3 Holdup ratio of active flights

In the study of the FRD, all flights in the upper half of the drum ($\delta > 0$) are called active flights. The effect of the number of flights on the solids holdup of active flights is also investigated. The variation of solids holdup ratio at 10 rpm is plotted as a function of the angle of drum rotation. The data from PTV measurements, model calculations and DEM simulations for the drum with a different number of flights are plotted in Figs. 9.5 (a)-(d). The standard deviation obtained from repeated experiments is represented by bars in the plots.

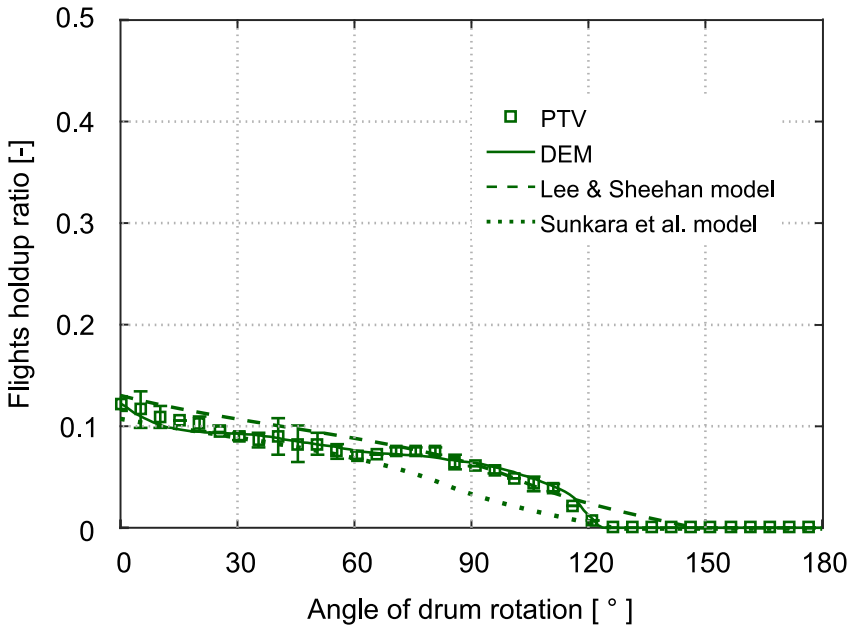

(a)

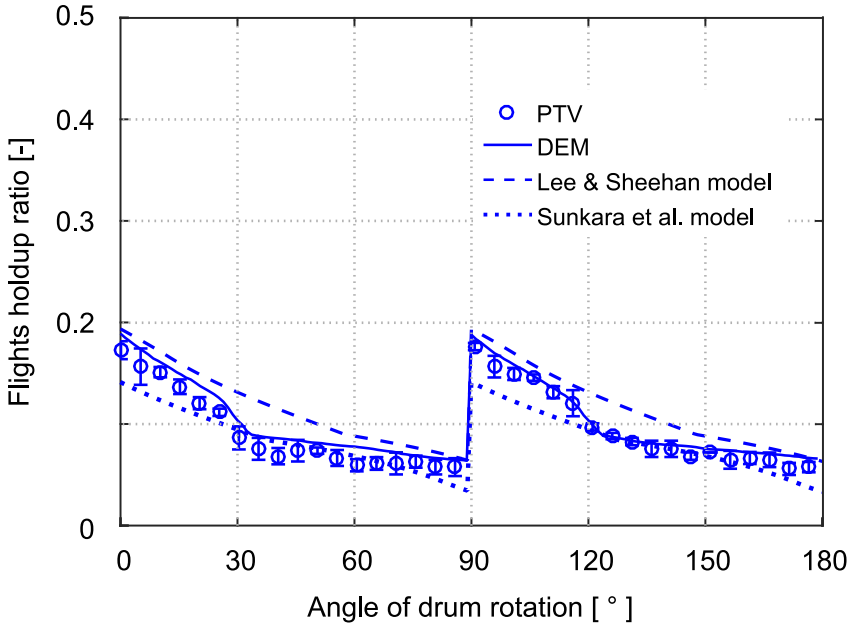

(b)

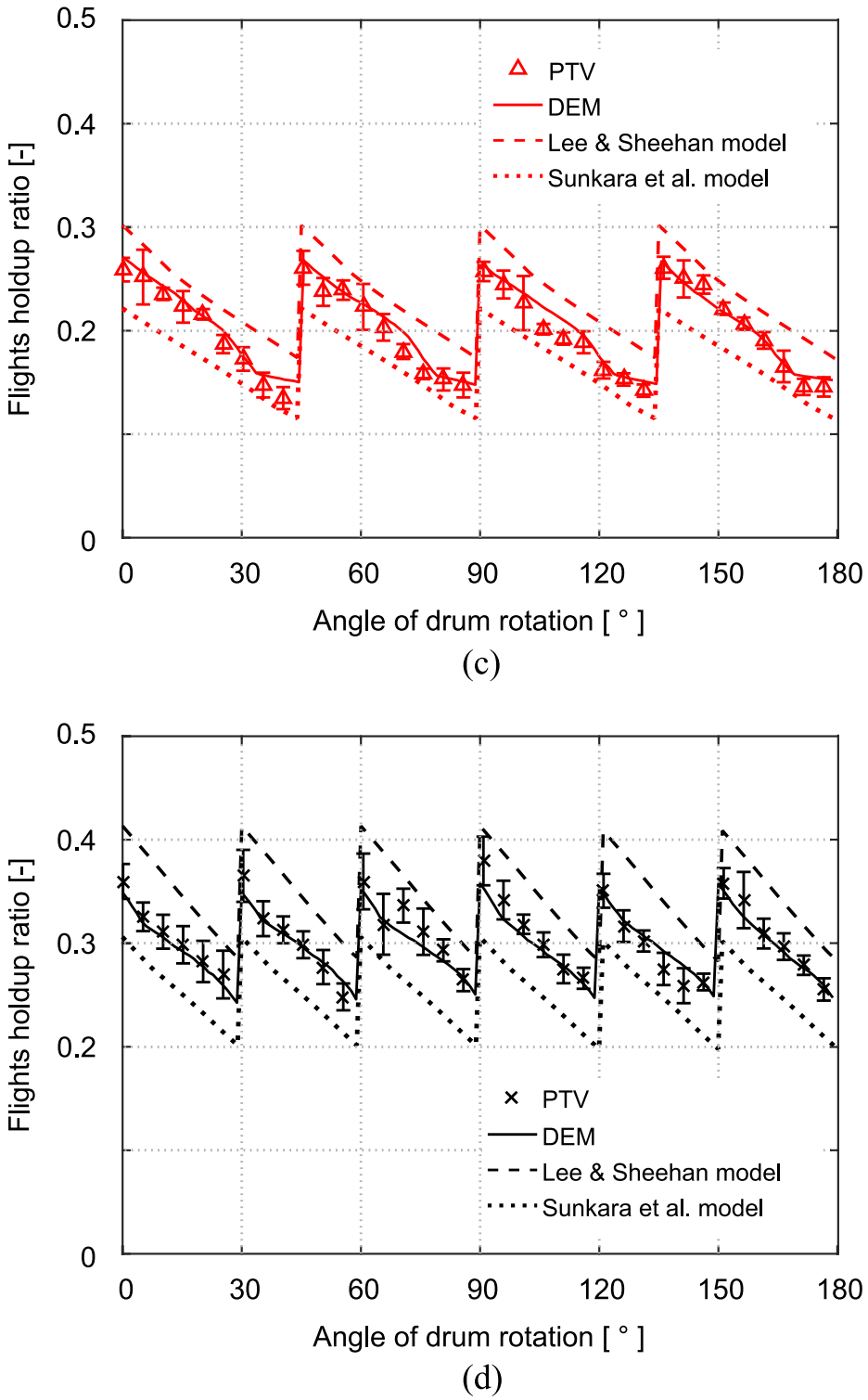

Figure 9.5: Active flights holdup ratio as a function of drum rotating angle. The drums, operated at 10 rpm with 15 % filling degree, are installed with different numbers of flights: (a) 1 flight, (b) 4 flights, (c) 8 flights, and (d) 12 flights. Bed material: plastic balls.

Generally, the holdup ratios of all active flights change periodically as the drum rotates. The frequency of periodic fluctuation is proportional to the number of flights, which leads

to periods of 360°, 90°, 45° and 30° for 1, 4, 8 and 12 flights, respectively. It should be mentioned that the rotating speed has an additional big impact on the frequency of the periodic fluctuations. As expected, larger holdup ratio of flights is obtained with more flights, and this advantage is maintained over the whole process. The maxima of solids holdup for the cases with 1, 4, 8 and 12 flights, according to the DEM results, are about 12.24 %, 18.82 %, 27.06 %, and 34.71 %, respectively. There is no linear relationship between the increment of the holdup ratio of active flights and the increment of flights number.

As can be seen from Figs. 9.5 (a)-(d), the models of Lee & Sheehan and Sunkara et al. overestimate and underestimate the holdup ratio of active flights, respectively. There is a greater deviation when the drum has more flights, which comes from the superposition of deviations in the holdup ratios of single flight. The data from DEM simulations is in good agreement with the experimental measurements and thus DEM data is used for further analysis.

To quantitatively analyze the effect of the number of flights, the averaged holdup ratio of active flights within one rotation cycle of the drum $\overline{f}_F$ is calculated as

$$\overline{f}_F = \frac{1}{N} \sum_{i=1}^{N} f_F(i), \tag{9.1}$$

where N is the total number of time steps in a rotation cycle of the drum.

For drums with a different number of flights and rotated at various speeds, the corresponding results from PTV measurements and DEM simulations are plotted in Fig. 9.6. The bars in the histograms represent the standard deviation of holdup in the flights over one rotation cycle. For a drum rotated at 10 rpm, 15 rpm, 20 rpm, 25 rpm, and 30 rpm, the time periods of one rotation circle are 6 s, 4 s, 3 s, 2.4 s, and 2 s, respectively.

Figure 9.6 (a) shows a slight increase in the averaged solids holdup of the flight for the drum with one flight when changing the drum speed from 10 to 30 rpm. This phenomenon also appears in Figs. 9.6 (b)-(d) when the number of flights changes to 4, 8 or 12, because the high speed results in a larger kinetic angle of repose. Moreover, the spread in holdup ratio of flights during one rotation cycle of the drum slightly increases when the number of flights increases from 1 to 4. As the number of flights continues to increase to 4 and 8, the range of holdup ratio of flights is reduced. The overall performance indicates that a high number of flights produces a more stable amount of solids in those flights, thereby a more uniform solids distribution in the cross-section of the drum is obtained. Comparing the plots in Fig. 9.6 (a) to (d), the number of flights has a stronger influence on flight holdup than the drum rotating speed.

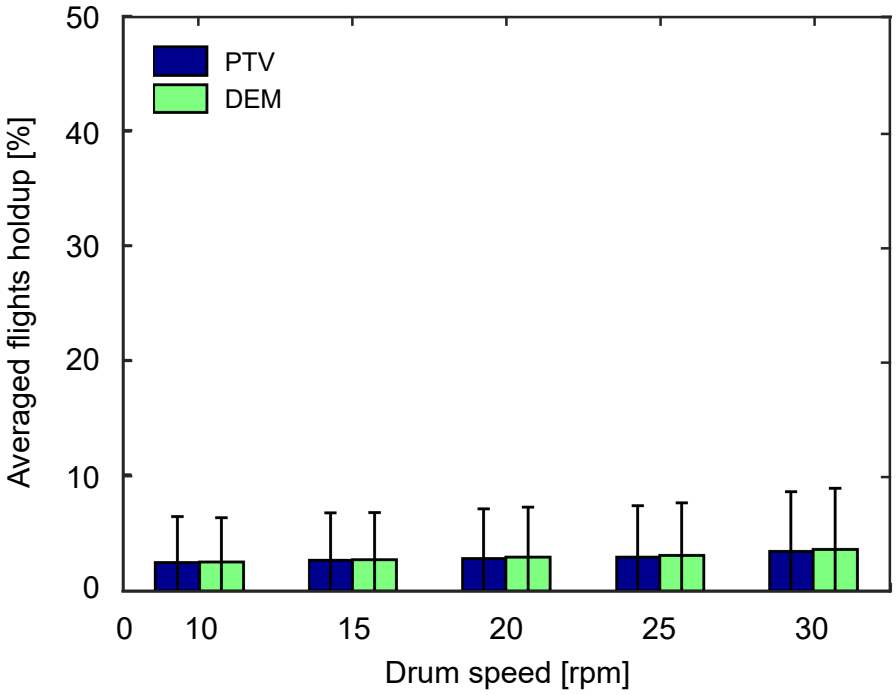
PTV
DEM
Averaged flights holdup [%]
0
10
20
30
40
50
0
10
15
20
25
30
Drum speed [rpm]

(a)

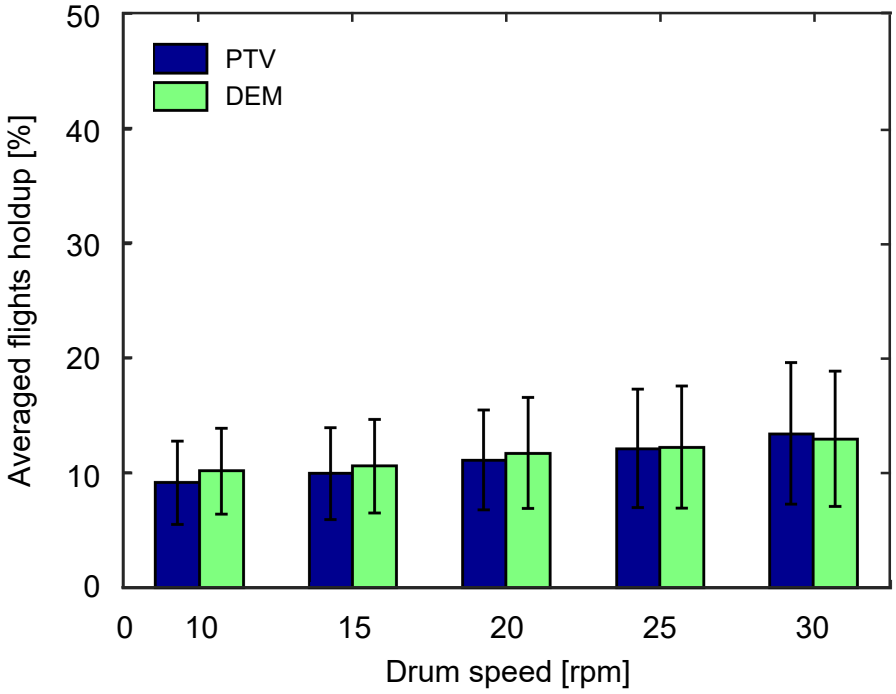
PTV
DEM
Averaged flights holdup [%]
0
10
20
30
40
50
0
10
15
20
25
30
Drum speed [rpm]

(b)

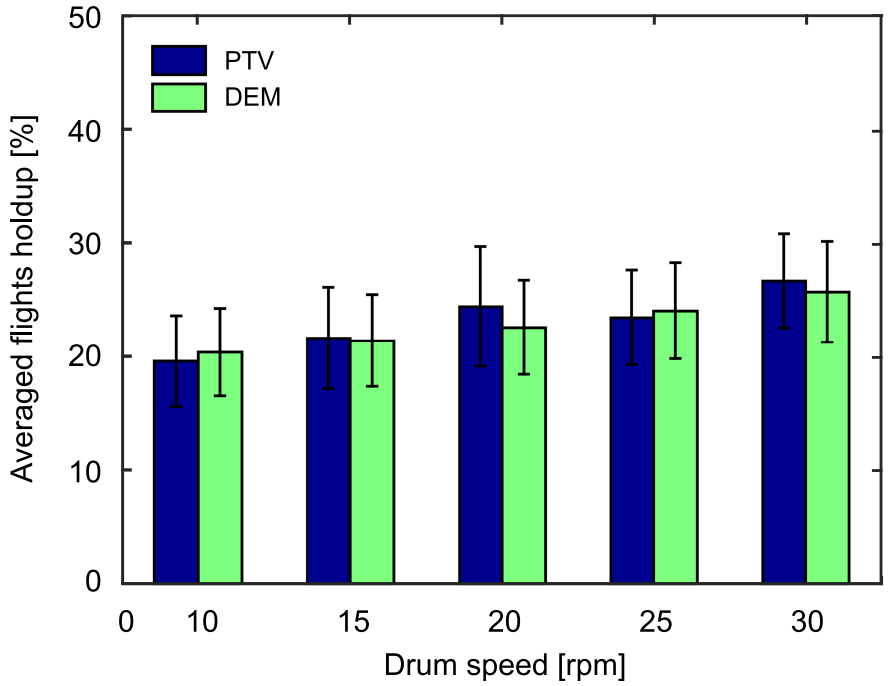

(c)

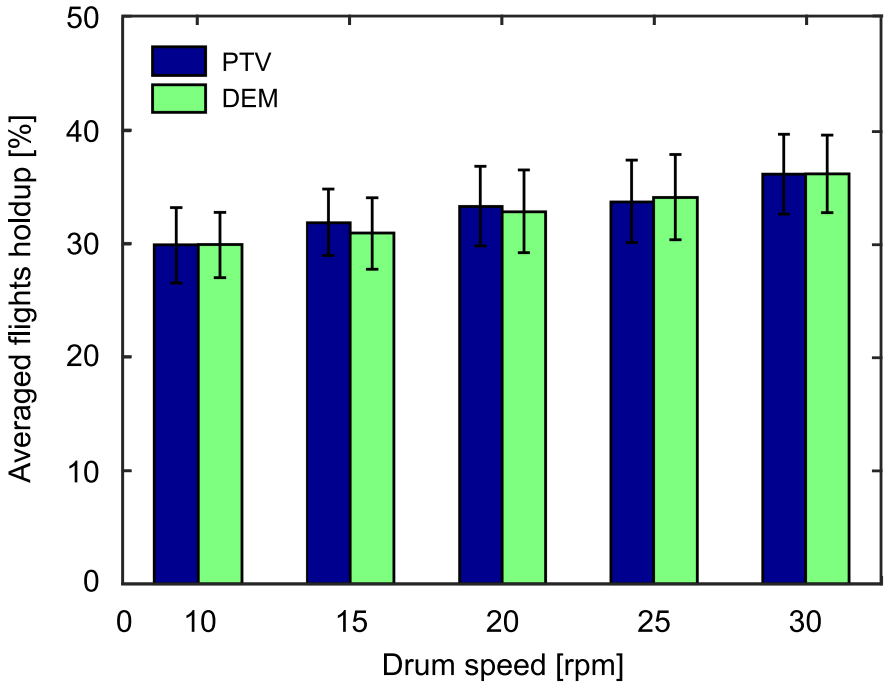

(d)

Figure 9.6: Averaged flights holdup as a function of drum speed. The drum is filled at 15 % level and operated at various rotational speeds, with different flights numbers: (a) 1 flight, (b) 4 flights, (c) 8 flights, (d) 12 flights. Bed material: plastic balls.

9.2.4 Cascading rate of active flights

The variation of the cascading rate of active flights with the number of flights obtained from PTV measurements, DEM simulations and model calculations, is shown in Fig. 9.7 for a rotation speed of 10 rpm. All curves fluctuate periodically as the drum rotates, and the frequency is the same as the frequency of the corresponding holdup ratio of flights in Fig. 9.5.

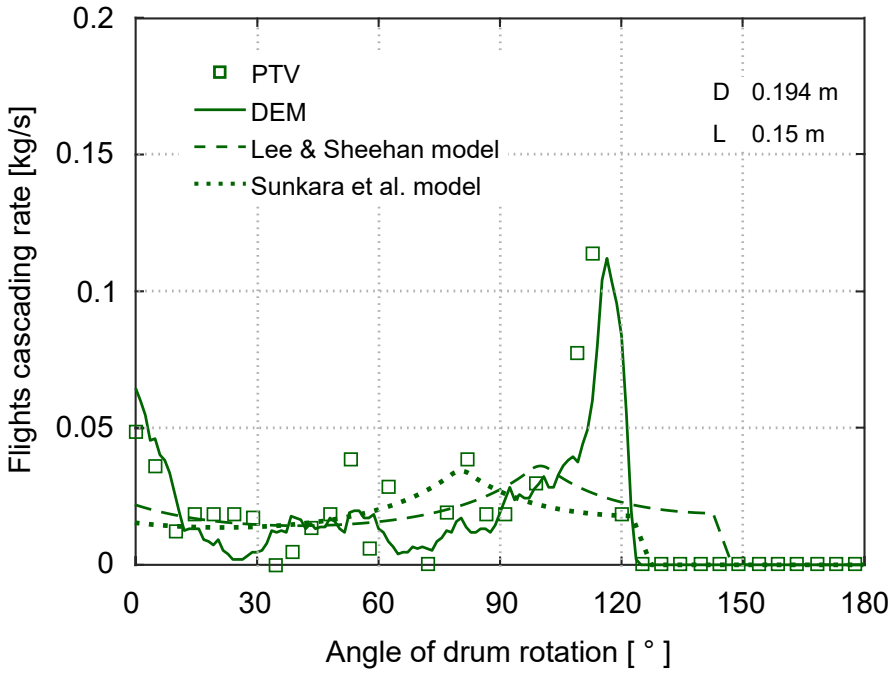

(a)

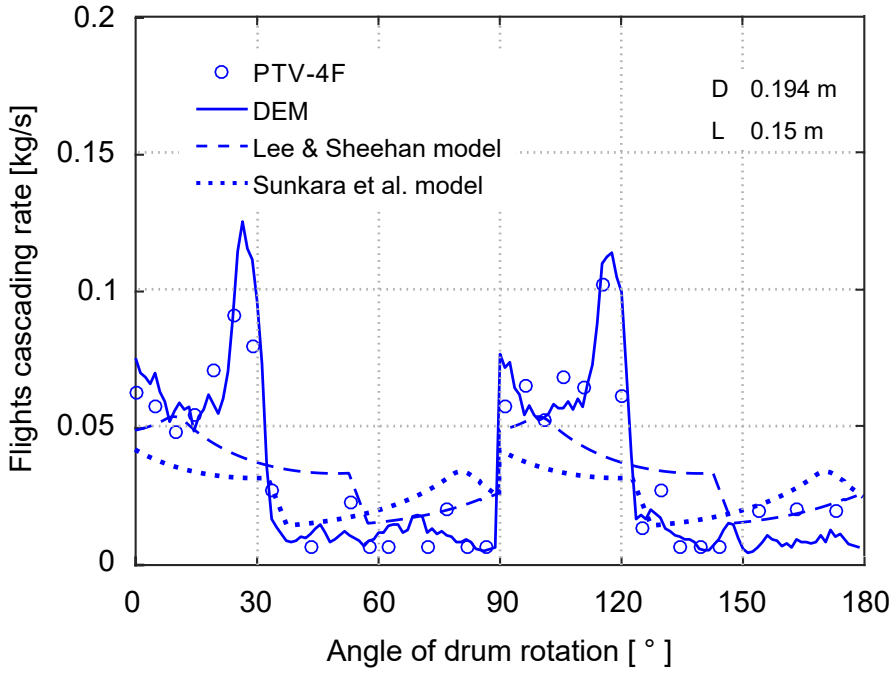

(b)

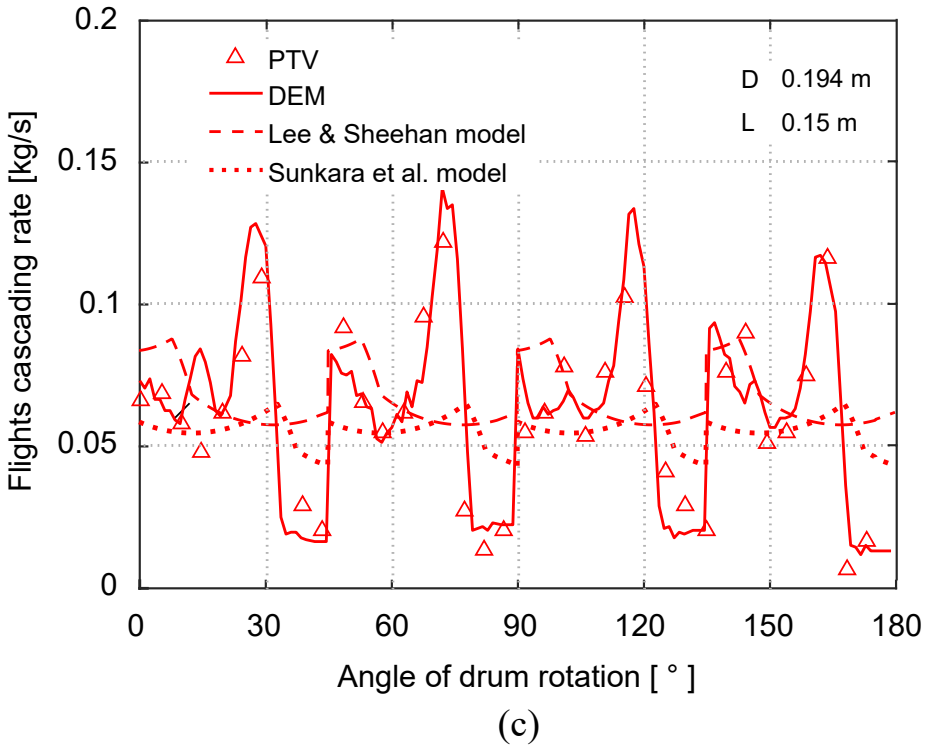

(c)

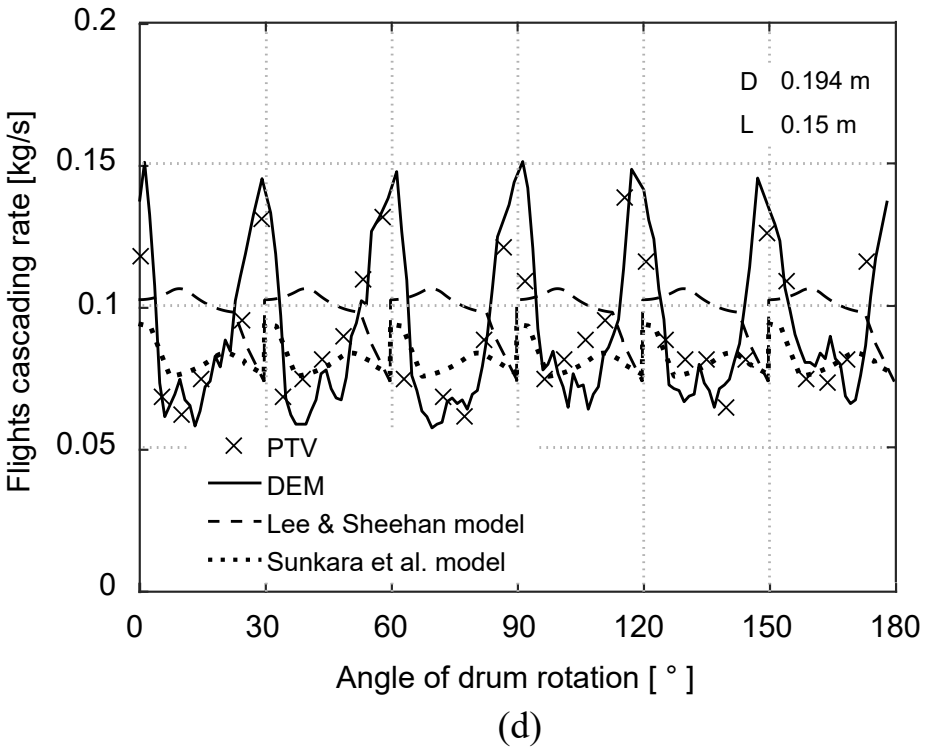

(d)

Figure 9.7: Cascading rate of flights as a function of the angle of drum rotation. The drums, operated at 10 rpm with 15 % filling degree, are installed with different number of flights: (a) 1 flight, (b) 4 flights, (c) 8 flights, and (d) 12 flights. Bed material: plastic balls.

The PTV and DEM profiles of cascading rate in a single cycle are roughly the same. There are some fluctuations in the PTV and DEM data which may result from the discontinuous movement of solids, while the unloading profiles of the two literature models are quite different from the experimental results. Large deviations indicate that the discontinuous unloading of solids has a significant impact on the cascading rate of flights. It is necessary to consider the avalanche behavior of granular materials in the geometric models, especially for particle of large size. A better agreement between the geometric models and experimental results would be expected when the drum filled with small-sized particles. The largest cascading rate over the entire rotation cycle is observed for the case with 12 flights. Furthermore, the drum installed with 12 flights has a larger value of the minimum cascading rate than all other designs. It may be concluded that with more flights, the unloading behavior in the cross-section of the drum is more continuous and more stable.

Like in case of the holdup ratio of active flights, average values and the standard deviations of the cascading rate of flights in one rotation cycle of the drum have been calculated from PTV and DEM data for the different cases. As Fig. 9.8 illustrates, the averaged cascading rate shows a strong dependency on the number of flights and the drum rotating speed.

As seen from Fig. 9.8 (a) for the drum with one flight, the cascading rate increases with increase of drum rotating speed. This can also be observed in Figs. 9.8 (b)-(d) for drums with 4, 8 or 12 flights. Comparing the four plots in Fig. 9.8, a smaller spread of the cascading rate is observed as the number of flights increases. It can be concluded that a higher number of flights provides a larger and more stable discharging rate in the cross-section of the drum.

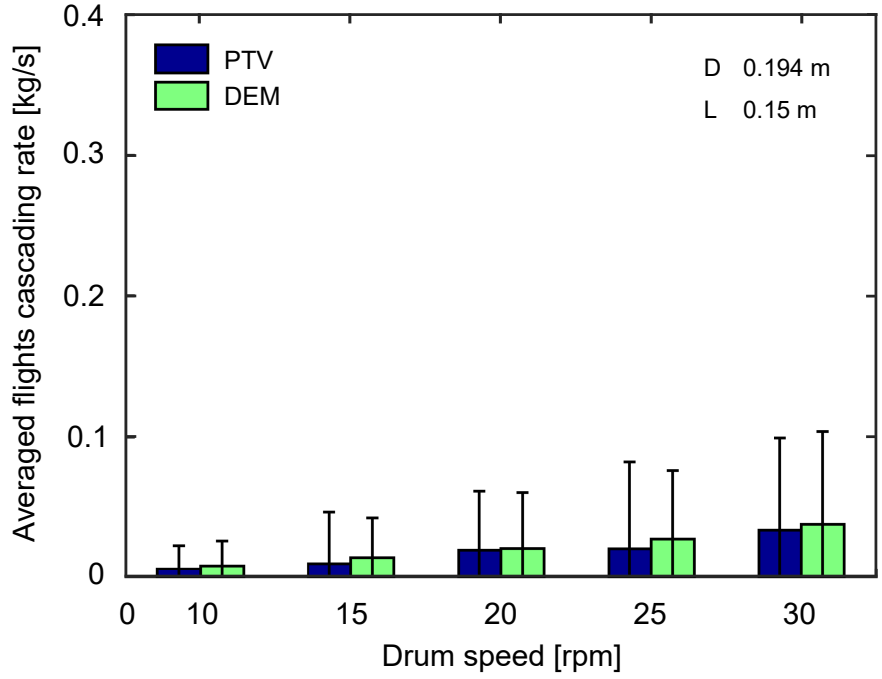
PTV
DEM
D 0.194 m
L 0.15 m
Averaged flights cascading rate [kg/s]
0.4
0.3
0.2
0.1
0
0
10
15
20
25
30
Drum speed [rpm]

(a)

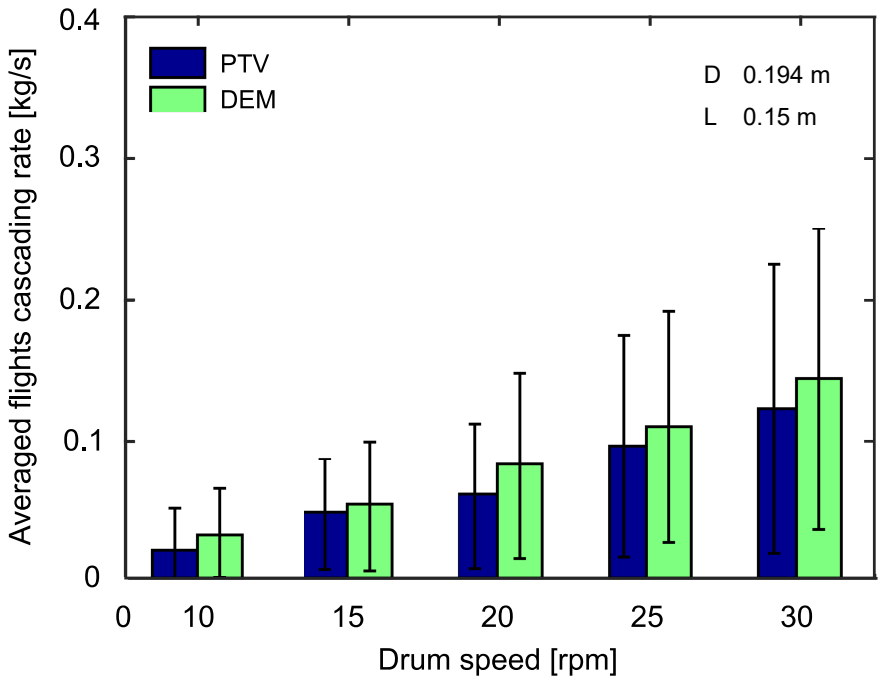
PTV
DEM
D 0.194 m
L 0.15 m
Averaged flights cascading rate [kg/s]
0.4
0.3
0.2
0.1
0
0
10
15
20
25
30
Drum speed [rpm]

(b)

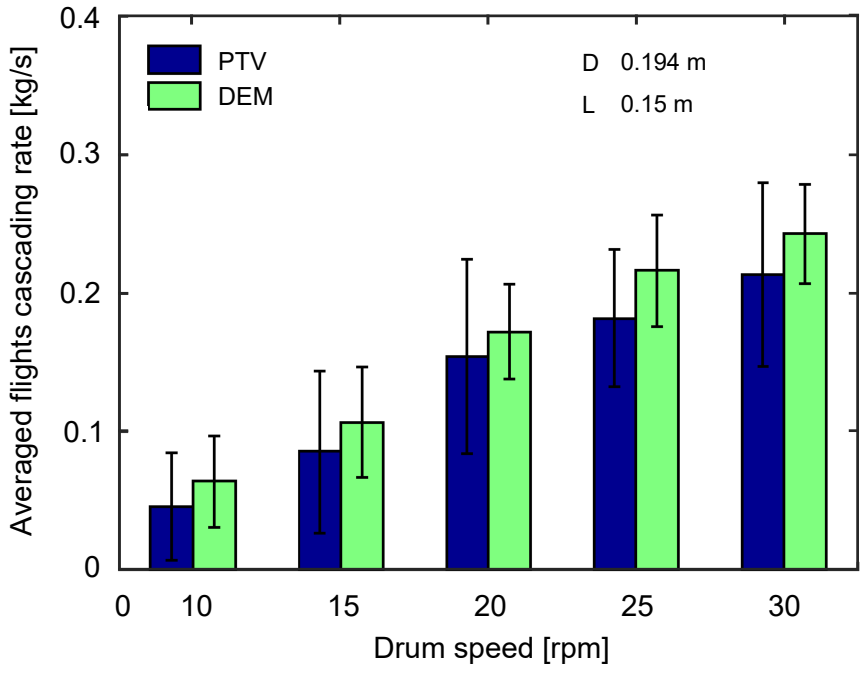

(c)

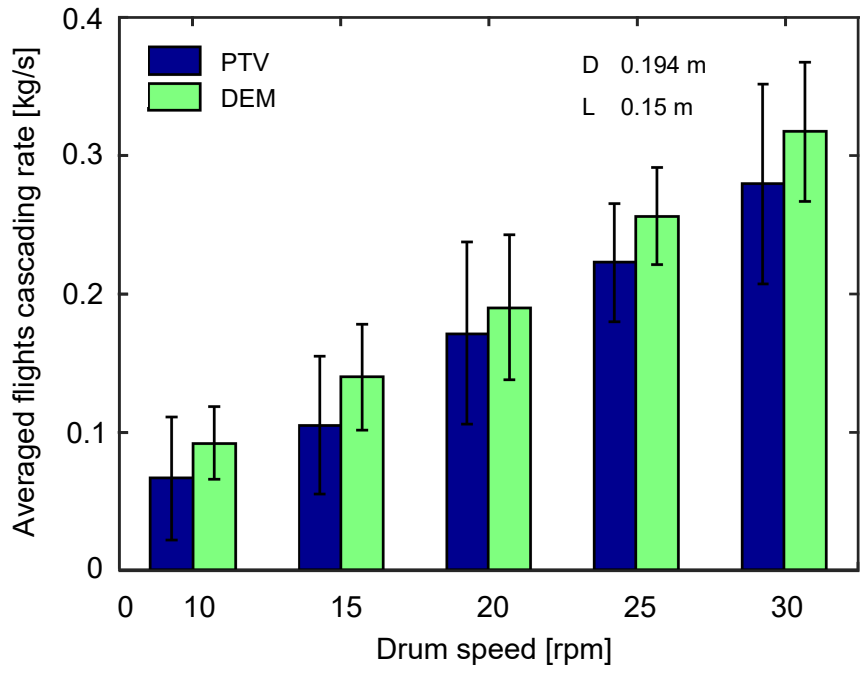

(d)

Figure 9.8: Averaged cascading rate of flights as a function of drum speed. The drum is operated with 15 % filling degree and with different number of flights: (a) 1 flight, (b) 4 flights, (c) 8 flights, and (d) 12 flights. Bed material: plastic balls.

9.2.5 Dilute phase ratio

The dilute phase consists of all particles which fall from the flights and is fully exposed to the gas. Such exposure is desired in order to enhance heat and mass transfer with the gas. Hence, the mass fraction of particles which belongs to the dilute phase (dilute phase ratio) directly affects the efficiency and performance of drums used, for example, to dry granular material. Combining the location and velocity of individual particles obtained from PTV measurements and DEM simulations, dilute phase identification can be realized. Figure 9.9 presents the variation of the particle fraction of the dilute phase during drum rotation, for drums with different number of flights. The bars on the symbols represent the standard deviation of the repeated PTV measurements.

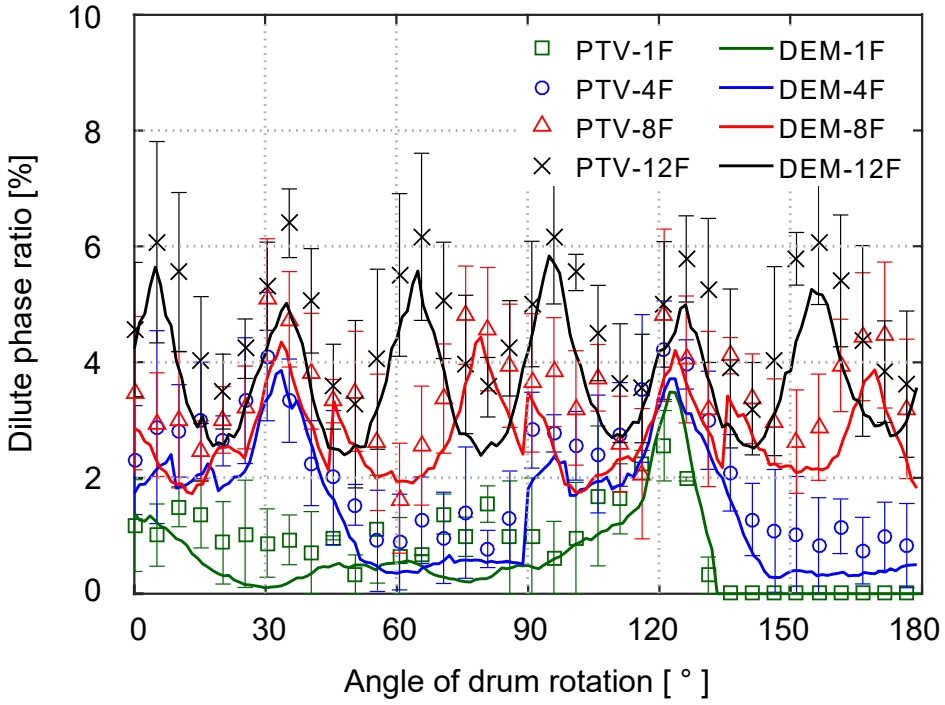

Figure 9.9: Dilute phase ratio as a function of the angle of drum rotation, obtained from PTV measurements and DEM simulations. The drums are installed with 1, 4, 8 and 12 flights and rotated at 10 rpm. Bed material: plastic balls. Filling degree 15 %.

In general, the curves fluctuate periodically with the corresponding frequency of the drum rotation. Increasing the number of flights can greatly improve the dilute phase ratio. At the same time, it also increases the frequency at which the maximum particle ratio of dilute phase occurs. It should be noted that a relatively large standard deviation is observed in the experimental results, especially for the drum with a high number of flights. The reasons are when the drum has more flights, more intense collisions occur

between falling particles and flights, or between rebound particles and other particles. This enhances the movement of particles in the axial direction. It also causes the particle number in the first layer of the drum, which is detected by the PTV method, to lose its representativeness of the cross-sectional particle distribution. Moreover, as the drum rotating speed increases, this effect becomes more serious. However, the results of 3D-DEM simulations do not have this problem as each particle is tracked and analyzed to reflect the dynamics of the particle system. Considering the good consistency of the DEM and PTV results in the previous studies, the subsequent analysis is performed by using the data from DEM simulations.

The average dilute phase ratio in one rotation cycle of the drum is calculated from the DEM data and compared with the predictions of the Sunkara et al. model (Eq. 2.15). The results for the drum with different number of flights and rotated at various speeds are shown in Fig. 9.10. The bars on the symbols represent again the standard deviation of the dilute phase ratio during one rotation cycle of the drum.

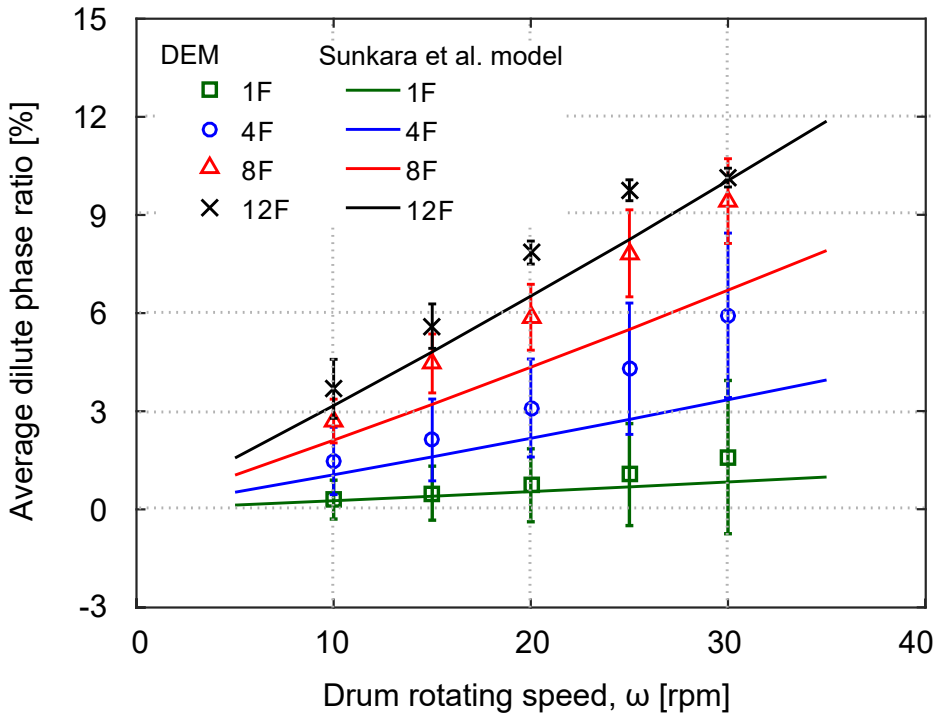

Figure 9.10: Averaged particle ratios of the dilute phase as a function of the drum rotating speed for the drums with 1, 4, 8 or 12 flights. The results are calculated from DEM simulations and the Sunkara et al. model. Bed material: plastic balls. Filling degree 15 %.

As can be seen, both the number of flights and the drum rotating speed show a positive effect on the fraction of particles that belong to the dilute phase. Compared with the DEM data, the model of Sunkara et al. underestimates the average particle ratio of the

dilute phase. The smaller flight holdup calculated from Eqs. 2.7 could be one reason. Moreover, the model ignores the phenomenon that some falling particles hit the rotating wall or flight and rebound into the dilute phase region.

At the same drum rotating speed, the portion of the dilute phase is larger for the drum installed with more flights. Looking into the details, there is a relatively small increment in the DEM data when the number of flights changes from 8 to 12. As presented before, the holdup ratio of a flight decreases when the increase in the number of flights results in a reduction in the angular distance between two adjacent flights.

For a fixed number of flights, the particle ratio of the dilute phase increases strongly with increasing drum rotating speed. Moreover, when the drum has 1 or 4 flights, the standard deviation of the particle ratio increases strongly as the drum rotating speed increases. While, a slower growth of the standard deviation is observed when the drum has 8 flights. When the number of flights increases to 12, the standard deviation is even smaller at high drum rotating speed. This illustrates that a constantly large number of particles are exposed to the gas for heat exchange when the drum has 12 flights.

It is worth noting that for the DEM results just a small increment is observed for the drum with 12 flights when changing the drum rotating speed from 25 rpm to 30 rpm. It may be caused by the 12 flights installed on the inner wall of the drum almost forming a closed circle. This makes particles which fall from a flight with some initial velocity to hit the adjacent flight shell and then bounce back into the air. Thereby, it increases the amount of particle in the gas. However, if the drum rotating speed is already high enough for all particles to hit an adjacent flight and rebound, further increasing the drum rotating speed will not increase the amount of particles in the dilute phase.

Chapter 10

Conclusions and outlook

10.1 Conclusions

The particle motion in FRD is quite complicated, as it is affected by many factors. An improved understanding of the motion behavior of the granular flow in FRD is crucial to improve the efficiency of particle drying and to achieve homogeneous product quality.

In the present work, the MPT technique was successfully utilized to track the particle motion in FRD for the first time. The movement of plastic balls and soybeans in an FRD has been investigated at various drum speeds. The results indicate that the particle translational and rotational velocities are strongly influenced by the drum rotating speed. The falling time of the particles in the dilute phase cascaded at a certain discharge angle is influenced by the drum rotating speed as it affects the falling height in the dilute phase. Drum rotating speed obviously influences the translational velocity component V_x of the dilute phase, but just slightly affects the translational velocity components V_y and V_z. The particle size and shape in the range investigated here influence the particle motion inside the FRD, as differences exist between plastic balls and soybeans in translational velocity and rotational velocity.

The particle motion in an FRD is also investigated in detail by PTV experimental measurements and DEM simulations. The segmentation process and the probability relaxation algorithm are applied to simultaneously track the particles in the FRD with a satisfactory recovery ratio. The particle motion is systematically analyzed based on changes in correlated particle trajectories. The results show that the holdup ratio and the discharging range of the flight increase as the drum rotation speed increases. The effect of the rotating speed on the cascading rate of a single flight is more pronounced in the early and last discharging periods. Besides, the increase in drum rotating speed does not improve the falling time distribution in the dilute phase obviously. Moreover, the particle

ratios in the three investigated phases (flight phase, dilute phase and bed phase) change periodically in every quarter of the drum rotating cycle and show a strong dependence on the drum rotating speed. Larger ratios of flight and dilute phases can be observed at higher drum rotating speeds. In addition, the average velocities and granular temperatures of the FRD particle system increase as the drum rotating speed increases and the filling degree decreases. The fluctuations of particle average velocities and granular temperatures are stronger in the vertical direction than in the horizontal direction.

To study the influence of the number of flights on the particle dynamics, drums with 1, 4, 8 or 12 flights have been considered in this work. The experiment data from PTV measurements are compared with model predictions and DEM simulations. The number of flights has little effect on the holdup ratio and the cascading rate of a single flight at the drum rotating speed of 10 rpm. But as the drum rotating speed increases, the drums with 8 and 12 flights show a small increment in these two parameters at the beginning of the discharge process. Increasing the number of flights can greatly enhance the holdup ratio and the cascading rate of the active flights, and this influence is stronger than the effect from drum rotating speed. A larger and more stable particle ratio of dilute phase is obtained when the drum has more flights. Moreover, as the number of flights and the drum rotating speed increase, the ratio of falling particles seems to be limited by a maximum. DEM simulations agree well with PTV measurements.

10.2 Outlook

The PTV method adopted in this work investigates the movement and the distribution of the plastic balls with standard spherical shape in FRDs. However, the granular materials in the processing industries are normally not limited in the spherical shape and could cause more complicated behavior. For our next step work, the PTV method will be further applied to study the flow behavior of non-spherical particles in FRD.

Due to the lack of drying equipment and detection device, the scope of this research lies in the particle motion in the FRD, study on heat transfer is lacking. Some important issues in developing an efficient heat and mass transfer system should be discussed.

One concern is related to the indirectly heated drums. In this case, the heat transfer between the particles, wall and particles, as well as gas and particles should be in detail investigated. DEM simulations and corresponding experimental measurements will be set up. The different heat transfer modes will be implemented and evaluated in the DEM model.

Another concern is about the directly heated drums. Our next step study will focus on the heat and mass transfer in the dilute phase region. A CFD-DEM model with the potential of combining computations of gas flow and particle motion will be applied to investigate the heating process in FRDs.

Bibliography

[1] A. J. Matchett, C. G. J. Baker, Particle residence times in cascading rotary dryers. Part 1: Derivation of the two-stream model, Journal of Separation Process Technology 8 (4) (1987) 11–17.

[2] M. A. Karali, K. R. Sunkara, F. Herz, E. Specht, Experimental analysis of a flighted rotary drum to assess the optimum loading, Chemical Engineering Science 138 (2015) 772–779.

[3] R. G. Sherritt, R. Caple, L. A. Behie, A. K. Mehrotra, The movement of solids through flighted rotating drums. Part 1: Model formulation, The Canadian Journal of Chemical Engineering 71 (3) (1993) 337–346.

[4] J. J. Kelly, J. P. O'Donnell, Dynamics of granular material rotary dryers and coolers., Institution of Chemical Engineers, Symposium Series 29 (1968) 33–41.

[5] J. Kelly, Flight design in rotary dryers, Drying Technology 10 (4) (1992) 979–993.

[6] A. S. Mujumdar, Handbook of Industrial Drying, Revised and Expanded, CRC press, Florida, 1995.

[7] J. G. Purcell, Practical rotary cascading dryer design., Chemical Engineering 346 (1979) 496–497.

[8] K. R. Sunkara, F. Herz, E. Specht, J. Mellmann, R. Erpelding, Modeling the discharge characteristics of rectangular flights in a flighted rotary drum, Powder Technology 234 (2013) 107–116.

[9] W. Blumberg, E. U. Schlünder, Transversale Schüttgutbewegung und Konvektiver Stoffübergang in Drehrohren, Teil 2: Mit Hubschaufeln, Chemical Engineering and Processing: Process Intensification 35 (6) (1996) 405–411.

[10] M. A. Karali, E. Specht, F. Herz, J. Mellmann, H. A. Refaey, Unloading characteristics of flights in a flighted rotary drum operated at optimum loading, Powder Technology 333 (2018) 347–352.

[11] R. G. Sheritt, J. Chaouki, A. K. Mehrotra, L. A. Behie, Axial dispersion in the three-dimensional mixing of particles in a rotating drum reactor, Chemical Engineering Science 58 (2) (2003) 401–415.

[12] E. Alizadeh, O. Dubé, F. Bertrand, J. Chaouki, Characterization of mixing and size segregation in a rotating drum by a particle tracking method, AIChE Journal 59 (6) (2013) 1894–1905.

[13] E. Alizadeh, F. Bertrand, J. Chaouki, Comparison of DEM results and Lagrangian experimental data for the flow and mixing of granules in a rotating drum, AIChE Journal 60 (1) (2014) 60–75.

[14] M. R. Hawkesworth, D. J. Parker, P. Fowles, J. F. Crilly, N. L. Jefferies, G. Jonkers, Nonmedical applications of a positron camera, Nuclear Instruments and Methods in Physics Research, Section A: Accelerators, Spectrometers, Detectors and Associated Equipment 310 (1-2) (1991) 423–434.

[15] D. J. Parker, A. E. Dijkstra, T. W. Martin, J. P. K. Seville, Positron emission particle tracking studies of spherical particle motion in rotating drums, Chemical Engineering Science 52 (13) (1997) 2011–2022.

[16] Y. L. Ding, J. P. K. Seville, R. Forster, D. J. Parker, Solids motion in rolling mode rotating drums operated at low to medium rotational speeds, Chemical Engineering Science 56 (5) (2001) 1769–1780.

[17] A. J. Morrison, I. Govender, A. N. Mainza, D. J. Parker, The shape and behaviour of a granular bed in a rotating drum using Eulerian flow fields obtained from PEPT, Chemical Engineering Science 152 (2016) 186–198.

[18] G. Mohs, O. Gryczka, S. Heinrich, L. Mörl, Magnetic monitoring of a single particle in a prismatic spouted bed, Chemical Engineering Science 64 (23) (2009) 4811–4825.

[19] M. Jiang, Y. Zhao, G. Liu, J. Zheng, Enhancing mixing of particles by baffles in a rotating drum mixer, Particuology 9 (3) (2011) 270–278.

[20] W. L. Vargas, S. K. Hajra, D. Shi, J. J. McCarthy, Suppressing the segregation of granular mixtures in rotating tumblers, AIChE Journal 54 (12) (2008) 3124–3132.

[21] F. Geng, Y. Wang, Y. Li, L. Yuan, X. Wang, M. Liu, Z. Yuan, Numerical simulation on mixing dynamics of flexible filamentous particles in the transverse section of a rotary drum, Particuology 11 (5) (2013) 594–600.

[22] R. J. Adrian, Particle-imaging techniques for experimental fluid mechanics, Annual Review of Fluid Mechanics 23 (1) (1991) 261–304.

[23] P. M. Lloyd, P. K. Stansby, D. J. Ball, Unsteady surface-velocity field measurement using particle tracking velocimetry, Journal of Hydraulic Research 33 (4) (1995) 519–534.

[24] J. Westerweel, Fundamentals of digital particle image velocimetry, Measurement Science and Technology 8 (12) (1997) 1379.

[25] F. R. Schofield, P. G. Glikin, Rotary dryers and coolers for granular fertilizers, Transactions of the Institution of Chemical Engineers 40 (1962) 183–190.

[26] K. R. Sunkara, F. Herz, E. Specht, J. Mellmann, Transverse flow at the flight surface in flighted rotary drum, Powder Technology 275 (2015) 161–171.

[27] P. G. Glikin, Transport of solids through flighted rotating drums, Transactions of the Institution of Chemical Engineers 56 (1978) 120–126.

[28] C. G. J. Baker, The design of flights in cascading rotary dryers, Drying Technology 6 (4) (1988) 631–653.

[29] F. Y. Wang, I. T. Cameron, J. D. Litster, V. Rudolph, A funtadamental study on particle transport through rotary dryers for flight design and system optimisation, Drying Technology 13 (5-7) (1995) 1261–1278.

[30] D. Revol, C. L. Briens, J. M. Chabagno, The design of flights in rotary dryers, Powder Technology 121 (2-3) (2001) 230–238.

[31] M. H. Lisboa, D. S. Vitorino, W. B. Delaiba, J. R. D. Finzer, M. A. S. Barrozo, A study of particle motion in rotary dryer, Brazilian Journal of Chemical Engineering 24 (3) (2007) 365–374.

[32] D. R. Van Puyvelde, Modelling the hold up of lifters in rotary dryers, Chemical Engineering Research and Design 87 (2) (2009) 226–232.

[33] R. A. Bagnold, Experiments on a gravity-free dispersion of large solid spheres in a Newtonian fluid under shear, Proceedings of the Royal Society of London. Series A 225 (1160) (1954) 49–63.

[34] P. Claudin, J. P. Bouchaud, M. E. Cates, J. P. Wittmer, Models of stress fluctuations in granular media, Physical Review E 57 (4) (1998) 4441.

[35] A. Lee, M. E. Sheehan, Development of a geometric flight unloading model for flighted rotary dryers, Powder Technology 198 (3) (2010) 395–403.

[36] M. Debacq, S. Vitu, D. Ablitzer, J. L. Houzelot, F. Patisson, Transverse motion of cohesive powders in flighted rotary kilns: Experimental study of unloading at ambient and high temperatures, Powder Technology 245 (2013) 56–63.

[37] M. Debacq, P. Thammavong, S. Vitu, D. Ablitzer, J. L. Houzelot, F. Patisson, A hydrodynamic model for flighted rotary kilns used for the conversion of cohesive uranium powders, Chemical Engineering Science 104 (2013) 586–595.

[38] K. R. Sunkara, F. Herz, E. Specht, J. Mellmann, Influence of flight design on the particle distribution of a flighted rotating drum, Chemical Engineering Science 90 (2013) 101–109.

[39] P. V. Danckwerts, Continuous flow systems: distribution of residence times, Chemical Engineering Science 2 (1) (1953) 1–13.

[40] A. S. B. Njeng, S. Vitu, M. Clausse, J. L. Dirion, M. Debacq, Effect of lifter shape and operating parameters on the flow of materials in a pilot rotary kiln, Part 2: Experimental hold-up and mean residence time modeling, Powder Technology 269 (2015) 566–576.

[41] A. S. B. Njeng, S. Vitu, M. Clausse, J. L. Dirion, M. Debacq, Effect of lifter shape and operating parameters on the flow of materials in a pilot rotary kiln, Part 1: Experimental RTD and axial dispersion study, Powder Technology 269 (2015) 554–565.

[42] A. S. B. Njeng, S. Vitu, M. Clausse, J. L. Dirion, M. Debacq, Effect of lifter shape and operating parameters on the flow of materials in a pilot rotary kiln, Part 3: Up-scaling considerations and segregation analysis, Powder Technology 297 (2016) 415–428.

[43] I. J. Paredes, B. Yohannes, H. Emady, B. J. Glasser, W. G. Borghard, F. Muzzio, A. M. Cuitiño, J. Beeckman, S. Ilias, P. Podsiadlo, E. Jezek, J. Baumgartner, The effect of operating conditions on the residence time distribution and axial dispersion coefficient of a cohesive powder in a rotary kiln, Chemical Engineering Science 158 (2017) 50–57.

[44] H. N. Emady, M. Wittman, S. Koynov, W. G. Borghard, F. J. Muzzio, B. J. Glasser, A. M. Cuitino, A simple color concentration measurement technique for powders, Powder Technology 286 (2015) 392–400.

[45] S. J. Porter, The design of rotary dryers and coolers, Transport Institute of Chemical Engineering 41 (1963) 272–287.

[46] J. J. Kelly, The kinetic angle of repose of powders, Journal of the Society of Cosmetic Chemists 21 (1) (1970) 37–51.

[47] A. J. Matchett, M. S. Sheikh, Improved model of particle motion in cascading rotary dryers, Chemical Engineering Research and Design 68 (2) (1990) 139–148.

[48] C. A. Schneider, W. S. Rasband, K. W. Eliceiri, NIH Image to ImageJ: 25 years of Image Analysis, Nature Methods 9 (7) (2012) 671–675.

[49] M. Christensen, Evaluating Porter's assumption to determine rotary dryer design loads, B. Eng. Thesis, James Cook University (2008).

[50] O. O. Ajayi, M. E. Sheehan, Application of image analysis to determine design loading in flighted rotary dryers, Powder Technology 223 (2012) 123–130.

[51] M. A. Karali, F. Herz, E. Specht, J. Mellmann, Comparison of image analysis methods to determine the optimum loading of flighted rotary drums, Powder Technology 291 (2016) 147–153.

[52] O. O. Ajayi, M. E. Sheehan, Design loading of free flowing and cohesive solids in flighted rotary dryers, Chemical Engineering Science 73 (2012) 400–411.

[53] M. A. Karali, E. Specht, F. Herz, J. Mellmann, Different camera and light positions to facilitate image analysis processing in rotary drums studies, Powder Technology 306 (2017) 55–60.

[54] S. M. Nascimento, D. A. Santos, M. A. S. Barrozo, C. R. Duarte, Solids holdup in flighted rotating drums: An experimental and simulation study, Powder Technology 280 (2015) 18–25.

[55] M. V. C. Machado, S. M. Nascimento, C. R. Duarte, M. A. S. Barrozo, Boundary conditions effects on the particle dynamic flow in a rotary drum with a single flight, Powder Technology 311 (2017) 341–349.

[56] H. Zhong, X. Lan, J. Gao, Y. Zheng, Z. Zhang, The difference between specularity coefficient of 1 and no-slip solid phase wall boundary conditions in CFD simulation of gas–solid fluidized beds, Powder Technology 286 (2015) 740–743.

[57] F. Geng, Z. Yuan, Y. Yan, D. Luo, H. Wang, B. Li, D. Xu, Numerical simulation on mixing kinetics of slender particles in a rotary dryer, Powder Technology 193 (1) (2009) 50–58.

[58] F. Geng, H. Chai, L. Ma, G. Luo, Y. Li, Z. Yuan, Simulation of dynamic transport of flexible ribbon particles in a rotary dryer, Powder Technology 297 (2016) 115–125.

[59] Z. Zhou, J. Li, J. Zhou, S. Li, J. Feng, Enhancing mixing of cohesive particles by baffles in a rotary drum, Particuology 25 (2016) 104–110.

[60] T. Bhattacharya, S. K. Hajra, J. McCarthy, A design heuristic for optimizing segregation avoidance practices in horizontal drum mixers, Powder Technology 253 (2014) 107–115.

[61] F. Yu, G. Zhou, J. Xu, W. Ge, Enhanced axial mixing of rotating drums with alternately arranged baffles, Powder Technology 286 (2015) 276–287.

[62] R. Maione, S. K. De Richter, G. Mauviel, G. Wild, DEM investigation of granular flow and binary mixture segregation in a rotating tumbler: Influence of particle shape and internal baffles, Powder Technology 286 (2015) 732–739.

[63] Q. Xie, Z. Chen, Q. Hou, A. Yu, R. Yang, DEM investigation of heat transfer in a drum mixer with lifters, Powder Technology 314 (2017) 175–181.

[64] V. Scherer, M. Mönnigmann, M. O. Berner, F. Sudbrock, Coupled DEM–CFD simulation of drying wood chips in a rotary drum – Baffle design and model reduction, Fuel 184 (2016) 896–904.

[65] L. Zhang, F. Weigler, V. Idakiev, Z. Jiang, L. Mörl, J. Mellmann, E. Tsotsas, Experimental study of the particle motion in flighted rotating drums by means of Magnetic Particle Tracking, Powder Technology 339 (2018) 817–826.

[66] V. Idakiev, L. Mörl, How to measure the particle translation and rotation in a spouted and fluidized bed?, Journal of Chemical Technology and Metallurgy 48 (5) (2013) 445–450.

[67] K. A. Buist, A. C. Gaag, N. G. Deen, J. A. M. Kuipers, Improved magnetic particle tracking technique in dense gas fluidized beds, AIChE Journal 60 (9) (2014) 3133–3142.

[68] A. Köhler, D. Pallarès, F. Johnsson, Magnetic tracking of a fuel particle in a fluid-dynamically down-scaled fluidised bed, Fuel Processing Technology 162 (2017) 147–156.

[69] A. Köhler, A. Rasch, D. Pallarès, F. Johnsson, Experimental characterization of axial fuel mixing in fluidized beds by magnetic particle tracking, Powder Technology 316 (2017) 492–499.

[70] J. C. Maxwell, A Dynamical Theory of the Electromagnetic Field, Proceedings of the Royal Society of London (1863) 531–536.

[71] H. Richert, O. Kosch, P. Görnert, Magnetic monitoring as a diagnostic method for investigating motility in the human digestive system, Magnetism in Medicine 4 (2007) 481–498.

[72] H. Chen, X. Zhao, Y. Xiao, Y. Liu, Y. Liu, Radial mixing and segregation of granular bed bi-dispersed both in particle size and density within horizontal rotating drum, Transactions of Nonferrous Metals Society of China 26 (2) (2016) 527–535.

[73] L. Sanfratello, E. Fukushima, Experimental studies of density segregation in the 3D rotating cylinder and the absence of banding, Granular Matter 11 (2) (2009) 73–78.

[74] A. Tripathi, D. V. Khakhar, Density difference-driven segregation in a dense granular flow, Journal of Fluid Mechanics 717 (2013) 643–669.

[75] M. Yamamoto, S. Ishihara, J. Kano, Evaluation of particle density effect for mixing behavior in a rotating drum mixer by DEM simulation, Advanced Powder Technology 27 (3) (2016) 864–870.

[76] D. A. Santos, C. R. Duarte, M. A. S. Barrozo, Segregation phenomenon in a rotary drum: Experimental study and CFD simulation, Powder Technology 294 (2016) 1–10.

[77] S. H. Chou, C. C. Liao, S. S. Hsiau, The effect of interstitial fluid viscosity on particle segregation in a slurry rotating drum, Physics of Fluids 23 (8) (2011) 83301.

[78] C. C. Liao, S. S. Hsiau, H. C. Nien, Effects of density ratio, rotation speed, and fill level on density-induced granular streak segregation in a rotating drum, Powder Technology 284 (2015) 514–520.

[79] F. M. White, Fluid Mechanics, McGraw-Hill, New York, 1994.

[80] R. Clift, J. R. Grace, M. E. Weber, Bubbles, Drops, and Particles, Academic Press, North Chelmsford, 1978.

[81] L. Zhang, Z. Jiang, F. Weigler, F. Herz, J. Mellmann, E. Tsotsas, PTV measurement and DEM simulation of the particle motion in a flighted rotating drum, Powder Technology 363 (2020) 23–37.

[82] C. H. Tai, S. S. Hsiau, Dynamic behaviors of powders in a vibrating bed, Powder Technology 139 (3) (2004) 221–232.

[83] Y. C. Chung, S. S. Hsiau, H. H. Liao, J. Y. Ooi, An improved PTV technique to evaluate the velocity field of non-spherical particles, Powder Technology 202 (1-3) (2010) 151–161.

[84] C. Bendicks, D. Tarlet, C. Roloff, R. Bordás, B. Wunderlich, B. Michaelis, D. Thévenin, Improved 3-D particle tracking velocimetry with colored particles, Journal of Signal and Information Processing 2 (02) (2011) 59–71.

[85] A. I. Kartushinsky, Y. A. Rudi, S. V. Tisler, M. T. Hussainov, I. N. Shcheglov, Application of particle tracking velocimetry for studying the dispersion of particles in a turbulent gas flow, High Temperature 50 (3) (2012) 381–390.

[86] B. Gopalan, M. Shahnam, R. Panday, J. Tucker, F. Shaffer, L. Shadle, J. Mei, W. Rogers, C. Guenther, M. Syamlal, Measurements of pressure drop and particle velocity in a pseudo 2-D rectangular bed with Geldart Group D particles, Powder Technology 291 (2016) 299–310.

[87] T. Hagemeier, C. Roloff, A. Bück, E. Tsotsas, Estimation of particle dynamics in 2-D fluidized beds using particle tracking velocimetry, Particuology 22 (2015) 39–51.

[88] Z. Jiang, T. Hagemeier, A. Bück, E. Tsotsas, Experimental measurements of particle collision dynamics in a pseudo-2D gas-solid fluidized bed, Chemical Engineering Science 167 (2017) 297–316.

[89] Z. Jiang, T. Hagemeier, A. Bück, E. Tsotsas, Color-PTV measurement and CFD-DEM simulation of the dynamics of poly-disperse particle systems in a pseudo-2D fluidized bed, Chemical Engineering Science 179 (2018) 115–132.

[90] K. Meyer, A. Bück, E. Tsotsas, Determination of particle exchange rates at over-flow weirs in horizontal fluidised beds by particle tracking velocimetry, Particuology 32 (2017) 1–9.

[91] K. Vollmari, R. Jasevičius, H. Kruggel-Emden, Experimental and numerical study of fluidization and pressure drop of spherical and non-spherical particles in a model scale fluidized bed, Powder Technology 291 (2016) 506–521.

[92] H. Chou, C. Lee, Cross-sectional and axial flow characteristics of dry granular material in rotating drums, Granular Matter 11 (1) (2009) 13–32.

[93] K. Takehara, T. Etoh, A study on particle identification in PTV particle mask correlation method, Journal of Visualization 1 (3) (1998) 313–323.

[94] K. Ohmi, H. Y. Li, Particle-tracking velocimetry with new algorithms, Measurement Science and Technology 11 (6) (2000) 603–616.

[95] F. Aurenhammer, Voronoi diagrams: A survey of a fundamental geometric data structure, ACM Computing Surveys (CSUR) 23 (3) (1991) 345–405.

[96] H. Capart, D. L. Young, Y. Zech, Voronoi imaging methods for the measurement of granular flows, Experiments in Fluids 32 (1) (2002) 121–135.

[97] B. Spinewine, H. Capart, M. Larcher, Y. Zech, Three-dimensional Voronoi imaging methods for the measurement of near-wall particulate flows, Experiments in Fluids 34 (2) (2003) 227.

[98] V. A. Luchnikov, N. N. Medvedev, L. Oger, J. P. Troadec, Voronoi-Delaunay analysis of voids in systems of nonspherical particles, Physical Review E 59 (6) (1999) 7205.

[99] S. T. Barnard, W. B. Thompson, Disparity analysis of images, IEEE Transactions on Pattern Analysis and Machine Intelligence (4) (1980) 333–340.

[100] S. J. Baek, S. J. Lee, A new two-frame particle tracking algorithm using match probability, Experiments in Fluids 22 (1) (1996) 23–32.

[101] F. Pereira, H. Stüer, E. C. Graff, M. Gharib, Two-frame 3D particle tracking, Measurement Science and Technology 17 (7) (2006) 1680–1692.

[102] W. Brevis, Y. Niño, G. H. Jirka, Integrating cross-correlation and relaxation algorithms for particle tracking velocimetry, Experiments in Fluids 50 (1) (2011) 135–147.

[103] L. Zhang, Z. Jiang, J. Mellmann, F. Weigler, F. Herz, A. Bück, E. Tsotsas, Influence of the number of flights on the dilute phase ratio in flighted rotating drums by PTV measurements and DEM simulations, Particuology (2020) Online.

[104] K. Kröll, Trocknungstechnik: Trockner und Trocknungsverfahren [Drying technology: Dryers and drying procedures], Springer Verlag, Berlin-Heidelberg-New York, 1978.

[105] R. H. Perry, D. W. Green, J. O. Maloney, Perry's Chemical Engineers' Handbook, McGraw-Hill, New York, 1997.

[106] P. A. Cundall, O. D. L. Strack, A discrete numerical model for granular assemblies, Geotechnique 29 (1) (1979) 47–65.

[107] S. Yang, A. Cahyadi, J. Wang, J. W. Chew, DEM study of granular flow characteristics in the active and passive regions of a three-dimensional rotating drum, AIChE Journal 62 (11) (2016) 3874–3888.

[108] J. Ai, J.-F. Chen, J. M. Rotter, J. Y. Ooi, Assessment of rolling resistance models in discrete element simulations, Powder Technology 206 (3) (2011) 269–282.

[109] H. Chen, Y. G. Xiao, Y. L. Liu, Y. S. Shi, Effect of Young's modulus on DEM results regarding transverse mixing of particles within a rotating drum, Powder Technology 318 (2017) 507–517.

[110] J. A. Rinde, Poisson's ratio for rigid plastic foams, Journal of Applied Polymer Science 14 (8) (1970) 1913–1926.

[111] C. Goniva, C. Kloss, N. G. Deen, J. A. M. Kuipers, S. Pirker, Influence of rolling friction on single spout fluidized bed simulation, Particuology 10 (5) (2012) 582–591.

[112] Z. C. Jiang, C. Rieck, A. Bück, E. Tsotsas, Estimation of coefficient of restitution of irregularly shaped particles on horizontal substrates, in: 8th International Granulation Workshop, Sheffield, UK, 2017, pp. 28–30.

[113] D. A. Santos, M. A. S. Barrozo, C. R. Duarte, F. Weigler, J. Mellmann, Investigation of particle dynamics in a rotary drum by means of experiments and numerical simulations using DEM, Advanced Powder Technology 27 (2) (2016) 692–703.

[114] T. Kobayashi, T. Tanaka, N. Shimada, T. Kawaguchi, DEM–CFD analysis of fluidization behavior of Geldart Group A particles using a dynamic adhesion force model, Powder Technology 248 (2013) 143–152.

[115] J. J. Kelly, O. JP, Encyclopaedia of Chemical Technology, 3rd edition, John Wiley and Sons, New York, 1981.

[116] M. Jalaal, D. D. Ganji, An analytical study on motion of a sphere rolling down an inclined plane submerged in a Newtonian fluid, Powder Technology 198 (1) (2010) 82–92.

[117] R. Martino, A. Paterson, M. F. Piva, Experimental and analytical study of the motion of a sphere falling along an inclined plane in still water, Powder Technology 283 (2015) 227–233.

[118] N. Jain, J. M. Ottino, R. M. Lueptow, An experimental study of the flowing granular layer in a rotating tumbler, Physics of Fluids 14 (2) (2002) 572–582.

[119] K. R. Sunkara, Granular flow and design studies in flighted rotating drums, Ph.D. thesis, Universitätsbibliothek (2013).

[120] C. M. Dury, G. H. Ristow, J. L. Moss, M. Nakagawa, Boundary effects on the angle of repose in rotating cylinders, Physical Review E 57 (4) (1998) 4491.

[121] A. A. Boateng, P. V. Barr, Granular flow behaviour in the transverse plane of a partially filled rotating cylinder, Journal of Fluid Mechanics 330 (1997) 233–249.

[122] J. E. Maneval, K. M. Hill, B. E. Smith, A. Caprihan, E. Fukushima, Effects of end wall friction in rotating cylinder granular flow experiments, Granular Matter 7 (4) (2005) 199–202.

[123] L. E. Silbert, J. W. Landry, G. S. Grest, Granular flow down a rough inclined plane: Transition between thin and thick piles, Physics of Fluids 15 (1) (2003) 1–10.

Publication list

Journal Papers

1. **L. Zhang**, F. Weigler, V. Idakiev, Z. Jiang, L. Mörl, J. Mellmann, E. Tsotsas, *Experimental study of the particle motion in flighted rotating drums by means of Magnetic Particle Tracking,* Powder Technology 339 (2018), 817–826. 10.1016/j.powtec.2018.08.057

2. **L. Zhang**, Z. Jiang, F. Weigler, F. Herz, J. Mellmann, E. Tsotsas, *PTV measurement and DEM simulation of the particle motion in a flighted rotating drum,* Powder Technology 363 (2020), 23–37. 10.1016/j.powtec.2019.12.035

3. **L. Zhang**, Z. Jiang, J. Mellmann, F. Weigler, F. Herz, A. Bück, E. Tsotsas, *Influence of the number of flights on the dilute phase ratio in flighted rotating drums by PTV measurements and DEM simulations,* Particuology (2020). 10.1016/j.partic.2020.09.010

Conference Proceeding

1. **L. Zhang**, F. Weigler, Z. Jiang, V. Idakiev, L. Mörl, J. Mellmann, E. Tsotsas, *Investigation of 3D particle flow in a flighted rotating drum,* In: The 21th International Drying Symposium, Valencia (ES), September, 2018. 10.4995/IDS2018.2018.7389

Oral and Poster Presentations

1. **L. Zhang**, L. Mörl, J. Mellmann, E. Tsotsas, *Study of particle motion in a flighted rotating drum by means of Magnetic Particle Tracking and DEM simulation,* In: Annual Meeting of the Process Net "Agglomeration und Schüttguttechnik", Nestle Research Lausanne, Switzerland, March, 2019 (Poster)

2. **L. Zhang**, J. Mellmann, E. Tsotsas, *Dynamic behaviour of particle curtains in a flighted rotating drum investigated by PTV experiments and a DEM model,* In: PARTEC, Nürnberg (DE), April, 2019 (Oral)